Laboratory study on the optical properties of absorbing atmospheric aerosols and field applications.

DISSERTATION

zur Erlangung des Grades

Doktor der Naturwissenschaften

(Dr. rer.nat.)

Jorge Michel Flores

am Fachbereich 08 für Physik, Mathematik und Informatik
(Max-Planck-Institut für Chemie)
der Johannes Gutenberg-Universität Mainz

vorgelegt von
Jorge Michel Flores
geboren in Mexico City / Mexico
Mainz, 2011

To Male

"Vive intensamente"

J.M.Magdalena López L.

Abstract

The interaction between aerosols and sun light plays an important role in the radiative balance of Earth's atmosphere. This interaction is obtained by measuring the removal (extinction), redistribution (scattering), and transformation into heat (absorption) of light by the aerosols; i.e. their optical properties. Knowledge of these properties is crucial for our understanding of the atmospheric system.

Light absorption by aerosols is a major contributor to the direct and indirect effects on our climate system, and an accurate and sensitive measurement method is crucial to further our understanding. A homebuilt photoacoustic sensor (PAS), measuring at a 532nm wavelength, was fully characterized and its functionality validated for measurements of absorbing aerosols. The optical absorption cross-sections of absorbing polystyrene latex spheres, to be used as a standard for aerosol absorption measurements, were measured and compared to literature values. Additionally, a calibration method using absorbing aerosol of known complex refractive index was presented.

A new approach to retrieve the effective broadband refractive indices ($m_{broad,eff}$) of aerosol particles by a white light aerosol spectrometer (WELAS) optical particle counter (OPC) was achieved. Using a tandem differential mobility analyzer (DMA)-OPC system, the $n_{broad,eff}$ are obtained for both laboratory and field applications. This method was tested in the laboratory using substances with a wide range of optical properties and it was used in ambient measurements to retrieve the $n_{broad,eff}$ of biomass burning aerosols in a nationwide burning event in Israel. The retrieved effective broadband refractive indices for laboratory generated scattering aerosols were: ammonium sulfate (AS), glutaric acid (GA), and sodium chloride, all within 4% of literature values. For absorbing substances, nigrosine and various mixtures of nigrosine with AS and GA were measured, as well as a lightly absorbing substance, Suwannee river fulvic acid (SRFA). For the ambient measurements, the calibration curves generated from this method were to follow the optical evolution of biomass burning (BB) aerosols. A decrease in the overall aerosol absorption and scattering for aged aerosols during the day after the fires compared to the smoldering phase of the fires was found.

The connection between light extinction of aerosols, their chemical composition and hygroscopicity for particles with different degrees of absorption was studied. The extinction cross-section (σ_{ext}) at 532nm for different mobility diameters was measured at 80% and 90% relative humidity (RH), and at an RH<10%. The ratio of the humidified aerosols to the dry ones, fRH_{ext}(%RH,Dry), is presented. For purely scattering aerosols, fRH_{ext}(%RH,Dry) is inversely proportional with size; this dependence was suppressed for lightly absorbing ones. In addition, the validity of the mixing rules for water soluble absorbing aerosols is explored. The difference between the derived and calculated real parts of the complex RIs were less than 5.3% for all substances, wavelengths, and RHs. The obtained imaginary parts for the retrieved and calculated RIs were in good agreement with each other, and well within the measurement errors of retrieval from pulsed CRD spectroscopy measurements. Finally, a

core-shell structure model is also used to explore the differences between the models, for substances with low growth factors, under these hydration conditions. It was found that at 80% RH and for size parameters less than 2.5, there is less than a 5 % difference between the extinction efficiencies calculated with both models. This difference is within measurement errors; hence, there is no significant difference between the models in this case. However, for greater size parameters the difference can be up to 10%. For 90% RH the differences below a size parameter of 2.5 were up to 7%.

Finally, the fully characterized PAS together with a cavity ring down spectrometer (CRD), were used to study the optical properties of soot and secondary organic aerosol (SOA) during the SOOT-11 project in the AIDA chamber in Karlsruhe, Germany. The fresh fractal-like soot particles were allowed to coagulate for 28 hours before stepwise coating them with SOA. The single scattering albedo for fresh fractal-like soot was measured to be 0.2 (±0.03), and after allowing the soot to coagulate for 28 hours and coating it with SOA, it increased to 0.71(±0.01). An absorption enhancement of the coated soot of up to 1.71 (±0.03) times from the non-coated coagulated soot was directly measured with the PAS. Monodisperse measurements of SOA and soot coated with SOA were performed to derive the complex refractive index (m) of both aerosols. A complex refractive index of m = 1.471(±0.008) + i0.0(±0.002) for the SOA-αO_3 was retrieved. For the compact coagulated soot a preliminary complex refractive index of m = 2.04(+0.21/-0.14) + i0.34(+0.18/-0.06) with 10nm(+4/-6) coating thickness was retrieved.

These detail properties can be use by modelers to decrease uncertainties in assessing climatic impacts of the different species and to improve weather forecasting.

Table of Contents

List of Figures

List of Tables

1 Introduction

1.1 Motivation

Atmospheric aerosols are solid or liquid particles suspended in the air. Aerosols that are emitted directly into the atmosphere, either by natural processes (i.e., volcano eruptions, bubble bursting of oceanic waves, sand storms, natural forest fires, etc.), or by anthropogenic emissions (i.e., biomass burning, car emission, coal power plants emission, airplane exhausts, etc.) are referred to as primary aerosols. Aerosols that are directly formed in the atmosphere by condensation of existing gases are referred to as secondary. These aerosol particles vary from nanometers to micrometers in diameter, and within the same size class, they can exhibit widely different compositions and morphologies.[1] Aerosols can influence the climate system by scattering and absorbing shortwave (solar) radiation, enhancing cloud lifetime,[2] increasing cloud reflectance,[3] suppressing precipitation,[4] or by evaporating clouds.[5] Changes in the aerosols atmospheric concentrations and/or their chemical, and physical properties alter the energy balance of the climate system and are drivers of climate change.[6] The resulting positive or negative changes in energy balance due to these factors are expressed as radiative forcing, which is used to compare warming or cooling influences on global climate.[6] The last report from the Intergovernmental Panel on Climate Change (IPCC) showed that, to a great extent, aerosols have a cooling effect. However, our level of scientific understanding of the radiative forcing effect of aerosols in the atmosphere is still low. Specially, the role of light absorbing aerosols is poorly understood, as they transform electromagnetic radiation into thermal energy thereby changing the temperature profiles of their surroundings and reducing the incident solar power below the absorbing aerosols.[7, 8] The heating caused by the aerosols can cause a positive top-of-atmosphere radiative forcing[9] if they decrease the planetary albedo (as seen from space) or if the their single scattering albedo (SSA) is lower than the surface, or cloud, below them.[10] Moreover, if light absorbing aerosols are deposited on snow or ice, they can reduce the albedo of these surfaces,[11, 12] but the extent of this reduction is still under investigation.[13] Although the absorption of light by aerosols causes positive radiative forcing, in most cases it is just counteracting cooling caused by particles such as sulfates that predominantly scatter light.[14, 15] Recently, there is more evidence that carbonaceous aerosols are much more dominant and widespread in the atmosphere than previously thought.[16-20] Approximately 8.0 Tg y^{-1} of black carbon (BC) and 33.9 Tg y^{-1} of organic carbon are emitted globally[21] (for the year 1996), measuring and deriving their optical properties is critical in calculating the effects of aerosols on radiative transfer.

To attempt to calculate the climatic effects of different species found in the atmosphere, researches have use chemical transport models for many years. Two implicit assumptions are used in transport models to calculate the climatic effects of any species:[22]

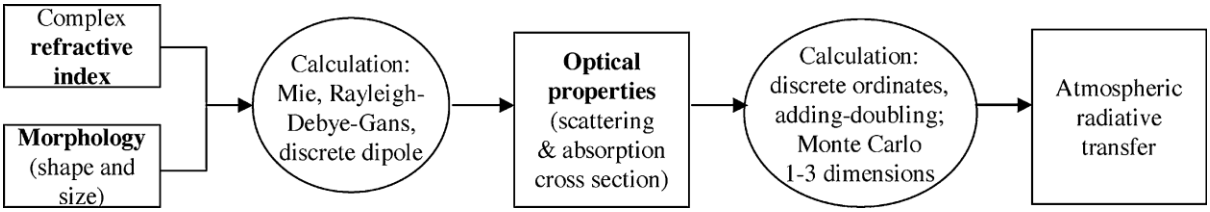

Figure 1.1 Schematic of the calculation of radiative transfer. Taken from Bond and Bergstrom (2006)[22]

1. There is a predictable relationship between emission (generation of new particles) and spatially distributed atmospheric concentration. This relationship is governed by advection, chemical transformation, and removal.

2. There is a predictable relationship between atmospheric concentration and its effects on radiative transfer. This relationship involves the optical properties of the species.

On one hand, radiative transfer models require knowledge of emissions, and on the other hand, accurate simulations of both relationships stated above, which is all embedded in a climate model in an effort to characterize the atmosphere-Earth system.[22]

A schematic of how the change in radiative transfer is determined from atmospheric concentration of light absorbing particles is shown in Figure 1.1 By first assuming a complex refractive index and physical properties of the aerosols (size, shape and state of mixing, categorized as *morphology*), most climate modelers obtain scattering and absorption cross sections, and apply those properties to modeled concentrations.[22] If the underlying assumptions are incorrect, this in turn will give a wrong estimate of the radiative forcing. Therefore, to include carbonaceous aerosols into the radiative transfer component of climate models several challenges need to be addressed:[10] (1) as mentioned above, aerosol light absorption can add a heating term to the cooling term of non-absorbing aerosols, (2) carbonaceous aerosols can be non-spherical and inhomogeneous with combustion soot often being emitted as fractal-like chain aggregates making calculation of their optical properties more difficult,[23-25] (3) aerosol light absorption from carbonaceous aerosols can be due to BC (constant imaginary part of the refractive index[22]) and due to brown carbon (BrC; wavelength dependent imaginary part of the refractive index),[26, 27] (4) some organic aerosols are formed in the atmosphere as secondary organic aerosols (SOAs),[28-30] (5) atmospheric life times and deposition modes can be strongly influenced by common atmospheric transition from hydrophobic to hydrophilic[31-33] and by morphology changes such as fractal collapse,[34, 35] and (6) carbonaceous aerosols are emitted from both natural and anthropogenic sources.[20] All these challenges have to a certain extent been addressed, but despite the vast literature and experience, the optical properties of atmospheric absorbing aerosol are not well understood, leaving a gap in our understanding of the optical properties of aerosols, and consequently, leading to major uncertainties in assessing their current and future climatic impacts; it is therefore necessary to perform detailed laboratory experiments on the absorbing properties of aerosols.

Laboratory measurements can be performed to simulate atmospheric processes in a control environment; such as chemical reactions or physical changes that can occur to aerosols in the atmosphere. They can also be used to measure, with a low level of uncertainty, the physical, chemical, and optical properties of single substances present in the atmosphere. These detail properties can later be use by modelers to decrease uncertainties in assessing climatic impacts of the different species. Laboratory studies can also be used to verify the calibrations of the different instrumentation being used in field project or to develop and characterize instruments.

1.2 Overview of dissertation

In this dissertation, four different laboratory studies related to the optical properties of absorbing aerosols will be presented. First, some theoretical background of light interaction with aerosols followed by a full characterization of a photoacoustic spectrometer, to directly measure the absorption by aerosols, will be given. Second, a new method to retrieve the complex refractive indices of aerosols with different degrees of absorption, using a white light spectrometer, will be presented. Next, an investigation of the interaction of water soluble absorbing substances with high relative humidity environments at two discrete wavelengths will be given. Finally, the optical properties of fresh fractal-like soot, and the internal mixture of coagulated soot with secondary organic aerosol will be presented. Every experiment will be covered in individual chapters and a comprehensive introduction will be given at the beginning of each chapter, only a brief overview of each study will be given in the remainder of this section.

In Chapter 2, a review of the definitions and some theoretical background of aerosol light extinction, scattering, and absorption will be given first. This is followed by a description and theoretical framework of the three optical instruments used in the other studies presented here: a White light aerosol spectrometer (Chapter 3), a cavity ring down spectrometer (Chapters 4 and 5), and a photoacoustic spectrometer (Chapters 4 and 5). Following, the full characterization of the photoacoustic spectrometer obtained from the research group of Martin Schnaiter in the Karlsruhe Institute of Technology will be given. Finally, a calibration method for the photoacoustic spectrometer using absorbing aerosols instead of gases is explored.

In Chapter 3, the first attempt to use a white light spectrometer to retrieve effective broadband refractive indices ($m_{broad,eff}$) for a variety of scattering and absorbing aerosol particles is described. The developed retrieval method can also be easily applied as a calibration approach to improve the performance of optical particle counters, both in the laboratory and in field settings. Furthermore, by using a white light source, the actinic light which the atmospheric aerosol interacts with, was mimicked. Therefore, crucial information concerning aerosols radiative properties can be obtained by using this method. For attaining information concerning aerosols' radiative properties a wide range of substances with

different optical properties, including pure scatterers, lightly and highly absorbing particles, were examined. Finally, the developed method was adapted for field applications, where the characterization of the $m_{broad,eff}$ evolution of submicron aerosols from a large anthropogenic biomass burning (BB) event in Israel, is presented.

In Chapter 4, the validity of the mixing rules for water soluble absorbing aerosols is explored. Furthermore, a closure study between measured hygroscopic growth factors, measured optical extinction, and model calculations in order to study the ability of the model to predict the optical properties of hydrated aerosols with different degrees of absorption, is performed. Moreover, it is investigated how the ratio of the extinction coefficient of the humidified aerosols to the dry extinction coefficient changes as a function of size. Finally, a core-shell structure model is also used to explore the differences between the models, for substances with low growth factors, under these hydration conditions. These laboratory measurements will be used as a basis to investigate how hydrated areas of the atmosphere, such as the twilight zone[36] of warm clouds, would change if aerosols with different degrees of absorption, from purely scattering to highly absorbing, are present.

In Chapter 5, results of two simulation experiments conducted at the large aerosol chamber facility AIDA of the Karlsruhe Institute of Technology, Karlsruhe, Germany, are presented. Soot aerosol particles from a Combustion Aerosol Standard were coated with secondary organic aerosols (SOA) generated by the ozonolysis of α-pinene. The non absorbing SOA particles with strongly absorbing soot inclusions was investigated as the geometry resembles the internally mixed soot particles in the atmosphere, and are good proxies for soot/sulfate mixtures which may be more frequent in the atmosphere. The optical properties of the particles were monitored using the cavity ring down spectrometer and the photoacoustic spectrometer at 532nm. Using a Mie model for homogenous[37] and coated spheres[38] the refractive indices of the SOA and the internally mixed soot particles with SOA were derived, respectively. This study also aims to further investigate the magnitude of the absorption enhancement of soot when coated with a purely scattering substance.

2 Optical properties and instrumentation

2.1 Introduction

The interaction between aerosols and sun light plays an important role in the radiative balance of Earth's atmosphere [6, 15, 39]. This interaction is obtained by measuring the removal (extinction), redistribution (scattering), and transformation into heat (absorption) of light by the aerosols; i.e. their optical properties. These properties affect the atmospheric radiative balance through a) the direct scattering and absorption of the incoming solar radiation which results in less radiation reaching the Earth's surface, referred to as the radiative ("Direct") effect, and b) the heating by absorbing aerosols can change the local atmospheric temperature, which influences relative humidity, atmospheric circulation and stability and thereby cloud formation and lifetime (semi-direct effect)*[5, 40]. The amount of scattering and absorption is determined by the size, chemical and physical properties of the particles, the ambient relative humidity, and the wavelength of the incident light.[6] The developed theories of scattering and absorption of light by particles have given us a better understanding of the aerosol radiative transfer in the Earth's atmosphere, and have served as a basis for the development of many different instruments for measuring the optical size distribution of particles, and the amount of scattering, absorption and extinction. In this chapter, a review of the definitions and some theoretical background of aerosol light extinction, scattering, and absorption will be given first. This is followed by a description and theoretical framework of the three optical instruments used in the studies presented here: the White Light Aerosol Spectrometer (WELAS), the cavity ring down spectrometer (CRD), and the photoacoustic sensor (PAS). Following, a description of the PAS calibration method and validation measurements will be given. Finally, the calibration of the PAS using absorbing aerosols is explored.

2.2 Optical properties

An illustration of the possible interactions between an incident electromagnetic wave of wavelength λ_o with a particle is shown in Figure 2.1. Even though Raman scattering and fluorescence occur in atmospheric aerosols, only elastic scattering will be addressed in this thesis, and it will be referred to as 'scattering'. Elastic scattering encompasses the combined effect of reflection, refraction, and diffraction. In elastic scattering the scattered photons have the same energy (frequency) and wavelength as the incident photons. If absorption of the incident light occurs, the absorbed energy can be re-emitted as thermal energy or fluorescence.

The combined effects of absorption and elastic scattering cause a net loss of energy from an incident light beam of irradiance I_o (in units of W/m^2), and it is referred to as

* Aerosols also serve as cloud condensation nuclei, and can control cloud lifetime, reflectivity, and breadth (microphysical "indirect" effect).

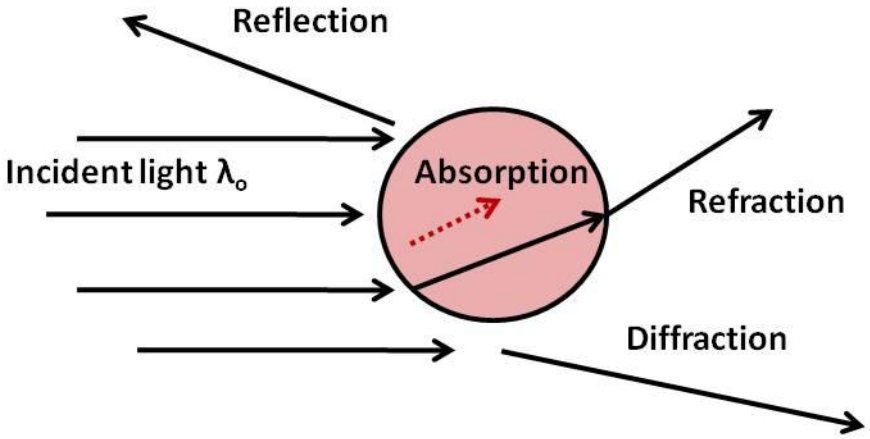

Figure 2.1 Representation of the possible optical interactions between an incident electromagnetic wave of wavelength λ_o and a particle. Raman scattering and fluorescence are not depicted.

extinction. In short, aerosol optical extinction is the sum of the effects of absorption and scattering. The total energy removed (expressed in W/m^2) from an incident beam by a single particle can be expressed as:

$$I_{ext} = I_o \cdot \sigma_{ext} \tag{2.1}$$

where σ_{ext} is the optical extinction cross-section (normally expressed in m^2) and is defined as:

$$\sigma_{ext} = \sigma_{abs} + \sigma_{sca} \tag{2.2}$$

where σ_{abs} and σ_{sca} represent the optical absorption and scattering cross-sections, respectively. The optical cross-sections are defined as:

$$\sigma_{ext/abs/sca} = Q_{ext/abs/sca} \cdot \sigma_{geometric} \quad \text{(for spherical particles } \sigma_{geometric} = \pi r^2\text{)} \tag{2.3}$$

where $\sigma_{geometric}$ is the geometric cross-section, r is the particle radius, and the Q terms are the extinction, absorption, or scattering efficiencies.[†] Q is a measure of the dimensional relationship of the optical cross section with the geometrical cross section.

For a collection of *p* particles the extinction (α_{ext}), absorption (α_{abs}), and scattering (α_{sca}) coefficients (normally given in units of Mm^{-1} = 1/10^6 m), describe the amount of light removed, absorbed, and scattered, respectively. The optical coefficients are expressed as the sums of the individual optical cross-sections of each substance present in a population of particles divided by the total volume (V) filled by this population. For the same type of particles the expression simplifies to the product of the cross-sections by the particle number concentration N [10]:

[†] The term 'efficiency' is misleading as it implies that Q cannot be greater than 1, but Q can have values much less that 1 and go up to values sometimes greater than 4. Personally, 'scaling factor' will be a better name for the term.

$$\alpha_{ext/abs/sca} = \frac{\sum_{i=1}^{n} \sigma_{ext_i/abs_i/sca_i}}{V} = N\sigma_{ext/abs/sca} \qquad where\ N = \frac{p}{V} \tag{2.4}$$

The single scattering albedo (SSA) ω for a single particle is defined as the ratio of the scattering cross-section by the extinction cross-section or their corresponding Q terms:

$$\omega = \frac{\sigma_{sca}}{\sigma_{ext}} = \frac{Q_{sca}}{Q_{ext}} \tag{2.5}$$

For an ensemble of particles the SSA is defined as the ratio of the scattering coefficient and the extinction coefficient, which, in the same way as the cross-sections, is the sum of the scattering coefficient and the absorption coefficient:

$$\omega = \frac{\alpha_{sca}}{\alpha_{ext}} = \frac{\alpha_{sca}}{\alpha_{sca} + \alpha_{abs}} \tag{2.6}$$

Hence, the SSA values range between $0 \leq \omega \leq 1$. A value of 1 represents a purely scattering particle (or population), and 0 a purely absorbing one (purely absorbing substances – *blackbodies* – do not exist in nature, it is an idealization).

All of the optical properties stated above (σ, Q, α, and ω) depend on the wavelength of the incident light, the size of the particle, and the spatial complex refractive index distribution of the surrounding medium in conjunction with the complex refractive index of the particle. In practically all atmospheric applications the complex refractive index of the surrounding medium can be taken as 1. The refractive index (*m*; RI) of a material is defined as the ratio of the speed of light in the surrounding medium (c) to the speed of light in the material (v)[‡]:

$$m = \frac{c}{v} \tag{2.7}$$

since m of the surrounding material can be taken as 1, the speed of light can be taken as that in vacuum. When the material has absorbing properties the refractive index is expressed as a complex number: $m = n + ik$, where *n* is the real and *k* the imaginary part of the refractive index. The real and imaginary parts express the extent of scattering and absorption, respectively. For most atmospheric particles *n* ranges from 1.3 to 2 and *k* from 0 to 1, depending on the wavelength. The complex refractive index is the only intrinsic optical property of a particle (where size is the intrinsic physical property); therefore, knowing the value of m is of high importance to accurately model the optical properties of aerosols.

[‡] The speed of propagation depends on the dielectric constant (ε) and magnetic constant (μ) of the material and free space: $v = 1/\sqrt{\varepsilon_o \mu_o \varepsilon \mu}$

Since the interaction of a beam of light of a particular wavelength with particle of a certain size is scale invariant (i.e., micrometer waves interact with micrometer particles in the same way as nanometer waves with nanometer particles), particles sizes are presented as the particle size parameter (x). For spherical particles, the particle size parameter is given as the ratio of the particle's circumference to the wavelength (λ) of the incident light:

$$x = \frac{2\pi r}{\lambda} \tag{2.8}$$

To calculate the various optical properties different theories have been developed depending on the size parameter (x), and the shape of the particle. When particles are "very small" compared to the wavelength ($x \ll 1$), it is customary to say that the particles are in the Rayleigh regime, and Rayleigh's theory properly models the optical properties. When particles have approximately the same size as the incident wavelength (x~1), particles are said to be in the Mie regime, and Mie Theory[§] is used. And if the particles have a much larger diameter than the wavelength ($x \gg 1$), the particles are said to be in the geometrical optics regime and classical laws of reflection, refraction, and diffraction can be used for the description of the optical properties.

Mie theory can be used to calculate the exact angular redistribution (i.e. the phase function) and absorption of light for any spherical particle at any wavelength if x and m are known, as it is a complete analytical solution of Maxwell's equations for the interaction of infinite electromagnetic plane waves with homogeneous, linear, isotropic, spherical particles.[37, 41] A detailed mathematical description of Mie theory is provided by Bohren and Hoffman (1983).

Even though Mie theory provides solutions for homogeneous spherical particles, it is regularly used for all atmospheric aerosols, regardless of their shape. Thanks to the computational power achieved in modern computers, it is very convenient to use, and since many atmospheric aerosols have, or are close to having, spherical shapes, they yield reasonable approximations. Furthermore, Mie theory has been extended to coated (core-shell) particles, spheroids, and some approximations of sphere aggregates to name a few.

[§] Mie theory is the popular name used today; however, Gustav Mie was not the only scientist involved in the development of the theory. Ludwig Lorenz also independently developed the theory of electromagnetic plane wave scattering by a dielectric sphere, and Peter Debye also contributed with his work to the understanding of light scattering. Please see the book by Milton Kerker, "The scattering of light and other electromagnetic radiation.", New York,NY. Academic Press, 1969, for a history of the development of Mie Theory.

2.3 White light aerosol optical particle counter 2100 (WELAS)

2.3.1 Working principle of optical particle counters

Optical particle counters (OPCs) are widely used in atmospheric science to determine the optical size distribution of aerosols. [42-57] OPCs use the fact that most particles, when they interact with a beam of light, scatter a portion of the total amount that was incident upon them. However, the amount of scattered light is dependent on the diameter, the complex refractive index, and the shape of the particle. To determine size distributions, OPCs assume *a priori* aerosols are spherical and have a fixed value of refractive index, and then they correlate the amount of scattered light (i.e. the value of the scattering cross section) to the particle's diameter by means of a calibration curve. The calibration curve is either theoretically determined using Mie theory, or experimentally, by measuring a photomultiplier's response to a particle of known size, refractive index, and shape. The value commonly adopted for the refractive index for calibration is that of polystyrene latex spheres (PSL, $m = 1.59 + i0$). As a result, when the refractive index of the ambient aerosol is different from that of PSL, the derived size distributions may be incorrect. This caveat can be used as an advantage to determine the refractive index of the particles measured (see chapter 3).

2.3.2 Description of the WELAS instrument

The WELAS 2100 (WELAS; PALAS Gmbh, Karlsruhe) is a white light (with an Osram Xenarc 4200 K lamp as a source) optical particle counter (OPC) with a light spectrum spanning from 370 to 780 nm (Figure 2.2). The instrument collects the light scattered between 79 to 101° (90° mean scattering angle) through a 3D, patented T-shape, optically defined measuring volume (Figure 2.3).[56] It samples at 5 L min^{-1}, and only counts particles that go through the optically defined measuring volume (155 x 155 x 177 mm). The scattered light intensity for every particle measured is classified into one of 4095 channels according to the intensity of the light scattered. By comparison to a calibration curve, a corresponding size is assigned for every channel. Figure 2.4 shows an example of typical size distributions measured by the WELAS for two different types of aerosols. The WELAS can be calibrated with a calibration dust (CalDust 1100, supplied by PALAS) which has the same index of refraction as PSL. This calibration was verified in this work with PSL spheres using the particle generation system described in Appendix I.

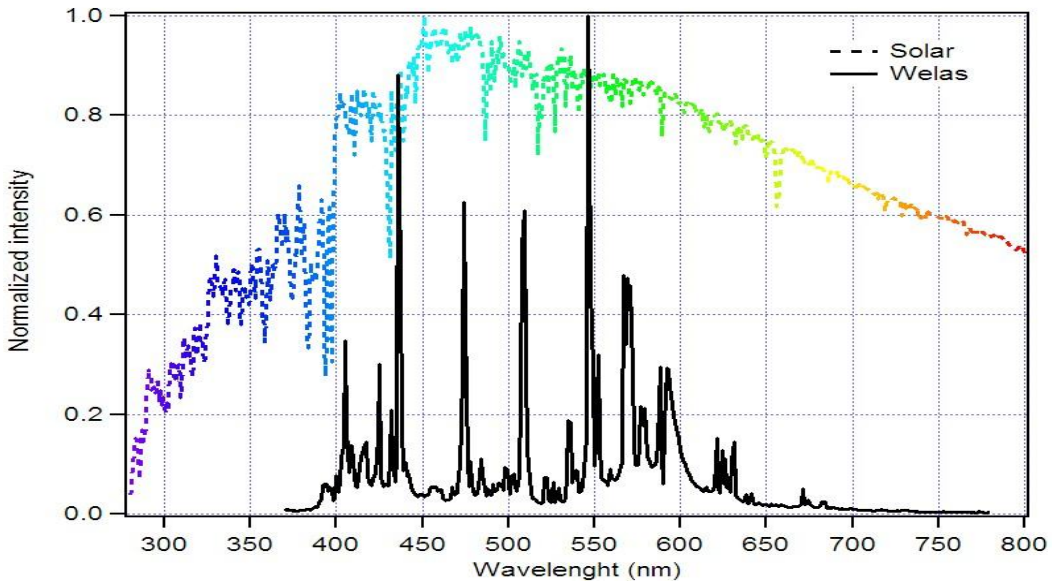

Figure 2.2 WELAS white light source spectrum (solid line; provided by PALAS Gmbh). The solar spectrum (color-dotted line) at Earth's surface is shown for comparison.

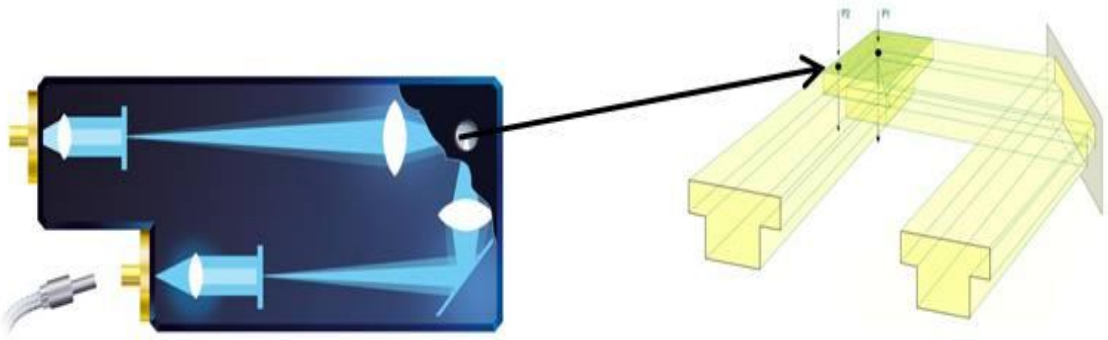

Figure 2.3 WELAS cross section and 3D measuring volume.

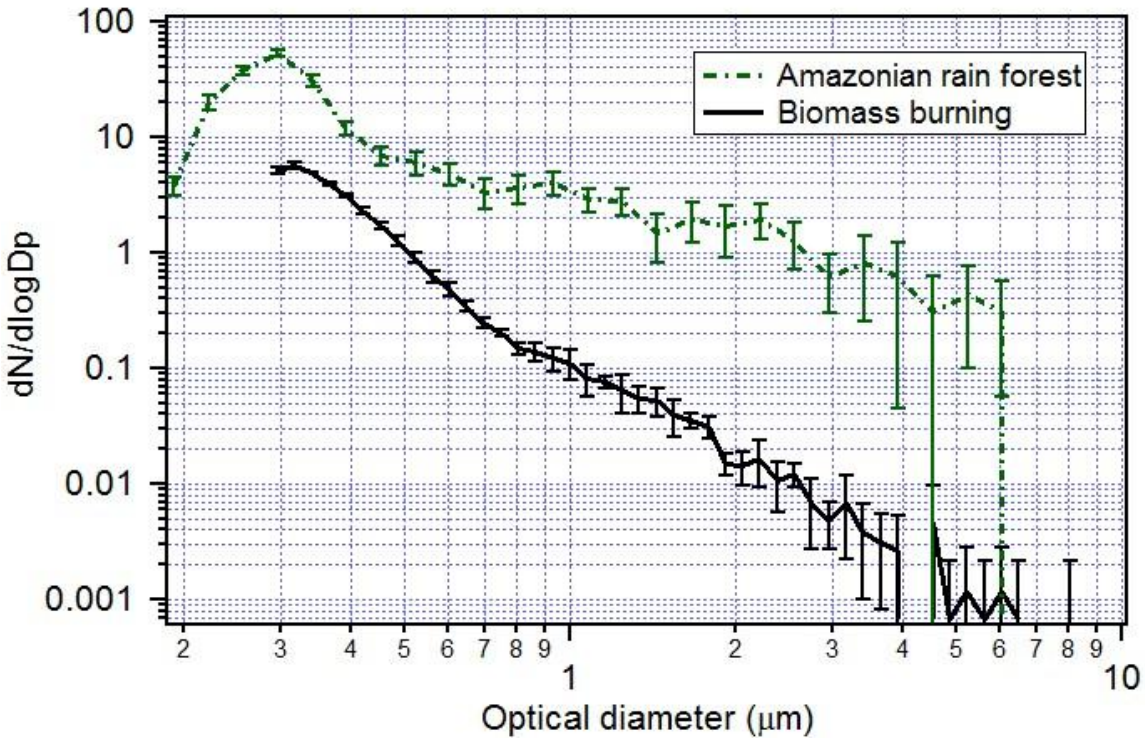

Figure 2.4. Typical size distributions measured by the WELAS for two different types of aerosols: pristine aerosol from the Amazonian rain forest in February 2008 (green dot-line curve), and biomass burning aerosols from a wood burning event in Israel in May 2010 (black line). The error bars show the variation over 2 days, and 5 hours for the Amazonian and wood burning measurement, respectively.

2.4 Cavity ring-down aerosol spectroscopy

2.4.1 Theory

Cavity ring down spectroscopy (CRDS) is a technique developed by O'Keefe and Deacon (1988)[58] to directly measure the absorption coefficient of absorbing gases, and it was later extended to measure the extinction coefficient of aerosols by Sappy *et al.*(1998).[59] With the development of laser technology, it rapidly became a widely used technique in atmospheric science. [60-73] Reviews on all the different applications can be found in works of Scherer *et al.* (1997)[74], Wheeler *et al.* (1998)[75], Busch and Busch (1999)[76], Berden *et al.* (2000)[77], and Brown (2003)[78].

The basic principle of CRDS is to inject a short laser pulse into an optical cavity composed of two highly reflecting mirrors placed opposite of each other which are separated by a distance no longer than a meter. This pulse is reflected back and forth and every time the pulse reaches the back end mirror, a small amount of light is transmitted, and a photomultiplier (PMT) placed at this end measures the intensity of the transmitted light. By measuring the time it takes the intensity of the laser pulse to decay 1/e of the initial intensity a time constant is obtained (see Figure 2.5).

The decay in intensity (I) is a result of the losses inside the cavity and the mirrors, follows Beer-Lambert's law; and thus can be expressed as:

$$I(t) = I_o \cdot e^{\left(\frac{-\tau}{\tau_o}\right)} \tag{2.9}$$

where I_o is the initial laser pulse intensity, τ is the measured decay time, and τ_o is the characteristic decay time of the cavity. When the optical cavity is empty, the decay time (τ_o) is dominated by the mirror losses, and the cavity's length:

$$\tau_o = \frac{L}{c}(1 - R) \tag{2.10}$$

where L is the length of the cavity (the distance between the two mirrors), c is the speed of light, and R is the reflectivity of the mirrors. When the cavity is filled with aerosols, and /or gaseous substances (in the case of laboratory measurements N_2 gas), the decay time is given by[59]:

$$\tau = L/c(lnR + \sigma_{aerosols}NL_{aerosols} + \sigma_{Rayleigh}NL_{scattering\ molecules} + \sigma_{abs}NL_{absorbers} + \cdots) \tag{2.11}$$

where σ is the optical extinction cross-section, and N is the number concentration of the scattering and absorbing aerosols or molecules. When measurements take place in the laboratory, normally, pure nitrogen is used as a carrier gas for the aerosols, and no absorbing gas is introduced into the cavity making σ_{abs} zero. Furthermore, the time constant for the empty cavity is measured with N_2 inside the cavity so $\sigma_{Rayleigh}$ is comprehended by τ_o and making it zero in equation 2.11. Hence τ for a cavity filled with aerosols can be expressed as:

$$\tau = \frac{L}{c}(lnR + \sigma_{aerosols}NL_{aerosols}) \tag{2.12}$$

Now $ln(R)$ can be expressed as $1 - R$[**], and since $\sigma_{ext}N$ is equal to the extinction coefficient (α_{ext}) and $\sigma_{aerosols} = \sigma_{ext}$ the extinction coefficient can be measured directly from the difference between the time constant of the empty and the filled cavity:

$$\alpha_{ext} = \frac{L_{cav}}{c}\left[\frac{1}{\tau} - \frac{1}{\tau_o}\right] \tag{2.13}$$

[**] The Taylor series for the $\ln(x)$ is:

$$\ln(x) = \sum_{n=1}^{\infty} \frac{(-1)^{n+1}}{n}(x-1)^n = (x-1) - \frac{(x-1)^2}{2} + \frac{(x-1)^3}{3} - \frac{(x-1)^4}{4}\cdots$$

For $|x - 1| \leq 1$and excluding x=0. Since the reflectivity of the mirror is >0.999 all of the high order terms can be taken as zero.

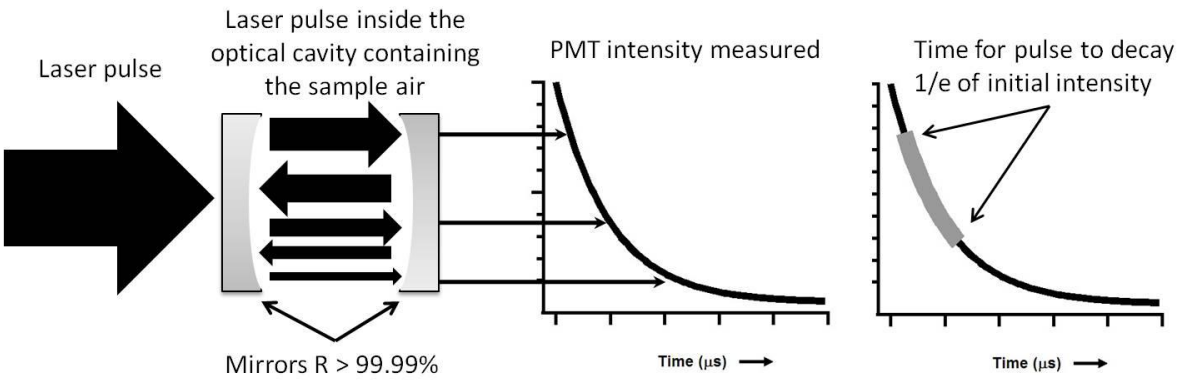

Figure 2.5 Schematic of the basic principle of cavity ring down spectroscopy. A laser pulse is injected into an optical cavity composed of two highly reflective mirrors placed opposite of each other. The laser pulse is reflected back and forth (in the picture the arrows are displaced to make the concept clearer) and light is transmitted through the back end mirror. A photomultiplier placed at this end measures the intensity of the laser pulse, and by measuring the time it takes the pulse to decay 1/e of the initial intensity a time constant is obtained.

where L_{cav} is the ratio of the total cavity length (the distance between the mirrors) and the actual distance in the cavity filled with aerosols. This also tells us that the measurement of α_{ext} is independent of the laser intensity. If the cavity is filled with homogeneous spherical particles the extinction coefficient can be described as (see equation 2.11 and 2.12):

$$\alpha_{ext} = N\sigma_{ext} = NQ_{ext}\sigma_{geometric} = NQ_{ext}\frac{1}{4}\pi D^2 \tag{2.14}$$

where Q_{ext} is the extinction efficiency, and D is the particle's diameter. Hence, by introducing a monodisperse aerosol distribution and measuring the particles' number density (e.g. with a condensation particle counter), the extinction efficiency can be measured. And by measuring Q_{ext} for different sizes (e.g. using a differential mobility analyzer (DMA) to select particle sizes) the complex refractive index of a substance in the aerosol phase can be retrieved for the wavelength of the laser pulse being injected into the cavity.

2.4.2 Detection limit and error treatment.

The minimum detectable extinction coefficient for an empty cavity can be calculated by[70, 79]:

$$\alpha_{min} = \frac{L_{cav}}{c}\frac{\Delta\tau_{min}}{\tau_o^2} = \frac{L_{cav}}{c}\frac{\sqrt{2}s(\tau_o)}{\tau_o^2\sqrt{\mathcal{R}T}} \tag{2.15}$$

where $\Delta\tau_{min}$ is the standard deviation of the decay time, $\mathcal{R}$ is the repetition rate of the pulse shots from the laser, T is the sampling rate, and $s(\tau_o)$ is the minimum detectable change in the ring down time for one laser shot. When aerosols are introduced into the cavity, the fluctuations of the aerosol concentration can lead to fluctuations in the decay time, therefore, lowering the sensitivity. Also, the uncertainty in L_{cav} can generate errors, however, these are

usually very small (< 0.5%). The error from the fluctuations in the concentration can be calculated from Poisson statistics, giving a relative error of[70]:

$$\frac{\Delta\alpha_{\mathrm{stat}}}{\alpha} = \frac{\sqrt{NV}}{NV}\frac{1}{\sqrt{\mathcal{R}T}} = \frac{1}{\sqrt{NV\mathcal{R}T}} \tag{2.16}$$

where V is the effective laser beam volume. Combining equation 2.15 and 2.16

$$\Delta\alpha = \sqrt{\frac{\alpha^2}{NV\mathcal{R}T} + \alpha_{min}^2} \tag{2.17}$$

In the experiments presented here, τ_o was ~40μs and τ_{min} was around 0.02μs for an average of a 100 laser shots operating at 15 Hz. This results in a minimum detectable extinction coefficient of ~4.96×10^{-10} cm^{-1} for an empty cavity. When the cavity is filled with aerosols the error is around the same order of magnitude [70, 71].

2.4.3 Description of the cavity ring down instrument used in this study

The cavity ring down (CRD) used in this study is depicted in Figure 2.6. It was fully developed and characterized by Riziq *et al*. (2007)[71], and only a concise description will be given here. It consists of two highly reflective concave mirrors (curvature radii of 1m and a reflectivity of 99.995% at 532 nm, Los Gatos, USA). The mirrors are mounted at the two sides of a 90 cm 3/3" stainless steel tube. A small purge flow of dry particle-free nitrogen (0.05 SLM) is introduced in front of each mirror to prevent mirror contamination by deposition of aerosols. The aerosol flow enters the CRD cell through four tubes at 45° and exits the cavity in a similar setup. This is to ensure good mixing and even concentration of the particles inside the cavity. The length of the cavity occupied by particles as they flow through the cavity is about 77 cm. The cavity can be fed with a total flow of 1 to 3 SLM. The second harmonic (532nm) of a pulsed Nd:YAG laser (Quanta-Ray GCR-100, 15 Hz, 7 ns) is introduced to the CRD through a spatial filter consisting of a red-transparent mirror to remove the excess 1064 nm pulses exiting with the second harmonic. The beam diameter in front of the cavity is about 1 mm, with energy of about 50 μJ. The intensity of the beam emerging from the CRD cell is measured with a photomultiplier (Hamamatsu H6780-02), and it is fed into a National Instruments card, which is triggered simultaneously with the laser pulse. The digitized data is transferred and stored in a personal computer using a LabVIEW program. Figure 2.7 gives an example of the output given from the CRD.

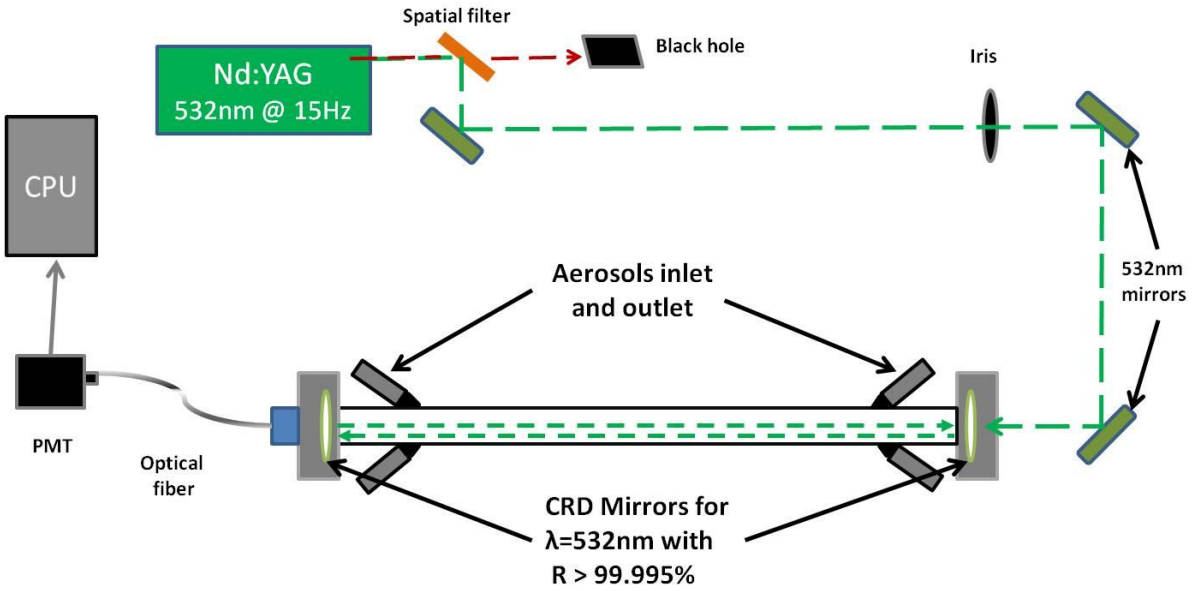

Figure 2.6 Schematic representation of the cavity ring down used in this study.

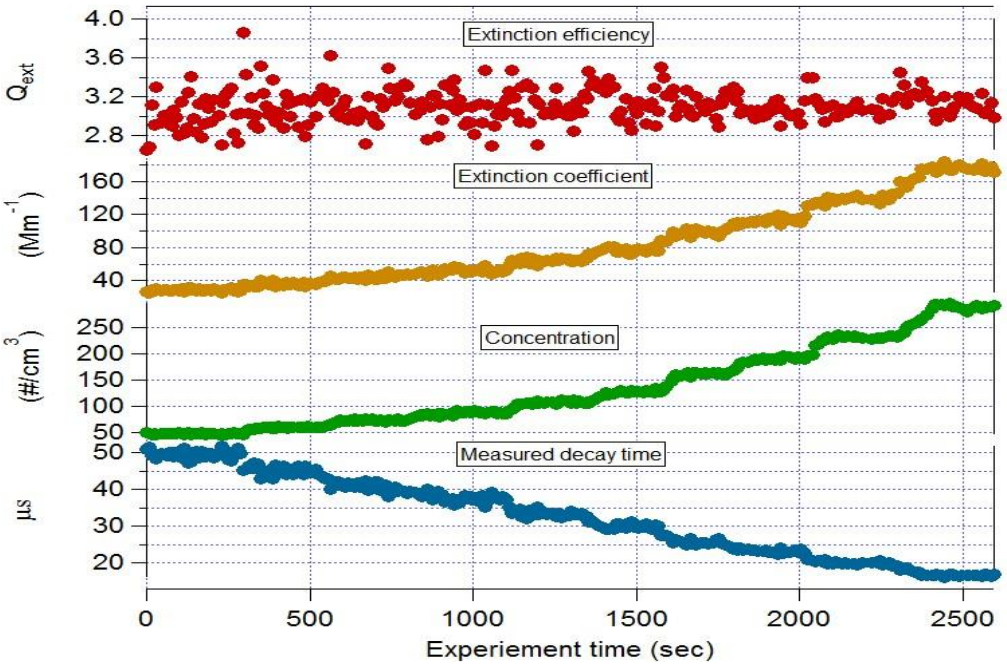

Figure 2.7. Example of the measurement output for 500 nm nigrosine particles for the cavity ring down used.

2.5 Photoacoustic spectroscopy

2.5.1 Basic principle

The photoacoustic (PA) effect was discovered in the late 1800s by Bell, but it was not until the development of laser technology that it was applied for scientific measurements. Since the late 1970's absorption by aerosols has been measured with photoacoustic measurements; [80, 81] however, only after the publication by Arnott *et al*. (1999)[82] was the PA method pursued in the aerosol community for measurements of absorption by aerosols, making the technique fairly new in the field.

The basic principle of the photoacoustic effect for aerosols†† is depicted in Figure 2.8. When a pulse of light is absorbed by a particle the temperature of the particle increases, the heat in the particle is then transferred by conduction to the surrounding air, causing the air to expand, and consequently creating a pressure disturbance; in other words, a sound wave. The temperature increase in the particle will also cause the particle to expand, but the volumetric expansion is negligible compared to that of the surrounding air. The increase of the particle's temperature is typically around 1K for typical size of aerosols measured (< 1μm) and laser power used[83]. The PA effect can be continuously generated in aerosol particles by periodically modulating a laser beam that is directed at the aerosols. However, the acoustic waves generated have a relatively small amplitude, making them difficult to measure with regular microphones. To help address this problem, acoustic resonators are used. Simple acoustic resonators consist of a well defined cavity; in an ideal case, the cavity will be closed, but in reality it is equipped with at least one opening for the microphone and gas and aerosol transport. There are many types of acoustic resonators, and each has their set of equations. See Miklos *et al*. (2001)[84] for a description of the different photoacoustic cell designs and the theory behind them. Moreover, the complete theoretical description of the generation of a PA signal in a resonant cell is complex, and beyond the scope of this manuscript (see Meyer *et al*. (1990)[85], Schäfer *et al*. (1997)[86], and Miklos *et al*. (2001)[84] for a full theoretical description); therefore, only a brief description of how the photoacoustic signal is defined and what are its dependencies will be presented. A detailed description of the photoacoustic sensor used in this study is given in the next section.

In an acoustic resonator the constructive interference caused by the boundaries can increase considerably the amplitude of the sound wave, and if the modulation frequency of the laser is equal to one of the acoustical eigenfrequencies of the cavity, the energy from the many modulation cycles is accumulated in a standing wave and the system works as an acoustic amplifier.[84] The amplitude at the resonance frequency is Q (the quality factor of the resonator, Q factor) times larger than the amplitude far from the resonance frequency. The physical definition of the Q factor is:[84]

†† The photoacoustic effect occurs in gases and liquids as well.

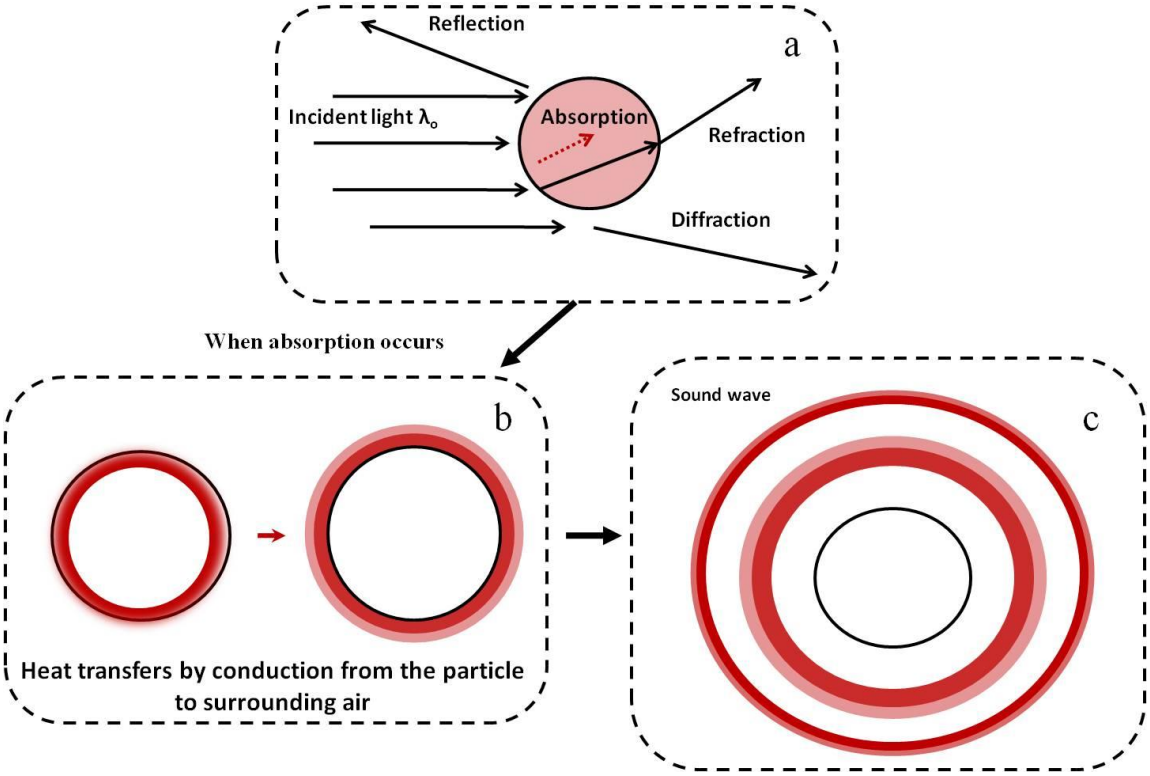

Figure 2.8 Depiction of the photoacoustic effect. When a pulse of light interacts with a suspended particle, the particle will scatter and absorb light (a). If the particle absorbs light, the energy absorbed from the electromagnetic wave will heat up the particle and the heat will be transferred to the surrounding air by conduction (b), this will expand the surrounding air, and create a pressure disturbance; in other words, a sound wave (c).

$$Q = \frac{f_o}{\Delta f} \tag{2.18}$$

where f_o is the resonance frequency, and Δf is the half-width value of the resonance frequency; in other words, it is the point where the amplitude is $1/\sqrt{2}$ the value of the peak amplitude, and is also referred to as the full width at half maximum.
The photoacoustic signal is defined as[85, 86]

$$S \equiv \alpha_{abs} CW \tag{2.19}$$

where S is the photoacoustic signal (given in Pa), α_{abs} the absorption coefficient (given in units of Mm^{-1}), C is the a proportionality factor (i.e. the cell constant), and W is the average laser power (in units of watts, $W = I_o \pi a^2$, where a is the beam radius). The cell constant depends on the microphone sensitivity, the geometry of the PA-cell, and the resonance frequency selected for detection, but it also includes the losses of the PA system. The value of the cell constant is determined by performing a calibration of the system; either with gases that have well defined concentrations and absorption cross-sections or by using a cavity ring

down to determine the absorption coefficient and correlating it to the microphone signal (see section 2.5). Therefore, by modulating the laser power at the resonance frequency of the acoustic cavity the propagated sound waves generated by the absorbing aerosols will be amplified and a maximal microphone signal will be generated. And by measuring the cell constant the absorption coefficient of an ensemble of particles can be directly measured.

2.5.2 Photoacoustic sensor

A schematic of the photoacoustic sensor (PAS) used in this study is shown in Figure 2.9. It has the same design as described in Miklos *et al*. (2001)[84] (see their figure 2, acoustic cell design b). For this instrument, a 1 Watt 532nm CW laser is introduced into a cylindrical acoustic resonator through one end. The amplitude of the laser is electronically modulated at the resonance frequency of the acoustic resonator with a square wave function. A sensitive microphone is placed at the center of the acoustic resonator. The signal of the microphone is then amplified using a Lock-in amplifier (Stanford Research Systems), and the signal is read through a LabView program.

Before performing a calibration of the system (calculating the cell constant) the resonance frequency of the cavity needs to be known as it is dependent on temperature and gas density. This is done by scanning the photoacoustic signal across a frequency range around the expected resonance frequency. Figure 2.10 shows an example of a measured peak resonance frequency (f_o) for this system. It can be seen that f_o is at ~1925Hz. The quality factor is calculated to be 30. It is a low Q for a resonant cavity, making the sensitivity to changes due to temperature and gas density small. A 1°C temperature change will have an effect of less than 1% in the measured signal.[84, 87]

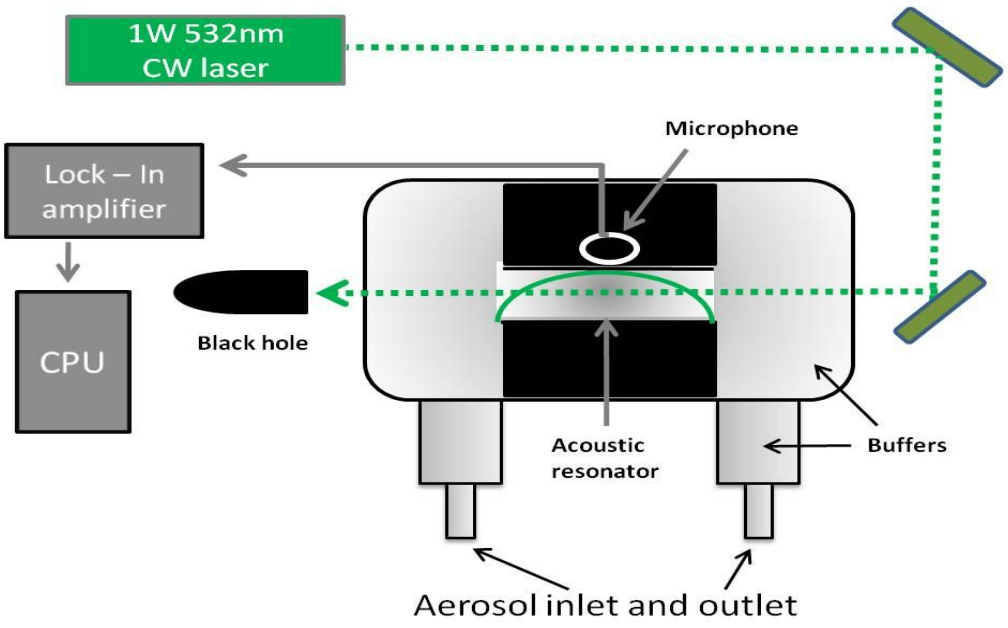

Figure 2.9 Schematic of the photoacoustic system.

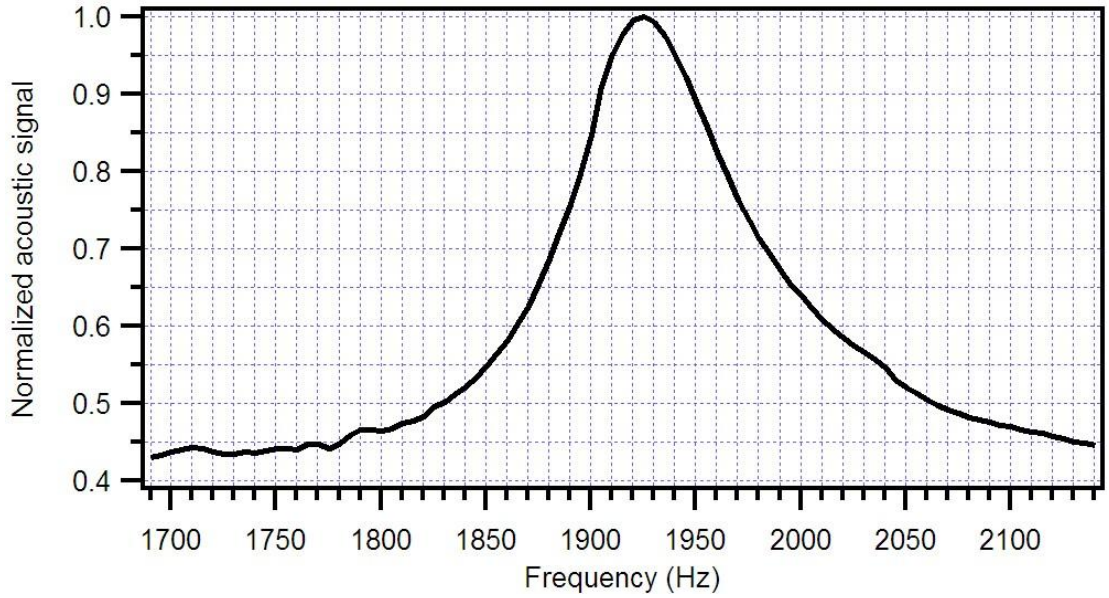

Figure 2.10 Measured resonance frequency for the photoacoustic system before performing a calibration. The resonance frequency can change with temperature, pressure, and gas density. The f_o measured here is approximately 1925Hz and the Q factor of the system is 30.

2.6 Photoacoustic sensor calibration

The calibration of the PAS was performed by measuring the absorption coefficient of ozone at different concentrations with a cavity ring down and relating it with the PA response of the PAS.[87] It is not necessary to know neither the ozone concentration in the instruments nor the absorption cross section of the ozone. The CRD gives a direct measurement of the absorption coefficient for gases.‡‡ An ozone gas flow of 100 cm^3 per minute was mixed with 900 cm^3 per minute of pure nitrogen before being introduced into the CRD and the PAS. The ozone was generated by flowing pure O_2 through a commercial UV-lamp. Figure 2.11a shows an example of a calibration performed with the CRD. Every point is an average of 60 one-second data points. The linear relationship between the absorption coefficient and the response from the PAS can be clearly seen. The precision of this calibration (2σ of the slope) is 2% for the full range. The laser power within the PAS is not monitored, but throughout a year of calibrations and measurements the calibrations showed repeated stability which indicates a very stable laser source.

‡‡ Calibrations can also be performed by measuring the light transmission through the photoacoustic cell and the photoacoustic response in the presence of NO_2, or theoretically.

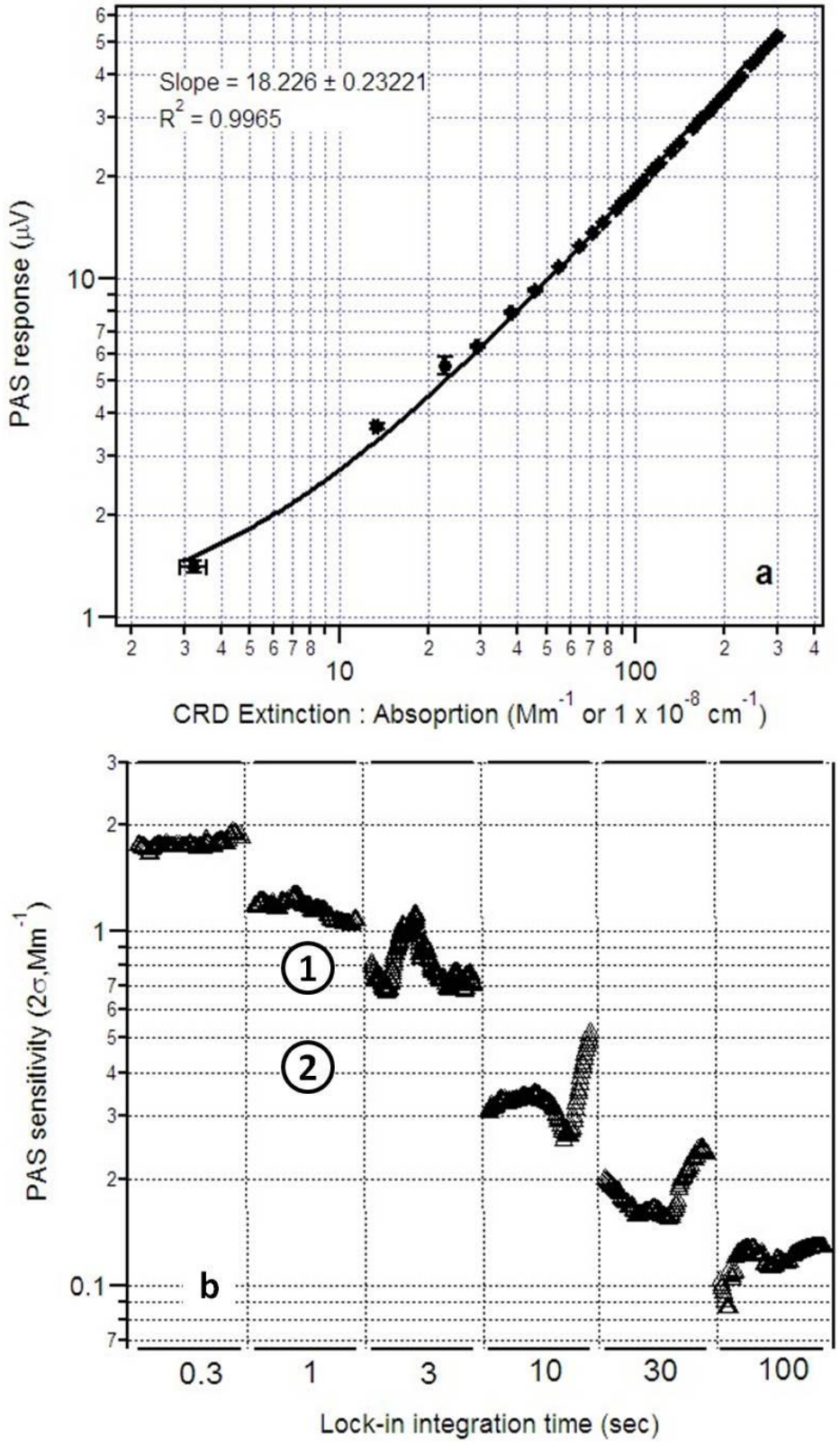

Figure 2.11. a) Example of a calibration of the PAS using ozone and the CRD. Every point is an average of a 60 second measurement at 1 sec integration time. The slope gives the cell constant. b) PAS sensitivity at different integration times of the lock-in amplifier. The numbers indicate different sensitivities reported in the literature for other photoacoustic sensors; 1-Lack *et al*. (2006)[87] with 0.8Mm^{-1} , and 2-Arnott *et al*. (2006)[88] with 0.4Mm^{-1}.

The sensitivity of the PAS is defined as 2σ of the background signal. By changing the integration time of the lock-in amplifier (the lock-in amplifier has 6 discrete integration times: 300ms, 1sec, 3sec, 10sec, 30sec, and 100sec), measurements of the background noise were performed at different flow rates, from 1 LPM (standard liter per minute) to 3 LPM, throughout several months. Figure 2.11b shows the sensitivity of the PAS at different integration times. For 1 second integration time this PAS shows an average sensitivity of $1.15Mm^{-1}$, and $0.18Mm^{-1}$ for a 30 second integration time. The consistency of the measurements indicates stability in the microphone response, and insensitivity to difference in the sample flows and ambient noise in the laboratory. The circled number inside Figure 2.11b are sensitivities reported in the literature; Lack *et al*. (2006)[87] reported a sensitivity of $0.8Mm^{-1}$ for a 1 second integration time, and Arnott *et al*. (2006)[88] $0.4Mm^{1}$.

2.7 Calibration verification

The PAS calibration with ozone and a CRD had been introduced by Lack *et al*. (2006)[87] and verified for their photoacoustic instrument; however, the instrument being described here was developed by Martin Schnaiter and his colleagues in the Karlsruhe Institute of Technology, in Karlsruhe, Germany, and only their group and ours have a unit of this model. Moreover, Schnaiter's group calibrates their PAS using NO_2; hence, the calibration using the CRD and ozone needed to be verified for measurements of absorbing aerosols.

For this verification Nigrosine dye was used. It is a water soluble black dye ($C_{11}N_2O_2H_{10}$) that has been used previously as a model of absorbing aerosols for instrument verifications and comparison.[71, 89, 90] Since it generates spherical particles [87] Mie theory can be used to calculate its complex refractive index. Different sizes of Nigrosine were selected to calculate their extinction and absorption cross-sections. The details of the experimental setup for particle generation, size selection, and counting are described in Appendix I. Figure 2.12 shows the linear responses of the extinction (a) and absorption (b) coefficients (equation 2.4) to concentration for three selected sizes. Each data point shown in Figure 2.12a/b is an average of the extinction and absorption measurements every 10.1 seconds for 2 minutes; the error bars show the variation during the 2 minute measurements. By doing linear fits of the data for each size, the values of the average optical extinction and absorption cross-sections were calculated, as the slope represents the cross-sections (equation 2.3). Furthermore, using the calculated cross-sections, $Q_{ext/abs}$ values were estimated. Table 2.1 shows the extinction and absorption cross-sections and efficiencies of every nigrosine particle size measured. The precision of the calculated cross-sections is also presented. The $Q_{ext/abs}$ values measured as a function of size are presented in Figure 2.13.

The complex refractive index of nigrosine dye was retrieved by comparing the measured extinction efficiency as a function of size parameter with the extinction efficiency calculated using Mie theory[37] at different complex refractive indices. This is achieved by

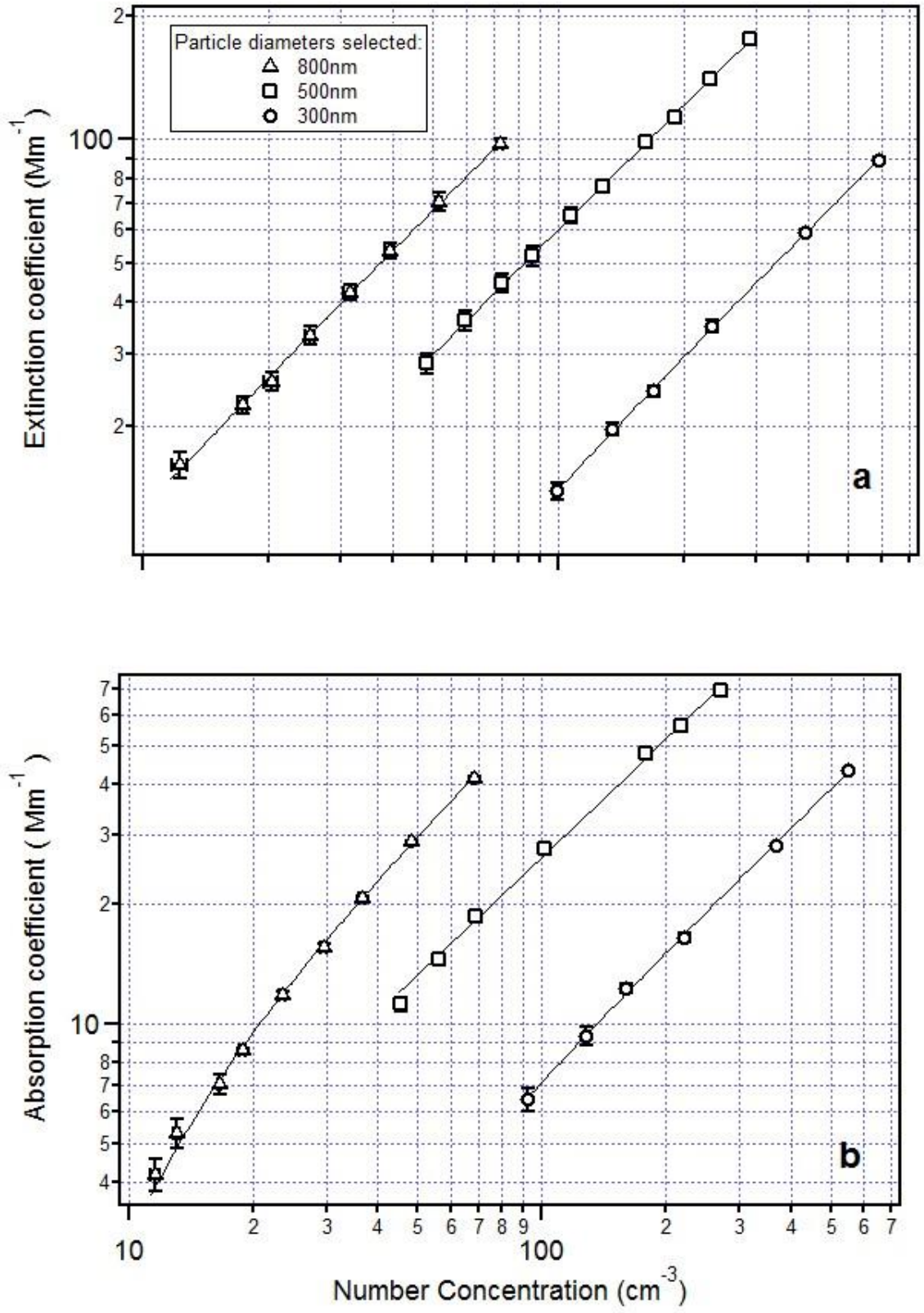

Figure 2.12 Extinction (a) and absorption (b) coefficient vs. number concentration of nigrosine dye for three selected sizes: 800nm (triangles), 500nm (squares), and 300nm (circles). Each data point is an average of extinction and absorption measurements sampled every 10.1 sec for 2 min; the error bars show the variation during the 2 min measurements. The lines are linear fits of the data, the value of the slope represents the optical extinction and absorption cross-sections.

minimizing the merit function χ^2,[71] where χ^2 is:

$$\chi^2(n,k) = \sum_{i=1}^{N} \frac{\left(Q_{ext\ measured} - Q_{ext_{(n,k)}}\right)_i^2}{\varepsilon_i^2} \qquad (2.20)$$

N is the number of particle sizes measured, *n* and *k* refer to the real and imaginary parts of the different complex refractive indices, respectively, and ε is the estimated error in the measurement (taken as the standard deviation of repeated measurements of the same particle size but for different concentrations).[91] The set of real and imaginary parts of the refractive indices that provides the minimum value of χ^2 in equation 2.20 gives the complex refractive index of the substance (see Appendix I for a specific example of the refractive index retrieval method).

Table 2.1 Extinction and absorption cross-sections (σ) and efficiencies (Q) for all sizes of nigrosine. The R^2 gives the precision of the line fit.

Size selected (nm)	Measured optical cross-sections σ(Mm^{-1}/cm^3) extinction / absorption	R^2 Extinction / absorption	Q values extinction /absorption
200	0.057(±0.001) / 0.031(±0.001)	0.9962 / 0.9914	1.81(±0.02) / 0.97(±0.01)
250	0.097(±0.002) / 0.053(±0.001)	0.9924 / 0.9981	1.97(±0.05) / 1.07(±0.01)
300	0.154(±0.003) / 0.080(±0.001)	0.9994 / 0.9995	2.18(±0.04) / 1.13(±0.01)
350	0.245(±0.005) / 0.109(±0.002)	0.9917 / 0.9946	2.55(±0.05) / 1.13(±0.02)
400	0.367(±0.008) / 0.164(±0.001)	0.9869 / 0.9965	2.92(±0.06) / 1.30(±0.01)
450	0.475(±0.010) / 0.223(±0.001)	0.9782 / 0.9941	3.06(±0.08) / 1.40(±0.01)
500	0.608(±0.013) / 0.260(±0.003)	0.9994 / 0.9608	3.09(±0.07) / 1.32(±0.01)
550	0.744(±0.030) / 0.355(±0.004)	0.9958 / 0.9714	3.13(±0.13) / 1.49(±0.02)
600	0.878(±0.030) / 0.343(±0.007)	0.9946 / 0.8563	3.11(±0.11) / 1.21(±0.03)
650	0.947(±0.032) / 0.469(±0.007)	0.9977 / 0.9888	2.85(±0.10) / 1.45(±0.02)
700	1.107(±0.022) / 0.535(±0.005)	0.9955 / 0.9927	2.88(±0.06) / 1.39(±0.01)
750	1.232(±0.026) / 0.625(±0.007)	0.9991 / 0.9997	2.79(±0.06) / 1.42(±0.02)
800	1.370(±0.047) / 0.678(±0.008)	0.9899 / 0.9714	2.73(±0.09) / 1.33(±0.02)

The complex refractive index that returned the minimum χ^2 was m = 1.626(±0.021) + i0.243(±0.023). The quoted uncertainties are one standard deviation from the minimum χ^2. They are calculated by studying the deviation of χ^2 in the vicinity of the minimum χ^2 found (χ^2_{min}). Assuming the errors of the measurement ε_i^2 to be normally distributed, the values of χ^2 for different measurements follow a χ^2 distribution for the two degrees of freedom *n* and *k*.[62, 65] The quantile for the 68.3% (1σ) confidence level for this parameter set is 2.298. Any measurement that falls within the 1σ error bound of the best measurement is considered acceptable if $\chi^2 < \chi^2_{min} + 2.298$. The derived RI for nigrosine is in very good agreement with the derived RI by Dinar *et al.* (2008)[62] of m = 1.649(±0.007)+i0.238(±0.008) using the same CRD system. Using Mie theory and the derived complex RI, the expected Q_{abs} was calculated (shown as the dotted line in Figure 2.11) and overlaid on the measured Q_{abs}. This shows an

excellent agreement, validating the calibration done with the CRD and O_3 for highly absorbing aerosols and providing an independent calibration of the PAS system (see next section). Only the measured Q_{abs} for 600nm falls quite low from the expected Q_{abs}, the reason for the deviation is unknown.

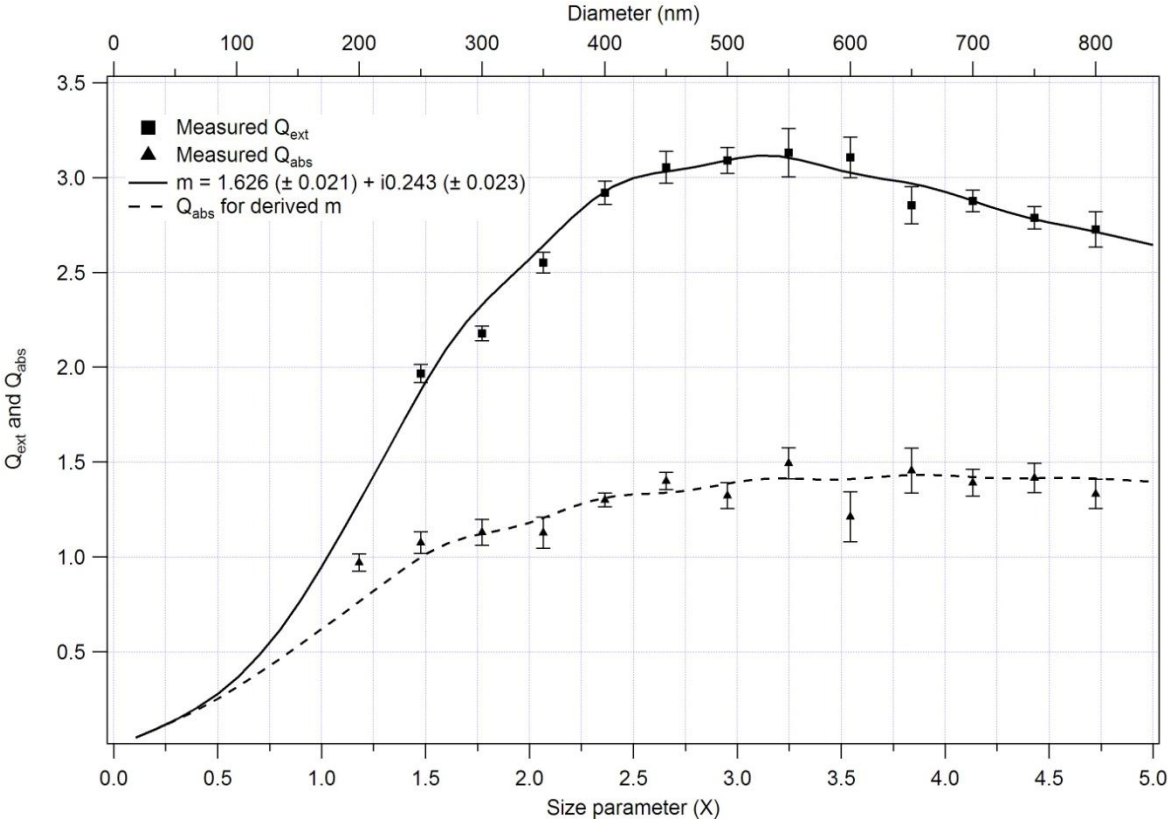

Figure 2.13 Measured Q_{ext} and Q_{abs} as a function of size for nigrosine particles. The black line is the complex refractive index retrieved by finding the minimum value of χ^2 in equation 20, and the dotted line is the corresponding Q_{abs} for the derived RI.

To validate the system for slightly absorbing aerosols, mixtures of 1:1 and 1:10 molar ratios of nigrosine to ammonium sulfate ($(NH_4)_2SO_4$, AS) were measured. The results for the 1:1 molar ratio mixture of nigrosine and AS are shown in Figure 2.14a. As it was done for pure nigrosine, the complex refractive index was derived using the Q_{ext} measurements from the CRD, and the corresponding Q_{abs} for this RI was overlaid to check the Q_{abs} measurements done with the PAS. The results of the measured Q_{abs} are in excellent agreement with the Q_{abs} from the derived RI. However, for an independent calculation of the value of the complex RI for internally mixed aerosols, optical mixing rules were used. Mixing rules are commonly used in climate models for calculating the refractive indices of internally mixed substances.[92] For the results shown here the volume-weighted linear average of the refractive indices[93] is used. The refractive index of AS in the aerosol phase has been previously measured [65, 71, 90, 94] and is well accepted. It is between 1.51 and 1.53 for the real part (with imaginary part of zero). A value of 1.53 was used for the calculations done here. For nigrosine the value derived in this study was used: m = 1.63 + i0.243. By doing a linear average of these two refractive indices; i.e., n= (1.63 + 1.53)/2 and k=0.243/2, gives a

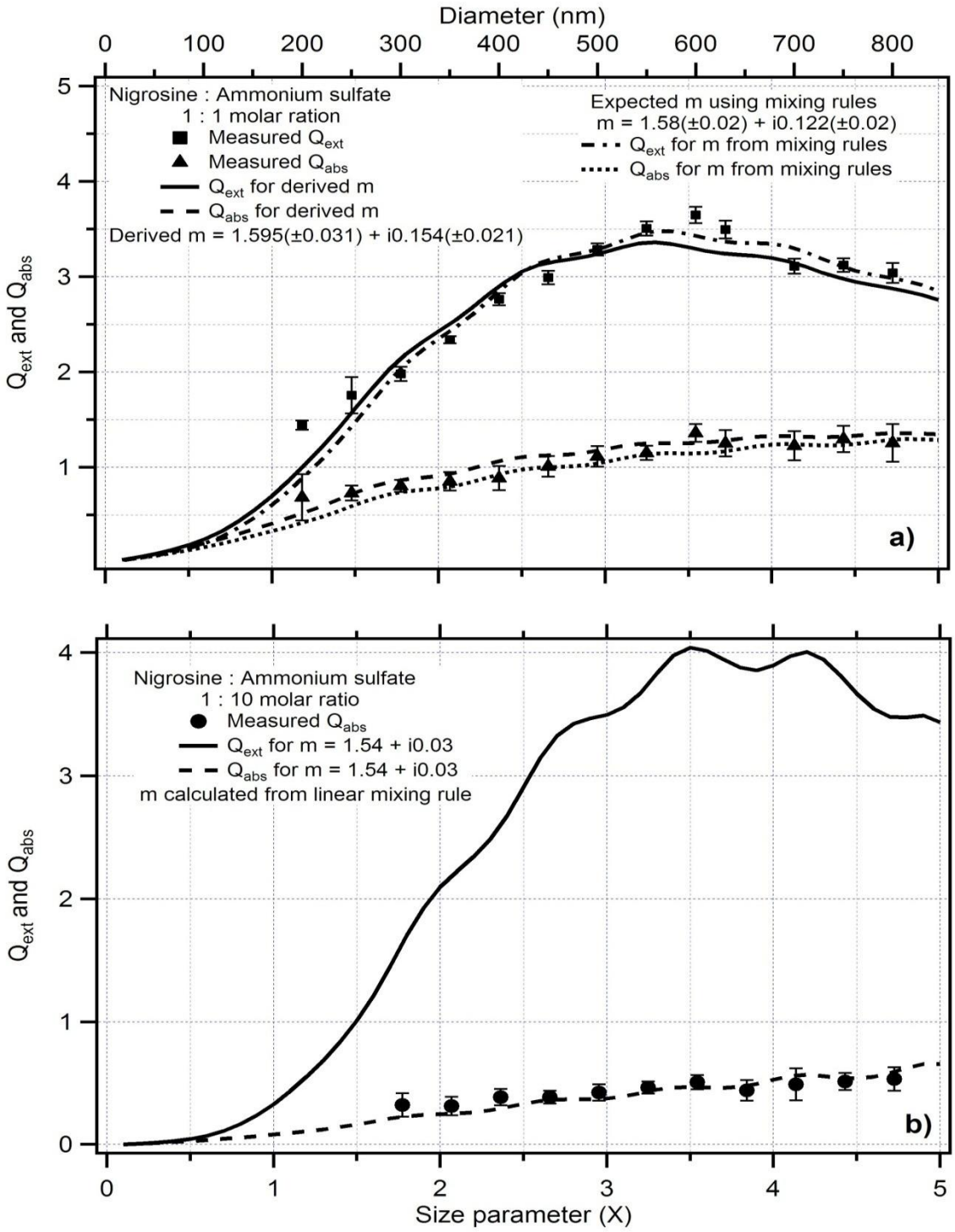

Figure 2.14 Measured Q_{ext} and Q_{abs} vs. size for two mixtures of nigrosine and ammonium sulfate. The top graph (a) shows the 1:1 nigrosine:AS molar ratio mixture. The measured Q_{ext}(solid squares) were used to derive the complex refractive index for this mixture (m=1.595+i0.154). The corresponding Q_{abs}(dashed line) from the derived RI is plotted to verify the measured Q_{abs}(solid triangles) from the PAS. The Q_{ext}(line-dot curve) and Q_{abs}(dotted curve) calculated from the expected RI using optical mixing rules are shown for comparison. The bottom graph (b) shows the measured Q_{abs}(solid circles) for a 1:10 nigrosine:AS molar ratio mixture. Due to technical problem the measurements for Q_{ext} could not be taken. The complex RI was calculated using the optical linear mixing rule. The corresponding Q_{abs}(dashed line) from the calculated RI in overlaid to verify the measured Q_{abs} from the PAS. The corresponding Q_{ext}(solid line) curve is shown for completeness.

complex RI for the 1:1 mixture of m = 1.58 + i0.122. The difference between the real parts of the derived RI with the CRD and the mixing rule is less than 1%. The imaginary parts have about a 20% difference, but as it can be seen in Figure 2.14a, it is a slight difference in terms of Q_{abs}. The measured Q_{abs} tend to fall in between both corresponding Q_{abs} from the derived and calculated RI implying that either method to obtain the complex refractive index can be used.

To verify the measured Q_{abs} for the 1:10 molar ratio of nigrosine to AS only the linear mixing rule was used to calculate the expected complex RI (due to technical issues the CRD could not be used for this set of measurements). A complex RI of m = 1.54 + i0.03 was calculated for this mixture, the corresponding Q_{ext} (plotted for completeness) and Q_{abs} curves, and the Q_{abs} measured with the PAS are plotted in Figure 2.14b. The measured Q_{abs} for this lightly absorbing aerosol also shows an excellent agreement with the expected Q_{abs}.

The measurement of these 3 different aerosol types, going from highly absorbing (i.e. nigrosine) to lightly absorbing (i.e. 1:10 molar ratio of nigrosine and AS) give a full validation of the calibration with ozone and the CRD and of the performance of the photoacoustic sensor. Furthermore, it opens a possibility of using not only highly absorbing aerosols, but lightly absorbing aerosols as well, for system calibration (see next section).

2.8 Aerosol calibration

2.8.1 Absorbing polystyrene spheres

To measure the absorption by aerosols, it would be ideal to calibrate the system using absorbing aerosols instead of other substances (such as absorbing gases). This is because calibration with other methods requires inter-comparison measurements among different absorption methods for verification. Having a standardized absorbing aerosol will help address this issue in the same way as polystyrene latex spheres (PSL) are used to calibrate instruments that measure optical scattering. Lack *et al*.(2006)[87] obtained samples of dyed monodisperse absorbing polystyrene latex spheres (APSL) and characterized them by measuring their extinction and absorption cross-sections and Q values. However, they could not determine a single complex refractive index that provided a good fit for the Q data, but concluded that the APSLs would have the following advantages: (1) it will allow calibration using particles. The APSL aerosol will eliminate any uncertainties that may be introduced due to volatile species on soot particles, the fractal nature of soot or the subtle differences in soot optical properties produced from different fuels and fuel ratios, when soot is used for calibration and inter-comparison purposes. And (2) APSLs will allow the interrogation of the absorption, scattering and extinction response of instrumentation using Mie theory, which may aid in investigations into scattering corrections (including particle stacking) for filter based methods. As no other study was found on the use of APSLs, four different sizes of the same batch used by Lack *et al*. (2006)[87] were obtained to measure and compare the extinction and absorption cross-sections and Q values. The optical cross-sections and Q

values were obtained using the same method as for nigrosine (see previous section). In Table 2.2 the measured optical cross sections, Q values, and single scattering albedo (ω) are compared to the measured values from Lack *et al.* (2006)[87], the percent difference is calculated for the three variables. It can be seen there is very good agreement in practically all measured parameters, especially in ω, with less than 3.5% difference. Only the absorption cross-section (and Q_{abs}) for 150nm and the extinction cross-section (and Q_{ext}) for 325nm have a considerable difference between them. The difference in the measured absorption for the 150/159nm APSL can originate from the instruments' sensitivity, as the optical absorption is near both instruments' detection limit. On the other hand, the difference in the extinction for the 325nm APSL between Lack *et al.*'s and the measurements performed in this study is unknown. The excellent agreement in the SSA (ω values) suggests that absorbing PSL particles can be used to investigate responses in the absorption, scattering and extinction of instrumentation using Mie theory, and can help with scattering corrections for absorption measurements using filter based methods. Furthermore, APSLs can be used as a calibration standard eliminating uncertainties due to the fractal nature, the occurrence of volatile species, and the differences from different fuels and fuel ratios of soot particles.

The only caveat of APSLs is the fact that the dyeing process is unknown and not standardized (Duke Scientific personal communication). This brings into question whether the next batch that is produced will have the same optical properties as this one. To address this potential problem, a method using nigrosine or a mixture of nigrosine with ammonium sulfate was also explored (see next section) as both substances' optical properties have been extensively characterized in the aerosol phase.[62, 65, 71, 72, 87, 90, 94]

2.8.2 Nigrosine or a mixture of nigrosine and ammonium sulfate

In the previous sections calibrations for the PAS using ozone and a CRD (O_3-CRD), and absorbing polystyrene latex sphere were explored. Even though, the O_3-CRD calibration was validated overlaying the Q_{abs} of nigrosine and the mixtures of nigrosine and AS calculated with the derived RI from the CRD measurements, or using the linear mixing rule onto the Q_{abs} measured with the PAS, it has the main problem that it is done using an absorbing gas for measurements that will take place in the aerosol phase. On the other hand, the measured optical properties of absorbing polystyrene latex were in excellent agreement with the optical properties measured by Lack et al. (2006) for the same batch indicating that they can be used as a standard; however, their dyeing process is unknown forcing a new optical characterization every time a new lot is produced. A third option would be to use another absorbing aerosol with defined optical properties that is widely available for different groups of researchers to use. In this section it is proposed that particles of nigrosine dye or a mixture of nigrosine with ammonium sulfate (AS) can be used as aerosol standards to calibrate the PAS. In Figures 2.11 and 2.12 it was validated that an accurate PAS cell

Table 2.2 Measured extinction and absorption optical cross-sections and Q values for absorbing polystyrene latex spheres. Comparisons with the study by Lack *et al*. (2006)[87] are also presented

Measured Diameter (nm)		Measured optical cross-sections $\sigma(Mm^{-1}/cm^3)$ extinction / absorption		% Difference extinction / absorption	Measured Q_{ext} / Q_{abs}		% Difference Q_{ext} / Q_{abs}	Singles scattering albedo (ω)		% Difference
This study	**Lack *et al*.**	**This study**	**Lack *et al*.**		**This study**	**Lack *et al*.**		**This study**	**Lack *et al*.**	
150	**159**	0.01656(±0.001)	0.01743(±0.0003)	5.1	0.94(±0.06)	0.88(±0.02)	6.6	0.75	0.78	3.5
		0.00433(±0.0003)	0.00377 (±0.00004)	13.8	0.24(±0.01)	0.19(±0.002)	23.3			
325	**315**	0.190(±0.004)	0.227(±0.002)	17.7	2.29(±0.05)	2.91(±0.03)	23.8	0.87	0.89	1.6
		0.0248(±0.0005)	0.0250 (±0.0005)	0.8	0.30(±0.01)	0.32(±0.01)	6.5			
610	**623**	1.143(±0.025)	1.206 (±0.006)	5.4	3.91(±0.08)	3.96(±0.02)	1.3	0.85	0.86	0.34
		0.171(±0.001)	0.174 (±0.002)	1.7	0.58(±0.01)	0.57(±0.01)	1.7			
805	**811**	1.71(±0.08)	1.77 (±0.01)	3.4	3.36(±0.16)	3.43(±0.02)	2.1	0.77	0.78	0.91
		0.406(±0.002)	0.39 (±0.01)	4.0	0.78(±0.01)	0.76(±0.02)	2.6			

constant can be obtained by measuring the absorption coefficient of ozone with the CRD and correlating it with the microphone response. But it was also illustrated that if the complex refractive index of a spherical absorbing substance is known, the Q_{abs} curve can be derived and hence the absorption cross-sections for all the sizes, which then can be used to acquire the PAS cell constant. To do this, an algorithm was developed to check how well a cell constant derived using aerosols will agree with the cell constant derived with the O_3-CRD method. A schematic of the logic of the algorithm is shown in Figure 2.13. It is a simple method where the response of the microphone (i.e. the photoacoustic signal S), at several sizes and different concentrations, is multiplied by a constant (*C*, i.e. the cell constant) to convert it to absorption coefficient values (equation 2.19). The α_{abs} values are used to calculate the cross-sections and, consequently, the Q_{abs} values for every size measured. Then the square deviation (χ^2) between these values and the Q_{abs} values obtained using Mie theory from the derived complex RI is calculated. The process is then repeated for a different *C*, by minimizing χ^2 the PAS cell constant is attained. This algorithm was applied to the data shown in Figures 2.11 and 2.12. The results are shown in Table 2.3. The average percent difference for the four retrieved cell constants is less than 4%. These results suggest that if the complex refractive index of a highly or lightly absorbing substance is known, the PAS can be independently calibrated without the use of a CRD, or an absorbing gas. It can also be used as a complementary method.

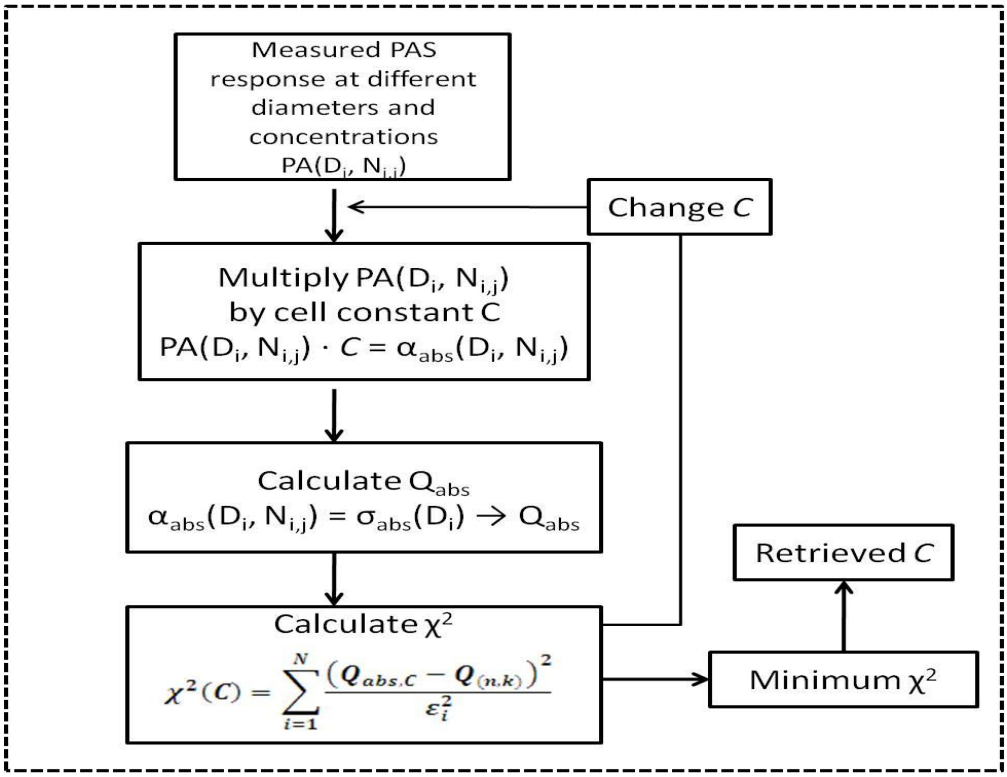

Figure 2.15 Schematic of the PAS cell constant retrieval's logic.

Table 2.3 Comparison between the cells constant derived with O_3-CRD calibration and the aerosol retrieval algorithm.

Aerosol	Complex RI used (m)	Derived cell constant *C*	O_3-CRD cell constant	% difference
Nigrosine	m = 1.626+i0.243	32.31	33.83	4.6
1:1 Nig:AS	m = 1.595+i0.154	31.81	33.83	6.2
	m = 1.580+i0.122	34.63	33.83	2.3
1:10 Nig:AS	m = 1.540+i0.030	32.93	33.83	2.7

2.9 Conclusions

A photoacoustic sensor (PAS) was fully characterized for measuring absorption by aerosols. It has an average sensitivity of 1.15Mm^{-1}, and 0.18Mm^{-1} for a 1 second and 30 second integration time, respectively. The instrument was initially calibrated using ozone and a cavity ring down spectrometer (CRD). This calibration method was independently validated by measuring different sizes of nigrosine dye, calculating their optical absorption cross-section, and comparing them to the predicted cross-sections using Mie theory.

Furthermore, the photoacoustic sensor was used to characterize absorbing polystyrene latex spheres (APSL). The measured optical absorption cross-sections were compared to the results from Lack *et al*. (2006)[87] for the same batch of APSLs, and very good agreement was found between both measurements. This suggests APSLs can be a potential calibration standard for aerosol absorption instruments.

Finally, a simple algorithm was developed to calculate the PAS cell constant using a mixture of nigrosine and ammonium sulfate solutions. It was shown that if the complex refractive index of a highly or lightly absorbing substance is known, the PAS can be independently calibrated without the use of a CRD, or an absorbing gas.

The O_3-CRD calibration was used for the measurements presented in Chapter 5.

3 Effective Broadband Refractive Index Retrieval by a White Light Optical Particle Counter

3.1 Motivation

The atmospheric aerosol is a critical component of the climate system. It scatters and absorbs solar and terrestrial radiation thus having direct cooling and warming effects on Earth's radiation budget.[95-102] The ability of aerosols to interact with radiation is determined by their optical properties, one of the main parameters in this respect are the scattering (real) and absorption (imaginary) components of the complex refractive index (RI). Aerosols with an organic component, originating from biogenic and anthropogenic emissions, [103, 104] as well as mixed aerosol that contain absorbing species and inclusions, can heat the atmosphere and affect atmospheric circulation and cloud properties.[101, 105-109] Despite the vast literature and experience, refractive indices of atmospheric aerosol are not well-determined, leaving a gap in the optical properties of aerosols, and consequently, leading to major uncertainties in assessing their current and future climatic impacts. Therefore, it is necessary to perform detailed laboratory experiments on the real and imaginary parts of the refractive index of aerosols.

Aerosols' optical properties have been extensively studied in the past. For example, integrating nephelometers are widely used to calculate the scattering component of the extinction coefficient of aerosols, [110, 111] while photoacoustic spectroscopy is used to calculate the absorbing component.[112-114] Recently, cavity ring down spectroscopy (CRD) using laser light, has been implemented to determine the real and imaginary part of the RI for a variety of aerosol species at specific wavelengths.[62, 70, 71, 115] Optical particle counters (OPC) have also been used to determine size distributions as well as optical properties of aerosols. To determine size distributions by means of OPCs, it is necessary to include *a-priori* values for the aerosol's refractive index. The value commonly adopted is that of polystyrene latex spheres (PSL), which is used for calibration. As a result, when the RI of the ambient aerosol is different from that of PSL, the derived size distributions may be incorrect. Methods to correct the size distribution of single wavelength OPCs and thereby to retrieve a RI have been pursued [48, 49, 53, 54, 116, 117]. Specifically, Stolzeburg *el al.*(1998)[54] derived the RI of ambient aerosol by using a specially designed high flow differential mobility analyzer (DMA)–OPC system. The DMA produces monodisperse aerosol population of known mobility diameter which was measured by the OPC, generating a time-dependant calibration, which was used to infer the real part of the RI. Hand *et al.*(2002)[49] overlapped size distributions from an aerodynamic particle sizer with those of an OPC to retrieve the real part of the complex RI of scattering aerosol. All these methods applied laser-based OPCs, hence the inferred refractive indices were at specific wavelengths. Additionally, multiangle scattering techniques together with Mie theory were developed to derive refractive indices of atmospheric aerosols.[42] Even with all these efforts to determine the optical properties of

aerosols at specific discrete wavelengths there is still a lack in optical properties determined with white light. Different evaluation procedures and calibration methods have been developed for white light OPCs.[43, 45, 50, 118, 119] Binnig *et al.*(2007)[44] utilized OPC calibration to provide PM2.5 mass of various aerosols. However, to the best of our knowledge, no attempt has been made to derive refractive indices of aerosols using a white light source.

The first attempt to use a white light spectrometer to retrieve effective broadband refractive indices ($m_{broad,eff}$) for a variety of scattering and absorbing aerosol particles is described in this study. The term effective is used as it was assumed the particle's chemical composition and morphology to be independent of particle size. The term broadband indicates an average over the wavelengths in the visible range. For this purpose, a retrieval method was developed which can also be easily applied as a calibration approach to improve the performance of OPCs both in the laboratory and in field settings. Furthermore, by using a white light source, the actinic light which the atmospheric aerosol interacts with, was mimicked (with the caveat of the differences between the solar spectrum and the white light source, see Figure 2.2). Therefore, crucial information concerning aerosols radiative properties can be obtained by using this method. For attaining information concerning aerosols' radiative properties a wide range of substances with different optical properties, including pure scatterers, lightly and highly absorbing particles, were examined.

To that end, two aerosol sizing techniques, each of which is based on a different physical principle were used. Using a differential mobility analyzer (DMA), a mobility diameter of aerosol particles was chosen and then the optical size obtained by the white light aerosol OPC (WELAS) was matched to it. This comparison allows the simultaneous measurement of optical scattering cross section and the mobility diameters, allowing the retrieval of the complex refractive index of the particles using Mie theory. To verify the retrieval method ammonium sulfate (AS, $(NH_4)_2SO_4$) and glutaric acid (GA), substances of well known refractive indices were measured. Subsequently, the refractive index for sodium chloride (NaCl), nigrosine, and Suwannee river fulvic acid (SRFA) were retrieved. Finally, various mixtures of nigrosine with pure scatterers (AS and GA) to measure different imaginary components of the complex RI were examined.

3.2 Methodology

The particle generation and size selection were done with the experimental setup described in Appendix I. The size-selected aerosol flow was diluted and sampled through a specially built manifold to ensure isokinetic sampling.[120] The inlet to the manifold was split into five to maximize the mixing of the particles in the manifold.

Particle sizes were selected from 300 nm to 800 nm, and measured in 50 nm steps. To ensure that coincidence effects did not affect the sizing of the particles, the particle concentrations used for the measurements were <400 p/cm^3. Moreover, each size was measured 8 to 10 times. To validate the size of the particles exiting the DMA, an

aerodynamic particle sizer (APS; TSI Model 3321) and a scanning mobility particle sizer (SMPS; TSI) were used. A condensation particle counter (CPC; TSI Model 3007) was used as the standard to calculate the counting efficiency of the WELAS. The counting efficiency is defined here as the ratio of the concentration measured by the WELAS divided by the concentration measured by the CPC for the same time period, particle size, and substance.

3.3 Substances

Six different substances were used for this experiment:

- Polysterene latex spheres (PSL), a standard used for instrument calibrations.
- Ammonium sulfate ($(NH_4)_2(SO_4)$), an inorganic substance commonly found in atmospheric aerosol.
- Sodium chloride (NaCl), an inorganic salt abundant in sea spray aerosol.
- Glutaric acid (GA), an organic acid.
- Suwannee river fulvic acid (SRFA), a model compound for atmospheric Humic like substances (HULIS).
- Nigrosine, an organic black dye used as a model for highly absorbing substances.

Detailed characteristics of the substances are given in Table 3.1. In addition, mixtures of ammonium sulfate and nigrosine (AS:N) in ratios of 1:1, 2:1 and 10:1, and glutaric acid and nigrosine (GA:N) with a 2:1 ratio to study aerosols with varying imaginary parts of the RI were investigated. Their refractive indices were calculated according to various optical mixing rules (see below) and compared with those retrieved from the WELAS measurements.

3.4 Optical mixing rules

Mixing rules are commonly used in climate models for calculating the refractive indices of internally mixed substances [92]. Three different mixing rules for estimation of the refractive indices of the mixtures were used: (1) Molar refraction and absorption; [121-124] (2) a volume-weighted linear average of the refractive indices, i.e., the "linear" mixing rule (see, e.g., d'Almeida *et al.* (1991), their Eq. 6.3);[125] and (3) the Maxwell-Garnett rule. [126, 127] A more detailed description on the various mixing rules is provided by Riziq *et al.* (2007).[71] The following RI values were used in the calculations: AS m=1.52+i0.0[71] and m=1.53+i0.0;[70] GA m=1.41+i0.0;[71] and nigrosine m=1.65+i0.24[62] and m=1.70+i0.31.[114]

Table 3.1 Chemical, physical, and optical parameters for PSL, nigrosine, glutaric acid, sodium chloride, ammonium sulfate, and Suwannee river fulvic acid.

Substance	Chemical properties	Sphericity	Refractive index at λ=532nm	Radiative property
Polystyrene Latex Spheres	Organic	Spherical	m=1.59 + i0.0	Non-absorbing
Ammonium Sulfate $(NH_4)_2SO_4$	Inorganic	Spherical	m=1.52+i0.0 [71] m=1.53+i0.0 [70]	Non-absorbing
Sodium Chloride (NaCl)	Inorganic	Non-spherical	m=1.54+i0.0 [71]	Non-absorbing
Glutaric Acid (GA)	Organic	Spherical	m=1.41+i0.0 [71]	Non-absorbing
Suwannee River Fulvic Acid (SRFA)	Organic	Spherical	m= 1.52 +i0.02 [115] m=1.65 + i0.02 [62]	Lightly-absorbing
Nigrosine – water soluble black dye	Organic	Spherical	m= 1.70 +i0.31 [114] m=1.65+i0.24 [62]	Absorbing

3.5 EBRI retrieval method

A simple method that corrects the optical diameter obtained by a white light OPC to match the mobility diameter chosen in the DMA, and by doing so, obtaining the effective broadband refractive index of the aerosol in the visible range, is demonstrated. This approach resembles experiments that employed tandem DMA-OPC laser-based OPCs setups. [54, 128, 129] A schematic presentation of the retrieval logic is shown in Figure 3.1.

The average scattering cross section ($\sigma_{sca,avg}$) is calculated using a Mie code. [126] The scattering cross section (σ_{sca}) is a function of the particle diameter (D_p), the wavelength (λ), the scattering angle (θ), the complex RI (m) and the polarization angle (ϕ) (however, for unpolarized light, the scattering function is independent of the polarization angle). For every wavelength of the white light source (410 wavelengths, from 370 to 780 nm), σ_{sca} is determined by calculating the phase function (φ) and accounting for the geometry of the sensor by calculating the solid angles (Ω) of the scattered light from a particle:

$$\sigma_{sca}(D_p,\theta,\lambda,m) = \sum_{\theta=79}^{101} \phi\big(D_p,\theta,\lambda,m\big)\Omega(\theta) \tag{3.1}$$

Finally, the average scattering cross section is obtained by averaging over the spectrum of the white light source, normalized to the highest intensity in the spectrum:

$$\sigma_{sca,avg}\big(D_p,\theta,\lambda,m\big) = \sum_{\lambda=370}^{780} \Big(I_s(\lambda)\sigma_{sca}\big(D_p,\theta,\lambda,m\big)\Big) \tag{3.2}$$

where $I_s(\lambda) = I_\lambda / I_{max}$, and I_λ is the intensity of a specific wavelength of the white light spectrum, and I_{max} is the maximum intensity in the spectrum.

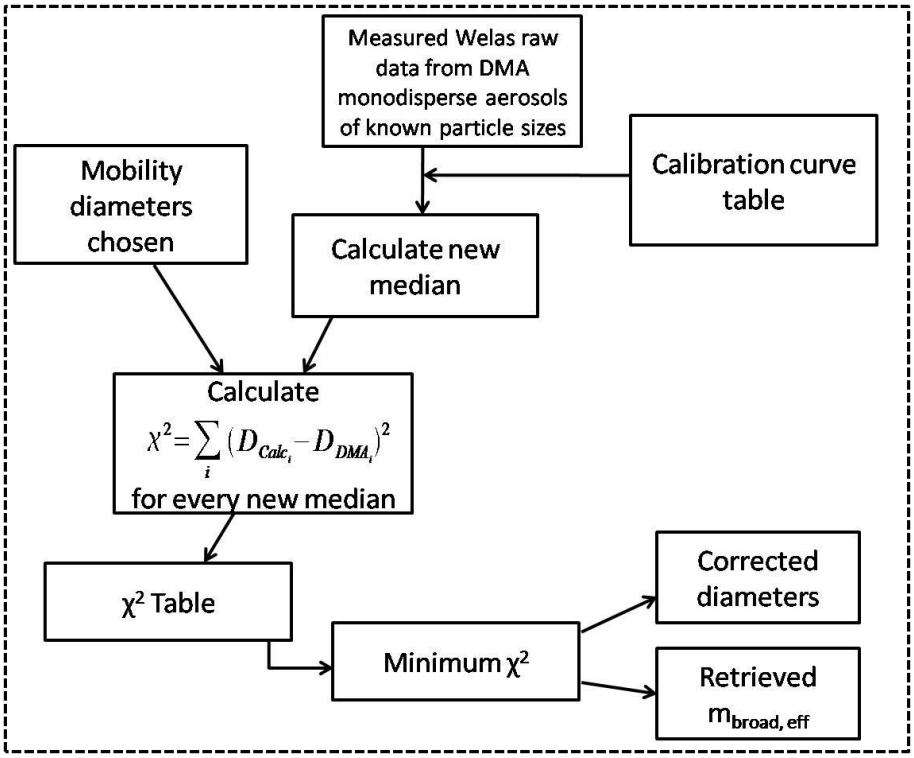

Figure 3.1. Schematics of the index of refraction retrieval method.

By calculating σ_{sca} for m = 1.59 + i0.0 (the RI of PSL) and equating it to the corresponding channel number assigned in the calibration curve provided by PALAS (PSL-based and experimentally created), a specific value of the σ_{sca} is assigned to a corresponding channel. The resolution of the calibration curves (number of channels per every 100 nm) was also based on the calibration curve supplied by the company. A look-up table of calibration curves was created from a real component of 1.3 to 1.7 in 0.01 steps, and imaginary part from i0.05 to i0.3 in 0.01 steps. Some examples of calibration curves are shown in Figure 3.2.

The retrieval algorithm uses the generated calibration to match measured optical median diameters with the median mobility diameter for each of the substances measured. This is done by determining a median optical diameter for each calibration curve and calculating the mean square deviation (χ^2) of the obtained median optical diameter and the mobility diameters chosen. By identifying the best calibration curve, which minimizes the mean square deviation, the effective broadband index of refraction is retrieved. Measurements within 5% of the minimum χ^2 are also taken as valid, assuming the errors of the measurement to be normally distributed; the values of χ^2 for different measurements follow a χ^2-distribution for the two degrees of freedom n and k. The RI was derived from the WELAS measurements using an aerosol size range from 400-800nm. The lower part of this range was chosen by measuring the counting efficiency of the WELAS and observing that for most substances the WELAS undercounts below 400nm. This was also observed by Heim *et al.*[50] Undercounting of particles causes biases in the derived size distribution towards larger sizes and must be empirically corrected in any quantitative measurements of size distributions by WELAS. Therefore, to avoid over-sizing biases caused by the undercounting below

400nm, the diameters smaller than 400nm for the refractive index derivations were excluded. A software was written in the graphing interface IGOR Pro 6 (WaveMetrics, Inc.) to perform the derivations of the refractive indices.

3.6 Calibration curves analysis

Accurate $m_{broad,eff}$ retrievals critically depend on the calibration curves created theoretically. Figure 3.2 shows four sets of calibration curves created by the algorithm: each set of curves spans from a real component of the complex RI of 1.4 to 1.6 and has a fixed imaginary component (k): k=0 (blue-dashed curves), k=0.08 (red-line-dot curves), k=0.2 (green-dash-dot curves), and k=0.3 (black-line curves). The k=0 curves have the same slope and equivalent resolution (they span over 90 channels) as the PSL curve, allowing clear differentiation between each of the calibration curves; i.e., clear differentiation between each RI. Therefore, an accurate retrieval for purely scattering substances is expected. Moreover, the slope of the curves with k=0 is significantly different from the curves with an imaginary component of $k \geq 0.05$; consequently, there is no confusion between the retrieved RI of the k=0 set and the complex $m_{broad,eff}$ with $k \geq 0.05$.

When the imaginary part is greater than i0.05, the slope of the calibration curves drastically decreases, but there is still a clear differentiation among the different curves. However, as the imaginary component increases, the resolution decreases; for example, the calibration curves with k=0.08 (red- line-dot curves) only span through 50 channels (compared to 90 for k=0), and those with k=0.3 (black-line curves) only span about 20. This means that, with increasingly larger values of the imaginary component, it is less likely to derive an accurate complex refractive index. Moreover, for sizes smaller than 400nm, the calibration curves with an imaginary component tend to mesh together. There is no clear separation among them, and the resolution is limited (only about 5 channels). As a result, an accurate retrieval of the complex RI using sizes smaller than 400nm is practically impossible.

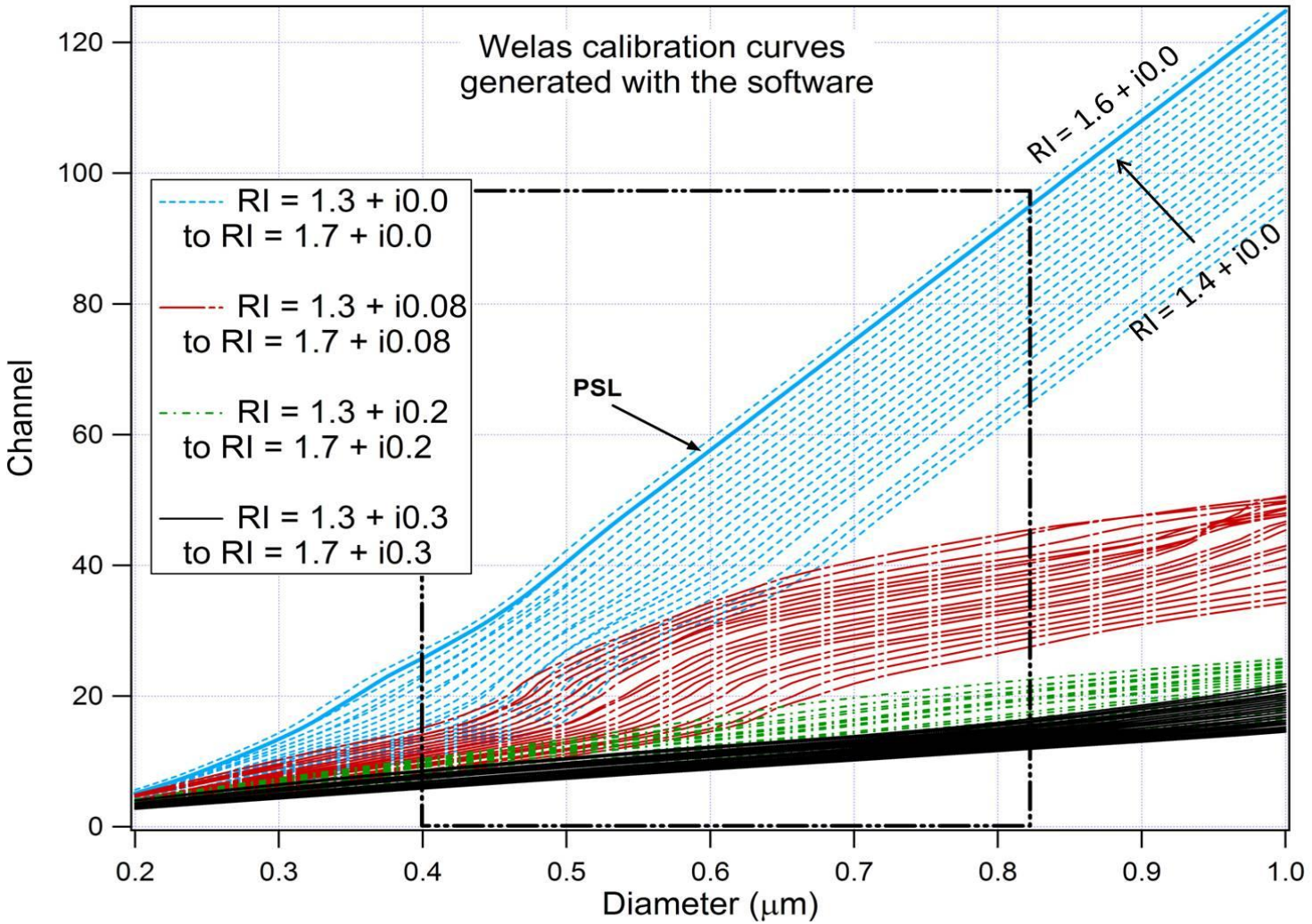

Figure 3.2 WELAS channel vs. size for five sets of created calibration curves. The real component spans from 1.4 to 1.7 keeping the imaginary part constant for each set. The bold blue line is the experimentally created calibration curve from the company.

3.7 Results & Discussion

The corrected diameters compared to the optical diameters measured by the WELAS, and the corresponding retrieved refractive indices for all substances are shown in Figure 3.3. The measured diameters are corrected by the retrieval method, aligning the measured optical diameters with the mobility diameters. All $m_{broad,eff}$ retrieved in this study are shown in Table 3.2. The $m_{broad,eff}$ of the single-component aerosols were compared to the literature values, while the $m_{broad,eff}$ derived for the mixtures were compared to those calculated by the various mixing rules. The percent difference between the retrieved values and the given RI was calculated.

For the pure scatterers (Figure 3.3a) the retrieved $m_{broad,eff}$ for AS is m=1.52+i0.0, which is the value reported by Riziq *et al*.(2007)[71] and within 0.6% of m=1.53+i0.0, found by Pettersson *et al*.(2004).[70] For GA, a $m_{broad,eff}$ =1.45+i0.0 was retrieved, which is within 2.8% of m=1.41+i0.0 found by Riziq *et al*.(2007),[71] and for NaCl, a $m_{broad,eff}$=1.49+i0.0 was derived, which is within 3.5% of m=1.54+i0.0 found by Riziq *et al.* (2007).[71] For AS, GA, and NaCl, the complex RI is considered to be constant throughout the visible wavelength range and considered equivalent to that found in the literature for λ=532nm.

Figure 3.3b shows the retrieved $m_{broad,eff}$ for lightly absorbing substances: SRFA, and the mixture of AS:N with a 10:1 ratio. For the mixture we derived $m_{broad,eff}$ =1.59+i0.08. The calculated values using the mixing rules are between 1.54 and 1.56 for the real part, and i0.02–i0.04 for the imaginary part. There is a slight overestimation of the real part of the $m_{broad,eff}$ as well as the imaginary part. The percent difference for the imaginary part reaches almost 100% which is within the measurement error observed in the CRD method results for low or even zero values of the imaginary component of various substances, see for example Lang-Yona *et al.* [115]. On the other hand, the value obtained for SRFA by the retrieval method is $m_{broad,eff}$ =1.53+i0.0. The complex RI of this specific extract at λ=532nm using a continuous wave cavity ring down method is m=1.52(±0.03)+i0.018 (±0.008).[115] The real part is in excellent agreement with our result (0.7% difference). To verify the derivation for the imaginary part, the imaginary component (k) was calculated. For this purpose, the absorption spectrum of this SRFA extract was measured with a UV-VIS spectrometer. The values obtained from the spectrum of the sample were normalized by the white light spectrum of the WELAS. Then, the absorption coefficient, α (cm^{-1}), was calculated for each wavelength using the Beer-Lambert law:

$$\left(\frac{I}{I_o}\right)_i = e^{-\alpha_i L} \tag{3.3}$$

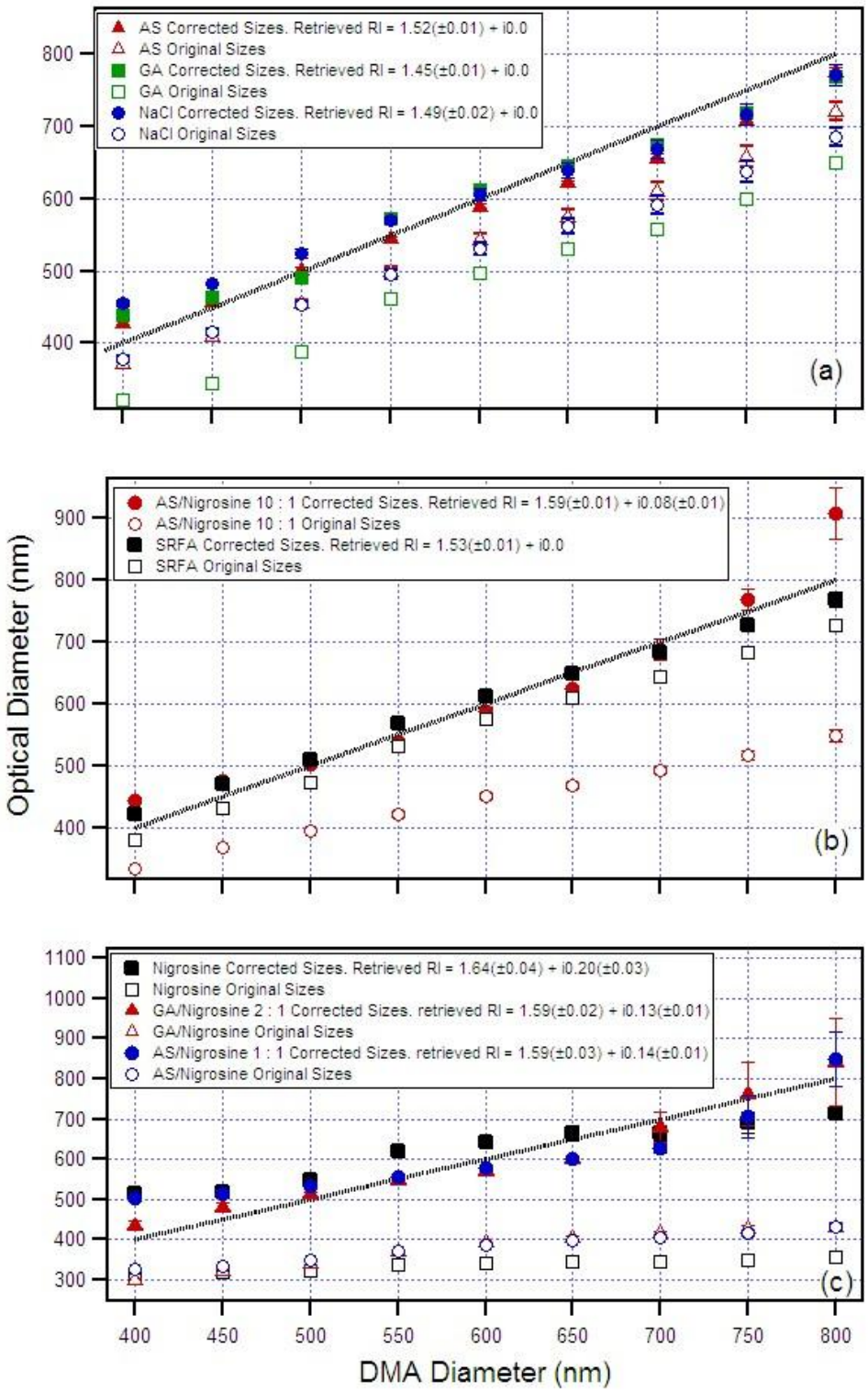

Figure 3.3 Optical median diameter *vs.* mobility diameter for (a) non-absorbing substances: ammonium sulfate, glutaric acid, and sodium chloride; (b) Lightly absorbing substances: Suwannee river fulvic acid and the mixture of AS:Nigrosine with a 10:1 ratio; and (c) Highly absorbing substances: Nigrosine and the mixtures of AS:Nigrosine with 1:1 ratio, and GA:Nigrosine with 2:1 ratio. The medians measured by the WELAS are shown by the empty markers. The full makers indicate the corrected medians. The retrieved refractive indices for each substance are shown in the legends. Every data point represents the average over 8-10 repetitions. The dash lines show the 1 to 1 line between the optical median diameter and the mobility diameter.

where I/I_0 is the relative intensity obtained from the normalized UV-VIS spectrum, and L is the path length of the spectrometer's cuvette. The imaginary part was separately calculated for each wavelength and averaged over the spectrum: [27]

$$k = \frac{\sum \alpha_i \lambda_i}{4\pi N} \tag{3.4}$$

where λ is the wavelength, and N is the total number of wavelengths. This calculation provides a value of k=0.00003. This value can be considered negligible. Thus, the imaginary part was also retrieved correctly as i0.0. The fact that SRFA is identified by the WELAS as a non-absorbing substance, although it is not a pure scatterer throughout the entire UV-VIS range, can be explained by the shape of the instrument's light spectrum which indicates that it is not sensitive below 380nm. Hence, a substance such as SRFA, which mostly absorbs between 200nm and 400nm, will not be detected by the WELAS as an absorber.

Figure 3.3c shows the retrieved refractive indices for 3 of the 4 highly absorbing substances. For nigrosine, $m_{broad,eff}$ =1.64+i0.20 was retrieved. This result is in excellent agreement with Dinar *et al.*(2008)[62] and Lack *et al.*(2006)[114] who retrieved m=1.65+i0.24 and m=1.7+i0.31, respectively, using CRD spectroscopy at λ=532nm. For the mixtures of GA:N and AS:N 2:1 ratio, $m_{broad,eff}$ =1.59+i0.13 and $m_{broad,eff}$ =1.61+i0.28 were retrieved, respectively. The value of the real part of the RI of GA:N was calculated, using mixing rules, to be between 1.50 and 1.53, and for the imaginary part between i0.09 and i0.13. As for the AS:N mixtures, values between 1.58 and 1.62 for the real component and values between i0.09 and i0.15 for the imaginary component were calculated. While the real part of the RI of the AS:N mixture is successfully retrieved by our method, the imaginary part is overestimated. In case of the GA:N, however, it is the real part which is overestimated (though only by up to 6%) and the imaginary part is in very close agreement to the values calculated with the mixing rules. As for the mixture of AS:N 1:1 ratio, $m_{broad,eff}$ =1.59+i0.14 was retrieved. The real component calculated by the mixing rules was between 1.6 and 1.65 and the imaginary between i0.14 and i0.19. As in the case of the purely scattering substances, we expect nigrosine and its mixtures to have a nearly-constant RI throughout the white light range, allowing us to compare the WELAS results to results from laser measurements at λ=532nm.

The method described herein can be used as a complementary method to those using a single wavelength, such as CRD spectroscopy, to determine the RI of aerosol particles. While CRD spectroscopy has the advantage of being spectrally resolved, which makes it sensitive to colored aerosol particles, it has the disadvantage of needing several wavelengths to cover the whole spectrum relevant to the atmosphere, and is not as easy to handle as the tandem DMA-white light OPC. On the other hand, deriving the RI with a white light spectrometer has the advantage of averaging over the spectrum relevant to the atmosphere and being easy to operate. However, it cannot resolve external mixtures and it is not sensitive to absorbers with

Table 3.2 Refractive indices taken from the literature and calculated by three different mixing rules compared to the $m_{broad,eff}$ retrieved using the WELAS measurements. The percent difference is calculated for the retrieved values vs. the reference values. The $m_{broad,eff}$ was also retrieved using the solar spectrum instead of the white light source from the WELAS, these values are shown for comparison.

	Substance	Mixing rule	Reference values of the refractive index for λ=532nm (literature and calculations)	WELAS retrieved $m_{broad,eff}$ (χ^2 from 400-800 nm)	% Difference	WELAS retrieved $m_{broad,eff}$ (solar spectrum)
Scatterers	Ammonium Sulfate		**1.52**(±0.01) **+ i0.00**(±0.01) [71]		**0 + i 0**	
			1.53(±0.0) **+ i0.0**(±0.0) [70]	**1.52(±0.01) + i0.0**	**0.7 + i 0**	**1.51(±0.01) + i0.0**
	Sodium Chloride		**1.54**(±0.01) **+ i0.0**(±0.003) [71]	**1.49(±0.02) + i0.0**	**3.3 + i 0**	**1.50(±0.01) + i0.0**
	Glutaric Acid		**1.41**(±0.0) **+ i0.0**(±0.0) [71]	**1.45(±0.01) + i0.0**	**2.8 + i 0**	**1.45(±0.01) + i0.0**
Lightly	**Suwannee River Fulvic Acid**		**1.52**(±0.03) **+ i0.00**(±0.01)*****[115]		**0.7 + i 0**	
			1.65(±0.01) **+ i0.02**(±0.005) [62]	**1.53(±0.01) + i0.0**	**7.6 + i 200**	**1.55(±0.02) + i0.0**
	Ammonium Sulfate/Nigrosine 10:1 ratio	Molar refraction/absorption	**1.56** (±0.01) **+ i0.05** (±0.01)		**1.9 + i 46**	
		Linear	**1.54** (±0.01) **+ i0.03**	**1.59(±0.01) + i0.08(±0.01)**	**3.2 + i 90**	**1.57(±0.01) + i0.06(±0.01)**
		Maxwell-Garnett	**1.55** (±0.01) **+ i0.05** (±0.01)		**2.6 + i 46**	
Highly absorbing	**Ammonium Sulfate/Nigrosine 1:1 ratio**	Molar refraction/absorption	**1.65** (± 0.02) + **i0.19** (± 0.03)		**3.7 + i 30**	
		Linear	**1.60** (± 0.02) +**i0.14** (±0.02)	**1.59(±0.03) + i0.14(±0.01)**	**0.6 + i 0**	**1.62(±0.02) + i0.12(±0.01)**
		Maxwell-Garnett	**1.63** (±0.02) **+ i0.17** (±0.02)		**2.5 + i 19**	
	Ammonium Sulfate/Nigrosine 2:1 ratio	Molar refraction/absorption	**1.62** (±0.02) **+ i0.15** (±0.02)		**0.6 + i 60**	
		Linear	**1.58** (±0.01) **+ i0.09** (±0.01)	**1.61(±0.08) + i0.28(±0.18)**	**1.9 + i 103**	**1.58(±0.04) + i0.09(±0.01)**
		Maxwell-Garnett	**1.61** (±0.02) **+ i0.14** (±0.02)		**0 + i 67**	
	Glutaric acid/Nigrosine 2:1 ratio	Molar refraction/absorption	**1.53** (±0.02) **+ i0.13** (±0.02)		**3.8 + i 0**	
		Linear	**1.50** (±0.01) **+ i0.09** (±0.02)	**1.59(±0.02) + i0.13(±0.01)**	**5.8 + i 36**	**1.59(±0.02) + i0.11(±0.01)**
		Maxwell-Garnett	**1.53** (±0.02) **+ i0.12** (±0.02)		**3.8 + i 8**	
	Nigrosine		**1.65**(±0.01) **+ i0.24**(±0.01) [62]		**0.6 + i 18**	
			1.70(±0.0) **+ i0.31**(±0.0)[114]	**1.64(±0.04) + i0.20(±0.03)**	**3.6 + i 43**	**1.7(±0.03)+ i0.20(±0.01)**

* - Value is taken from a measurement with laser light at λ=532nm and corrected for the white light spectrum of the WELAS.

spectral dependence, such as dust or humic like substances. Finally, this method for the WELAS, specifically, is limited to particles larger than 400 nm.

3.8 Field applications

The method described above was adapted for characterization of the $m_{broad,eff}$ evolution of submicron aerosols from a large anthropogenic biomass burning (BB) event in Israel. Hand and Kreidenweis (2002)[49] showed that by aligning the size distribution of an optical particle counter to that of the SMPS (in their overlap region) a refractive index can be derived. The same principle is applied here, only that the generated calibration curves also cover the imaginary plane, allowing the retrieval of a complex RI. As a caveat it should be emphasized that the method is applied for the first time for non-spherical particles, which were mostly present during the intensive fires. The WELAS size distributions were cut for particles above 1 μm diameter to match the calibration curves, and because the population of particles greater than 1 μm can vary significantly in composition and morphology from the accumulation mode population.

The measurements took place between the 11 and 12 May 2009 in an urban area on the roof of a 4-story building located at the Weizmann Institute of Science in Rehovot, Israel (31° 53' N, 34° 48' E). The chemical properties of the non refractory submicron diameter aerosols were sampled using a Time of Flight Aerosol Mass Spectrometer (TOF-AMS, Aerodyne). The size distributions and particle number concentrations for aerosol particles with a diameter below 700nm were measured using a Scanning Mobility Particle Sizer (SMPS, TSI model 3080). A Condensation Particle Counter (CPC, TSI 3022) was used for counting particles with diameters larger than 3 nm. The three instruments were located on the third floor; a sampling line of 3/8'' conductive tubing from the roof to the instruments was used for sampling. The flow was split and sampled by the SMPS and by the AMS and CPC. The TOF-AMS sampled at a constant flow of 80 cm^3 min^{-1}, while the SMPS and the CPC have constant flows of 300cm^3 min^{-1} each. The SMPS performed a measurement every 5 min, the HR-TOF-AMS was set to measure 1 min averages, while the CPC sampled continuously. The particle loss calculator[130] was used in order to estimate the particle losses via the tubing. The lengths of the tubes as well as the angles of curvature were taken into account. Figure 3.4 shows the calculated particle loss through the inlet as a function of particle size. The maximum loss was found to be 6.5% for 700 nm particle. The SMPS size distributions were corrected using the calculated losses. The WELAS was placed at the roof providing optical size distributions every 2 min. In addition, ozone concentrations and meteorological data from a monitoring air quality station located approximately 800m from the campaign site was used. The full study is published in ACP[131] and the reader is referred to this publication for a full description of the measurements. Only a description of the retrieval method, the retrieved $m_{broad,eff}$ and a comparison to the values found in the literature will be given here.

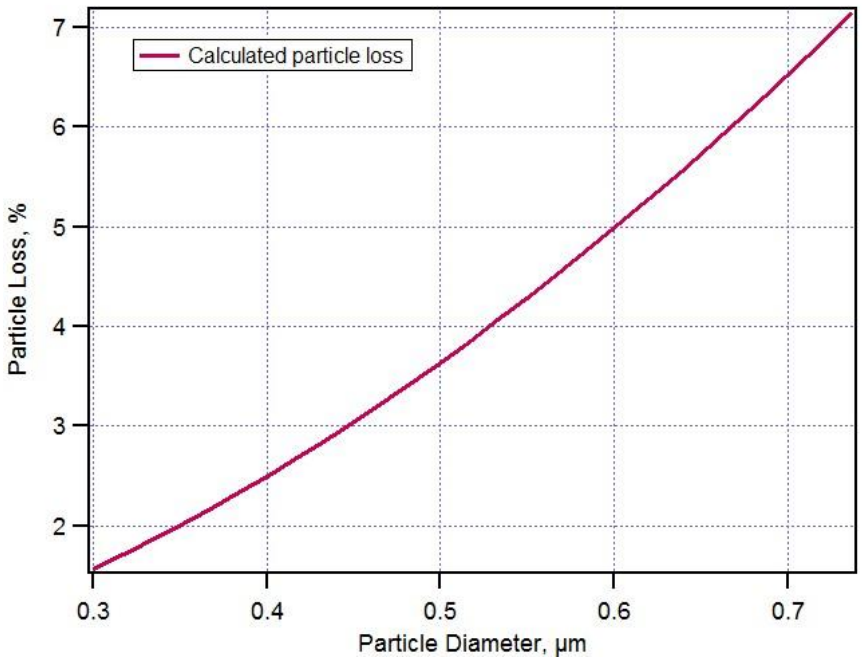

Figure 3.4.Calculated particle loss as a function of particle diameter for the inlet used for the SMPS measurements.

A retrieval algorithm was developed to correct the size distributions of the WELAS and match them to those of the SMPS in their overlap region; a schematic of the algorithm's logic is shown in Figure 3.5. In general, the retrieval algorithm relies on aligning mobility size distribution (obtained by SMPS, assuming spherical particles) with the WELAS-derived optical size distribution (assuming a refractive index of PSL). The $m_{broad,eff}$ is the refractive index that minimizes the difference between the size distribution measured by the SMPS and the WELAS, in other words; the $m_{broad,eff}$ is the refractive index required to produce the correct calibration curve for the WELAS, so that it would size the particles correctly with respect to the SMPS.

Since the $m_{broad,eff}$ was developed for homogeneous spherical particles (see above or Flores et al. (2009)[90]), large errors are expect when the aerosol population is not dominated by one species. Figure 3.6 depicts the real and imaginary parts of the complex $m_{broad,eff}$ as a function of time. In addition, the organic mass signal is presented as a reference to the timeline of the event and the following day. Due to instrumental problems, a significant portion of the burning peak itself was not measured by the WELAS. Nevertheless, the beginning (open fires) and the end (smoldering) of the burning event (periods 1 and 2, respectively) can be analyzed in comparison to the day following the burning (period 3).

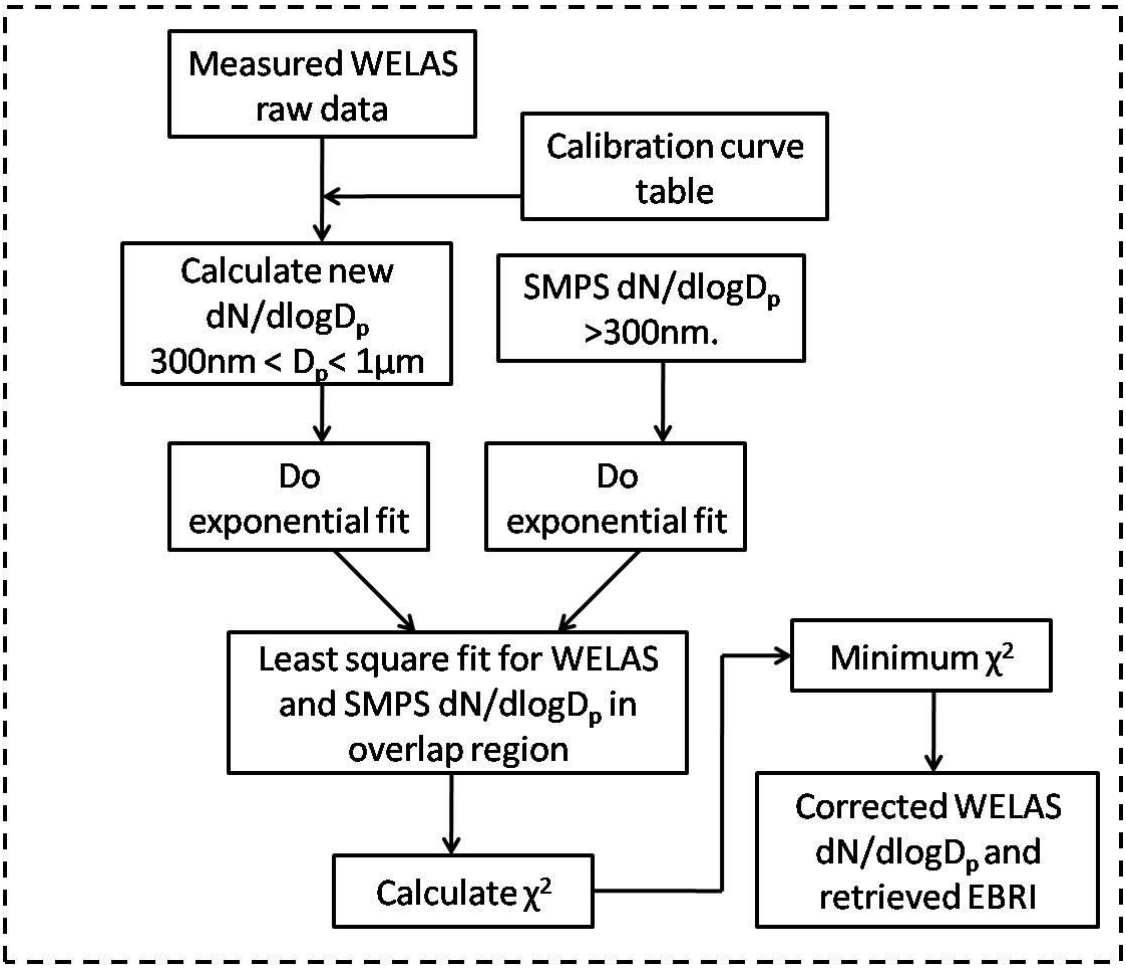

Figure 3.5 Schematic of the algorithm's logic for deriving the effective broadband refractive index (EBRI) using the generated calibration curves to match the measured size distribution by the WELAS to that of an SMPS.

At the first period in Figure 3.6 (period 1), which is dominated by flaming, the $m_{broad,eff}$ is highly variable. It varies from a minimum value of 1.47 to a maximum of 1.59 for the real part of the RI, and from a minimum value of 0.03 to a maximum value of 0.11 for the imaginary part. This variability can be attributed to a mixed aerosol population, one from the open fires and the other from the ambient pollution aerosols. Yamasoe et al. (1998)[132], based on sun photometer retrievals, reported a real part of the refractive index ranging between 1.5 and 1.6 for wavelengths of 438, 670, 870, and 1020nm occurring mainly in flaming conditions. During the extensive smoldering smoke event (period 2), the $m_{broad,eff}$ is stable with an average of m=1.54(±0.01)+i0.04(±0.01). Wandinger *et al.* (2002)[133] reported complex refractive indices ranging from 1.56 to 1.66 for the real part and 0.05 to 0.07 for the imaginary part at wavelengths between 320 and 1064 nm, for measurements upwind of forest fires in Northern Canada (at low RH conditions). The aerosols in our case were measured without drying. The relative humidity at the site of the campaign during the burning event reached a maximum value of 85%. Nonetheless, Hand *et al.* (2010)[134] observed no significant changes in the scattering coefficient of fresh smoke at RH lower than 80%. Our

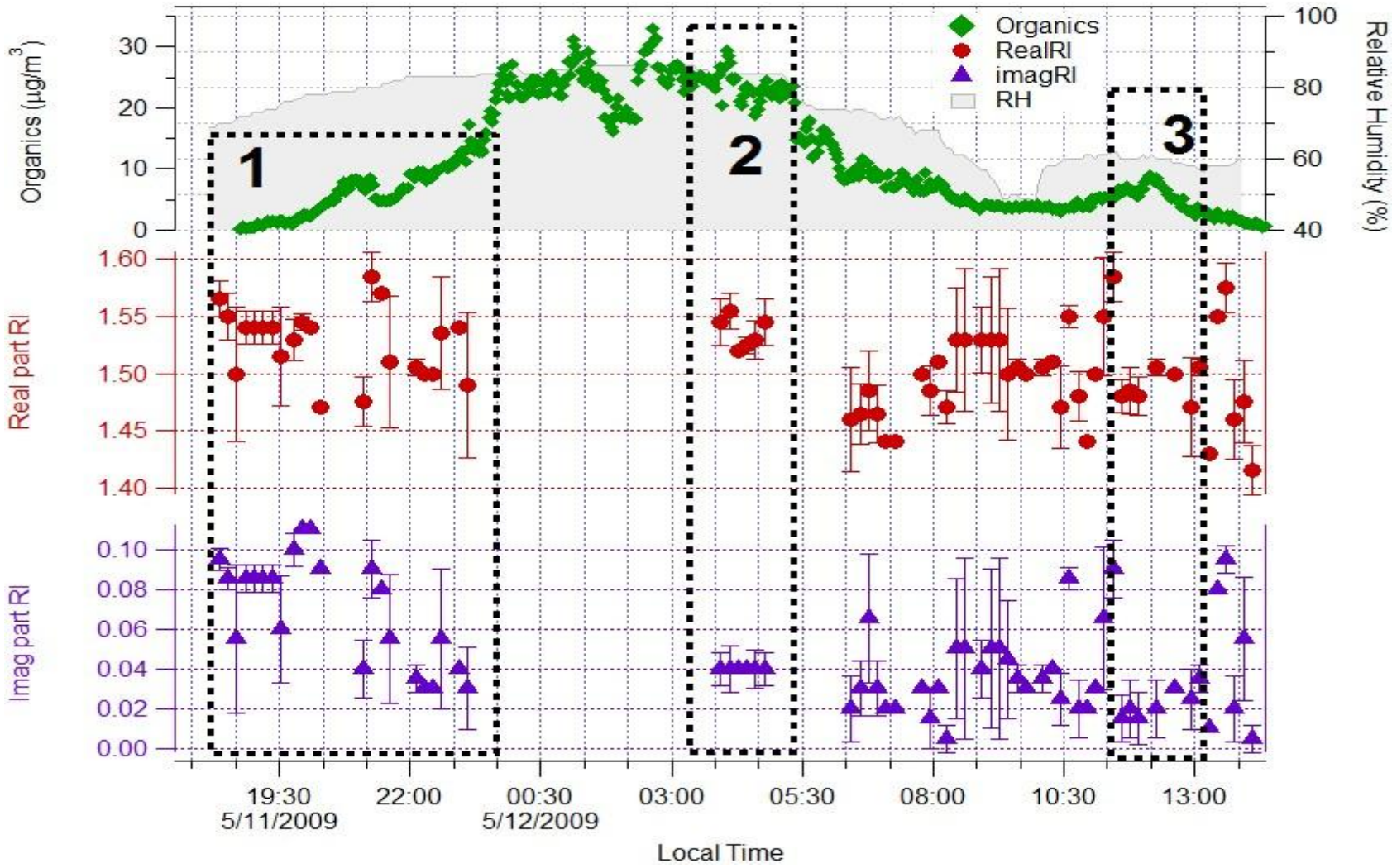

Figure 3.6 Time series of the Real and imaginary components of the effective broadband refractive index. The total organic mass is plotted to serve as a reference point. The burning event began at around 18:00 h local time. Period 1 is mostly open fires, Period 2 is the smoldering phase, and Period 3 is during the peak of photochemical processing on the following day.

results are slightly lower (for both the real and imaginary part) than those reported by Wandinger *et al.* (2002)[133], suggesting some water uptake by the BB aerosol, but the difference can also be attributed to a different mixture of the fuel, and to the occurrence of other ambient aerosols. On the other hand, the retrieved $m_{broad,eff}$ is higher than the average RI for biomass burning aerosol in high relative humidity conditions, as measured in the Amazon, with an average RI of m=1.41+i0.013 at 545nm.[135] The day following the fires, in which the RH decreases to 50–60%, there's a clear downward trend in the imaginary part of the $m_{broad,eff}$. Also, the real part of the $m_{broad,eff}$ is lower than the values measured during the burning event, but with more variations. The change in the real part can result from the presence of a mixed population of aerosols, traces of water on the particles due to more hydrophilic aerosols or aging. Previous studies in Southern Africa have shown that the single scattering albedo increases with the aging process of the aerosol, which includes changes in the aerosol chemical composition and shape.[136, 137] The aged biomass burning aerosols are less absorbing than the freshly emitted aerosols. In this study, during noon the day after the burning event (part 3), the average $m_{broad,eff}$ retrieved is m=1.49(±0.01)+i0.02(±0.01). Johnson *et al*. (2008)[138] derived a complex refractive index for aged biomass burning aerosol of m=1.54+i0.045, and Haywood *et al.* (2003)[136] reported a value of m=1.54+i0.018 at 550 nm. The values obtained in this study for the real part of the RI are slightly lower and the imaginary part falls between the values presented in the two studies. However, Johnson *et al*. (2008)[138] results were influenced by the presence of dust, and Haywood *et al*. (2003)[136] performed most of their measurements over the Atlantic Ocean. Moreover, the $m_{broad,eff}$ can be also influenced by traffic aerosols, as our measurements took place in an urban area.

3.9 Conclusions

A simple approach to retrieve the effective broadband refractive index in the visible range by matching the optical diameters measured by a white light OPC with the mobility diameters of a DMA was developed. This is the first time, to my knowledge, that such a method was applied to obtain RIs of lightly absorbing (SRFA and the AS:nigrosine 10:1 mixture) and highly absorbing substances (nigrosine and its various mixtures with AS and GA).

Generally, the real part of the $m_{broad,eff}$ for all substances in this study was retrieved successfully with a difference less than 8% from literature values. For absorbing substances, with the exception of AS:N 2:1 ratio, the obtained imaginary part is in good agreement with the expected values, and well within the measurement of other instruments, such as continuous wave and pulsed CRD spectroscopy.

With this new approach, the OPC can be used (with the caveat of the counting efficiency) to measure and analyze data and retrieve the complex $m_{broad,eff}$ for substances with a wide range of optical properties; from pure scatterers, for which the retrieval method is most accurate, up to highly absorbing ones, such as nigrosine. I expect that for substances

with greater imaginary parts than nigrosine, such as soot, the RI retrieval will be less accurate. Using this approach, it is easy to obtain accurate calibration curves for data analysis and correct the measured sizes of white light OPCs to agree with the mobility diameters, i.e. applying the retrieved calibration curve provides a corrected size distribution. This approach can substantially improve aerosol size distributions measured by OPCs in field measurements.

Finally, the calibration curves generated by this method were used to modify measured optical size distributions and align them with those of an SMPS to measure biomass burning aerosols, and by doing so, the effective broadband refractive index was derived. The average $m_{broad,eff}$ for a mixed population of aerosols dominated by open fires was $m_{broad,eff}=1.53(\pm0.03)+0.07i(\pm0.03)$, during the smoldering phase of the fires the effective broadband refractive index was found to be $m_{broad,eff}=1.54(\pm0.01)+0.04i(\pm0.01)$, compared to $m_{broad,eff}=1.49(\pm0.01)+0.02i(\pm0.01)$ of the aged aerosols measured the day following the burning event. As a caveat it should be emphasized that the method was applied for non-spherical particles, especially since the RH was below 80% during most of the measurements.

4 Interaction of absorbing aerosols with high relative humidity, is the volume weighted mixing rule valid?

4.1 Introduction

There is a complex interaction between clouds, aerosols and radiation which is still not well understood.[6] Koren *et al.*(2007)[36] showed there is a belt of forming and evaporating cloud fragments and hydrated aerosols extending kilometers away from the clouds into cloud-free areas. This phenomenon has been termed the "twilight zone". In the twilight zone, high relative humidity (RH) is predominant, creating an environment where aerosols can take up water and eventually deliquesce; once the aerosols deliquesce they become larger and more optically active. Moreover, modeling of downwelling solar irradiance at the surface relies on parameterizations of aerosol optical properties, mostly the single scattering albedo (ω) and the asymmetry parameter (g), and this is a major source of uncertainty.[139] Furthering our understanding of the optical properties of the hydrated aerosols can enable us to better model areas such as the twilight zone (as well as cloud-free areas with high RH), decrease uncertainties and better predict future climate.

Some laboratory studies have been devoted to understand the optical properties of purely scattering aerosols (mostly because of their "cooling effect") when exposed to high relative humidity. Garland *et al.*(2007)[140] parameterized the relative humidity dependence of light extinction at 532 nm for inorganic ammonium sulfate aerosols; while Baynard *et al.*(2006)[141] focused on mixtures of NaCl and ammonium sulfate with a few dicarboxylic acids. Recently, Hasenkopf *et al.* (2011)[142] compared the optical growth at 532 nm of slightly absorbing organic particles likely to have been present on early Earth and Titan. Absorbing aerosols can heat the atmosphere and affect atmospheric circulation[105] and cloud formation[97]; hence, it is crucial to better understand their optical properties and their RH dependence. While several studies have been directed to investigate the properties of absorbing aerosols such as organics[143], dust[100, 144], and soot[97, 106, 107, 145], our level of understanding as the RH changes is still limited.

At different RH values, water uptake by atmospheric aerosols can occur; hence, changing their size and composition. This in turn will change the complex refractive index of the aerosols. To accurately predict the "new" complex RI different theoretical mixing rules are often used.[92] The most common rule being the volume weighted mixing rule. The volume weighted mixing rule is often used in chemical transport models that estimate the aerosol direct forcing, [146, 147] and in some laboratory studies. Riziq *et al*. (2007)[71] measured different organic mixtures to test the validity of this mixing rule for a solution (before atomizing the particles). Garland *et al*. (2007)[140] used the volume weighted mixing rule (assuming complete mixing of the aerosols as they passed through a humidification stage) to test the performance of their system in parameterizing the change in the extinction coefficient for purely scattering substances (inorganic and organics) at an RH of 80%.

To explore the validity of the mixing rules for water soluble absorbing aerosols, this study addresses the change in refractive index of absorbing aerosols when exposed to 80% and 90% relative humidities, at 355 nm and 532 nm wavelengths. This study attempts at reaching closure between measured hygroscopic growth factors (GF; by tandem hygroscopic DMA measurements), measured optical extinction (by CRD) and model calculations in order to study the ability of the model to predict the optical properties of hydrated aerosols with different degrees of absorption. Moreover, how the ratio of the extinction coefficient of the humidified aerosols to the dry extinction coefficient changes as a function of size is investigated. Furthermore, a core-shell structure model is also used to explore the differences between the models, for substances with low growth factors, under these hydration conditions. Finally, these laboratory measurements will be used as a basis to investigate how the twilight zone of warm clouds would change if aerosols with different degrees of absorption, from purely scattering to highly absorbing, are present.

4.2 Methodology

To study the RH dependence of aerosols' optical extinction and absorption at 532 nm, a cavity ring down (CRD), a photoacoustic sensor (PAS), and a scanning mobility particle sizer (SMPS; TSI model 3081) were used. A schematic of the laboratory setup is shown in Figure 4.1. The same setup was used for the 355nm measurements, except that the PAS was bypassed.

Quasi-monodisperse particle distributions were generated using the particle generation system described in Appendix I. The dry, size selected aerosols exiting the DMA of the particle generation system were diluted and directed to a deliquescence stage consisting of a saturated permeable membrane at a controlled temperature (labeled 'Humidifier' in Figure 4.1) before being sampled by the CRD-PAS-SMPS system. Aerosol losses were measured with different sizes of polystyrene latex spheres (up to 800 nm) by placing a condensation particle counter (CPC; TSI Model 3022) before the CRD, and comparing the particle number concentration of this CPC with another CPC located at the end of the system; differences in particle concentration of less than 2% were found. To avoid temperature fluctuations in the system, insulation was placed around the tubing and the CRD, PAS, and SMPS (represented by the shaded areas in Figure 4.1). The relative humidity and temperature were measured inside the CRD, at the exit of the PAS, and at the entrance of the sheath flow of the DMA in the SMPS system. Measurements were only taken when all measured RH values in the system were within 2% (RH meter manufacturer's uncertainties are ±3%RH for $10 \leq \%RH \leq 90$). Following the deliquescence stage the aerosols' RH dependent extinction coefficient ($\alpha_{ext,\ \%RH}$) was measured with the CRD, then the absorption coefficient ($\alpha_{abs,\ \%RH}$) was measured by the PAS, and finally the hygroscopic growth factor (GF) was measured with the SMPS. The aerosol number concentrations were also measured with a CPC at the outlet of the PAS.

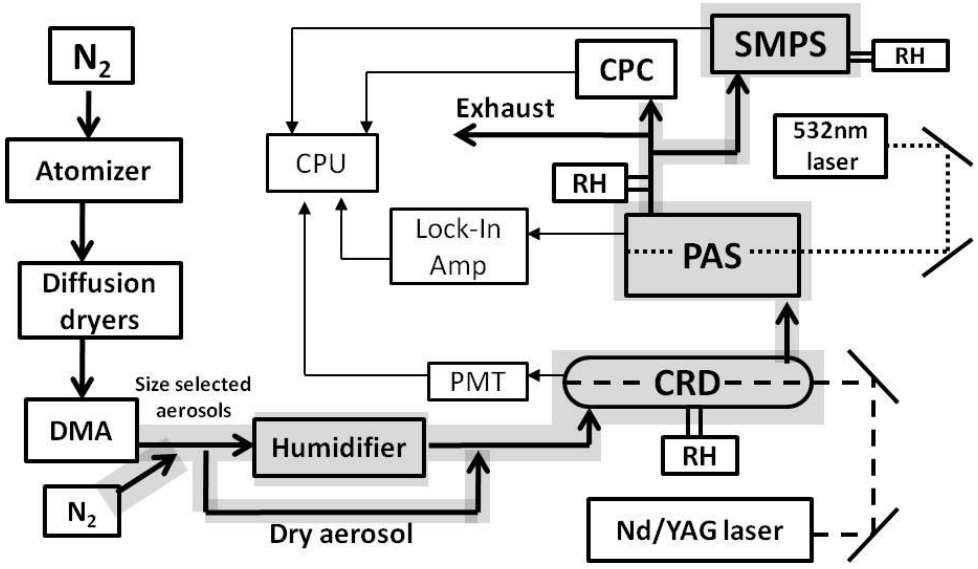

Figure 4.1. Schematic of the laboratory setup. The bold arrows show the aerosol flow and the dashed lines represent the lasers light paths. The temperature and relative humidity meters are marked as 'RH'. Abbreviations: CPC, condensation particle counter; PMT, photomultiplier; Lock-In Amp, Lock-In Amplifier; DMA, differential mobility analyzer.

The substances were measured at eight different mobility diameters, from 200 nm to 550 nm in 50 nm steps, and 2 different RH values; 80% and 90%. The sequence of measurements was performed by first measuring the substance at different diameters under dry conditions (RH < 3%), then directing the sample flow through the humidifier, allowing the system to equilibrate at the desired RH, and repeating the measurement for the same diameters. After the hydrated experiments were completed, the dry measurement was repeated to check the stability of the system, if the final dry measurement differed by more than 5% from the initial one, the measurements for the substance were repeated.

The hygroscopic growth factor is defined as the relative increase in the mobility diameter of particles due to water uptake at a specific %RH, as given by equation 4.2:

$$GF(\%RH, Dry) = \frac{D_{\%RH}(RH)}{D_{dry}} \tag{4.2}$$

where $D_{\%RH}(RH)$ is the mobility diameter at a specific %RH, and D_{dry} is the dry measured mobility diameter. The GF of a mixture (GF_{mix}) can be estimated from the GFs of the pure components and their respective volume fractions (ε) using the Zdanovskii–Stokes–Robinson relation (ZSR relation)[148, 149]:

$$GF_{mix} = \left(\sum_j \varepsilon_j GF_j^3 \right)^{\frac{1}{3}} \tag{4.3}$$

where the subscript *j* represents the different substances. The model assumes spherical particles, ideal mixing (i.e. no volume change upon mixing) and independent water uptake of the organic and inorganic components. Figure 4.2 shows an example of measured size distributions of 200 nm nigrosine seed particles before and after being exposed to 80% RH.

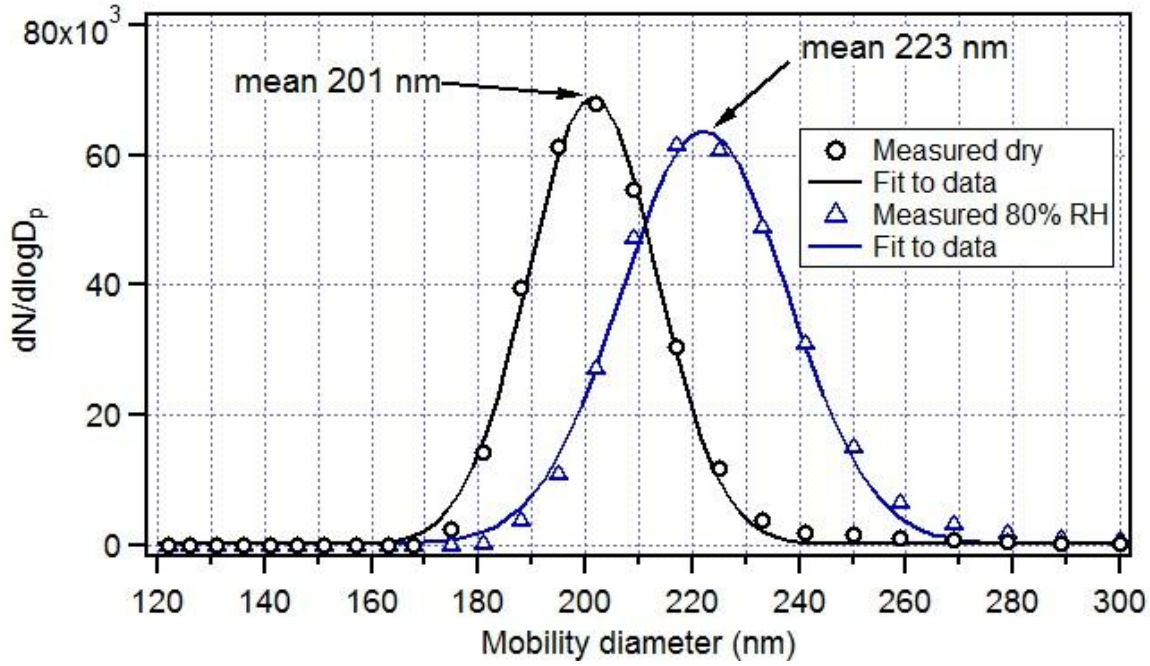

Figure 4.2. Measured size distributions for 200 nm particles of dry nigrosine (black circles), and nigrosine exposed to 80% RH (blue triangles). The solid lines are Gaussian fits to the measured data.

The changes of the aerosols' optical properties due to hygroscopic growth, $f\mathrm{RH}_{ext}$(%RH,Dry), is represented by the ratio of the measured extinction coefficient (α_{ext}, Mm^{-1}) at a specific %RH to the dry measurement, expressed as:

$$fRH_{ext}(\%RH, Dry) = \frac{\alpha_{ext}(\%RH)}{\alpha_{ext}(Dry)} \tag{4.4}$$

where $\alpha_{ext}(\%RH)$ is the extinction coefficient at a specific RH, and $\alpha_{ext}(Dry)$ is the extinction coefficient of the dry aerosol, measured at an RH<3%. The extinction coefficient for homogenous spheres is described by:

$$\alpha_{ext} = \frac{1}{4}\pi N D^2 Q_{ext} \tag{4.5}$$

where N is the particle concentration, D the particle's diameter, and Q_{ext} is the extinction efficiency. Hence, inserting equation 4.2 and 4.5 into equation 4.4, $f\mathrm{RH}_{ext}$(%RH,Dry)can be expressed as:

$$fRH_{ext}(\%RH, Dry) = \frac{N_{\%RH} Q_{ext-\%RH}}{N_{Dry} Q_{ext-dry}} GF^2 \quad (4.6)$$

where N_i is the particle concentration, $Q_{ext\text{-}\%RH}$ is the extinction efficiency at a specific relative humidity, and $Q_{exr\text{-}dry}$ is the extinction efficiency of the dry substance.

Particle concentrations were kept below 1000 cm^{-3}, and the median diameter from the SMPS size distributions (D_{med}) was taken instead of the chosen mobility diameter from the first DMA in order to reduce biases arising from multiply-charged particles.[150]. For this, a solution concentration of 500mg L^{-1} for sizes between 200nm to 300nm was used, and for larger diameters, 350nm to 550nm, a 1000mg L^{-1} concentration solution was used.

Three different substances were used to measure the extinction and absorption fRH$_{ext}$(%RH,Dry) and fRH$_{abs}$(%RH,Dry) dependence on particle size and absorption: ammonium sulfate (AS), a purely scattering substance, which was used to check the system performance; nigrosine, an organic black dye used as a model for highly absorbing substances; and IHSS Pahokee Peat (Pahokee), a fulvic acid used as a model for humic-like substances, complex organic matter often found in aerosol.[151] A mixture of ammonium sulfate and nigrosine 1:1 molar ratio (AS:Nig), was also measured to investigate the effect of the variation in the imaginary part of the complex refractive index on the results.

4.3 System validation with ammonium sulfate

The measurements of fRH$_{ext}$(%RH,Dry) with the system described above were validated with ammonium sulfate at 80% RH. Figure 4.3 shows the measured fRH$_{ext}$(80%RH,Dry) in this study, compared to that reported by Garland *et al*. (2007)[140] and to the calculated fRH$_{ext}$(80%RH,Dry) based on the measured GFs from the SMPS. To convert the GFs to fRH$_{ext}$(RH, dry), the method used by Garland *et al*. (2007)[140] was applied. Briefly, by using Mie scattering calculations,[37] the extinction cross sections of the dry aerosols were calculated using the refractive indices retrieved from the dry CRD measurements of AS, shown in Figure 4.4 as the red line. Humidity-controlled, tandem SMPS measurements were used to determine the hygroscopic GF of size-selected aerosols and consequently to determine the complex refractive index of the humidified aerosols using the volume weighted mixing rule, given as:

$$n_{mix} = V_{Dry}^{frac} n_{Dry} + V_{water}^{frac} n_{water} \quad (4.7.1)$$

$$k_{mix} = V_{Dry}^{frac} k_{Dry} + V_{water}^{frac} k_{water} \quad (4.7.2)$$

where V_i^{frac} is the volume fraction of each component, which can be rewritten as a function of the GF by inserting equation 4.2 into equations 4.7.1 and 4.7.2,

$$n_{mix} = \frac{D_{dry}^3 n_{Dry} + D_{water}^3 n_{water}}{D_{Dry}^3 + D_{water}^3} = \frac{1}{GF^3}\left[n_{Dry} + (GF^3 - 1)n_{water}\right] \quad (4.8.1)$$

$$k_{mix} = \frac{D_{dry}^3 k_{Dry} + D_{water}^3 k_{water}}{D_{Dry}^3 + D_{water}^3} = \frac{1}{GF^3}\left[k_{Dry} + (GF^3 - 1)k_{water}\right] \quad (4.8.2)$$

Hence, to determine the extinction cross-section at 532 nm of AS humidified at 80% RH (dotted line in Figure 4.3) the optical properties of pure AS and water, and the measured GF were used. The complex refractive index of AS humidified at 80% RH was calculated to be m_{mix}=1.390+i0.0; the refractive index for AS used was m=1.504 + i0.0 (derived from the

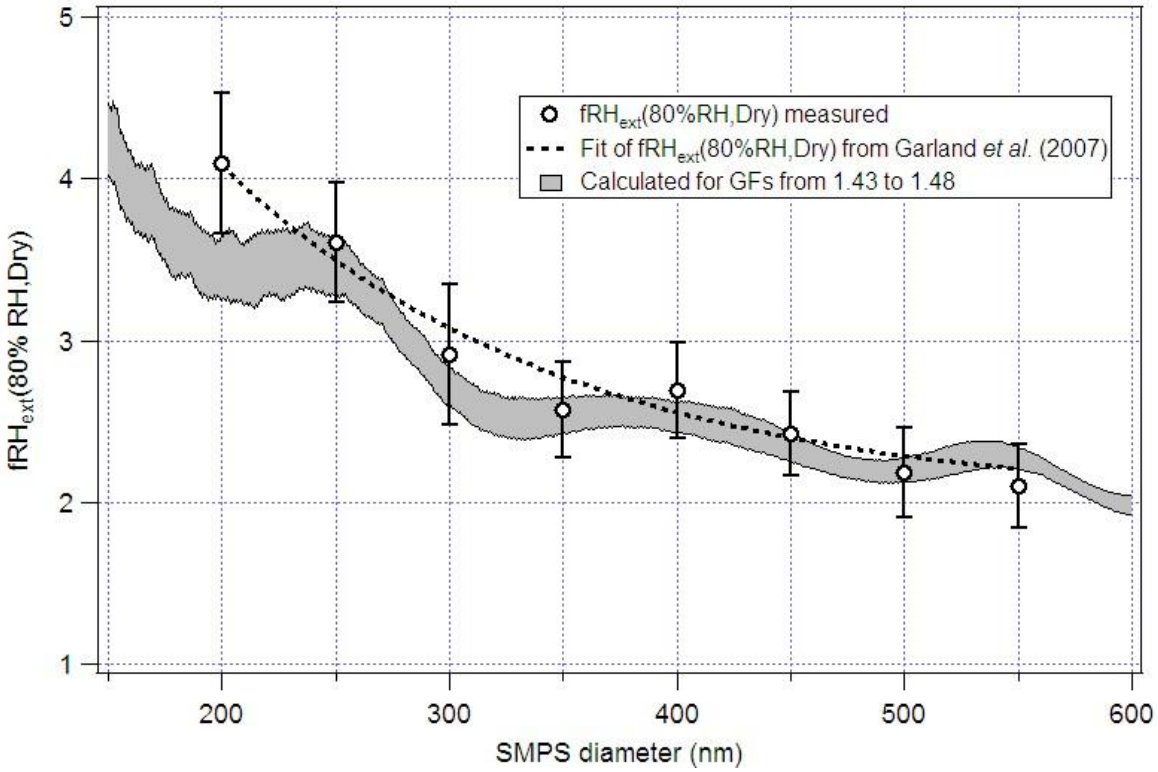

Figure 4.3. Measured fRH$_{ext}$(80% RH,Dry) as a function of size (solid circles) for pure ammonium sulfate. The dashed line shows the exponential fit from the measurements performed by Garland *et al*. (2007)[140] for ammonium sulfate at the same RH. The shaded area is the calculated fRH$_{ext}$(80% RH, Dry) range, based on the growth factors measured with the SMPS.

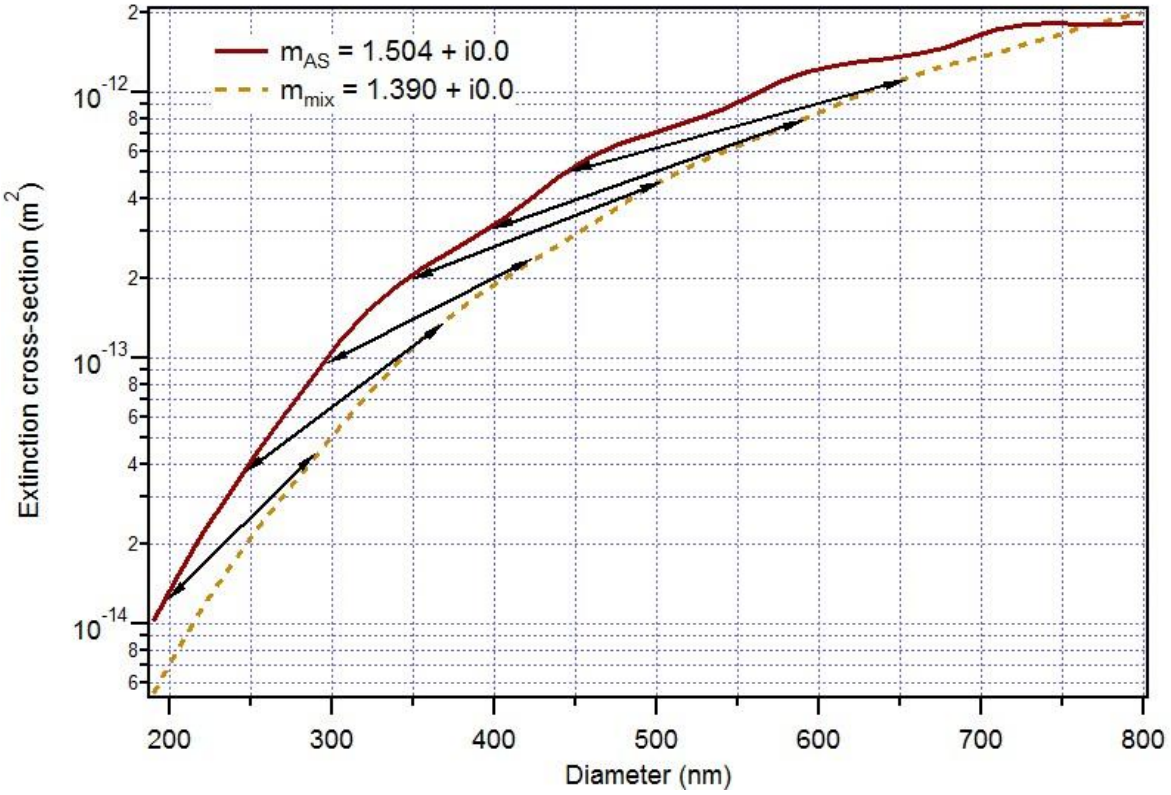

Figure 4.4. Extinction cross-sections as a function of size for dry ammonium sulfate (red line), and for ammonium sulfate humidified at 80% RH.

dry measurements), an RI of m=1.335 + i0.0[152] was used for water at 532 nm, and a measured GF(80%RH,Dry) = 1.45(±0.02) was used.

Finally, the diameters, $D_{\%RH} = GF \times D_{dry}$, and the corresponding humidified extinction cross section values at a wavelength of 532 nm can be used to determine the ratio of the humidified extinction cross section curve to the dry AS curve; i.e. the theoretical $f\mathrm{RH}_{ext}$(80%RH,Dry). The black arrows in Figure 4.4 show the increase in size and extinction cross section from their dry values to their corresponding hydrated values, used for the calculation of the theoretical fRH(80%RH,Dry); for example, a 200 nm AS particle has a dry extinction cross-section of 1.18×10^{-14} m^2, after humidification it grew to a 290 nm diameter with an extinction cross-section of 4.14×10^{-14} m^2, which gives an fRH(80%RH,Dry) = 3.51. All of the calculated values for the theoretical fRH(80%RH,Dry) are shown as the shaded area in Figure 4.3. The extent of the shaded area is determined from the standard deviation of the measured GFs. The reported uncertainties in the measured $f\mathrm{RH}_{ext}$(RH, dry) were based on the uncertainty in the RH measurement (±3% RH), the SMPS size distributions (~±10%), and the uncertainty in the measured extinction coefficient from the CRD (±1%).

It can be seen in Figure 4.3 that the measured $f\mathrm{RH}_{ext}$(80% RH, Dry) values (every measured value is an average of at least 2 min of measurements with an extinction value obtained every 10.1 seconds) are in very good agreement with the $f\mathrm{RH}_{ext}$(80% RH, Dry) measured by Garland *et al*. (2007)[140], and with the theoretical calculations. There is a slight

overestimation at 200nm, which may be attributed to the presence of doubly charged particles from the initial size selection. The good agreement between the theoretical calculations and the measured values provides a validation of the experimental setup.

4.4 Photoacoustic sensor measurements

In order to obtain a measure of $f\mathrm{RH}_{abs}$(%RH,Dry) and the Q_{abs} values at a high relative humidity (RH≥80%), mass transfer effects caused by evaporation, condensation and transport need to be taken into account. For example, a 'false' photoacoustic signal was generated when the relative humidity was increased in the system. Absorption by water vapor at 532nm was discarded as an explanation since the empty decay time for the CRD did not change in wet measurements (either 80% or 90% RH). To address this phenomenon I measured the photoacoustic signal with a particle free system at the desired RH, and established a new zero. However, it was not possible to extract the absorption signal at 80% and 90% RH since the noise levels were higher than the signal itself. Figure 4.5 shows an example of the obtained signal at 80% RH with no aerosols and after 500nm nigrosine aerosols were inserted. Arnott *et al.* (2003)[153] also found that at ambient measurements at high RH conditions there is a contribution from mass transfer to the photoacoustic signal, and recommended that PAS measurements should be done below 65% RH. From this study I can also conclude, that even in laboratory setups the PAS cannot be used at high RHs.

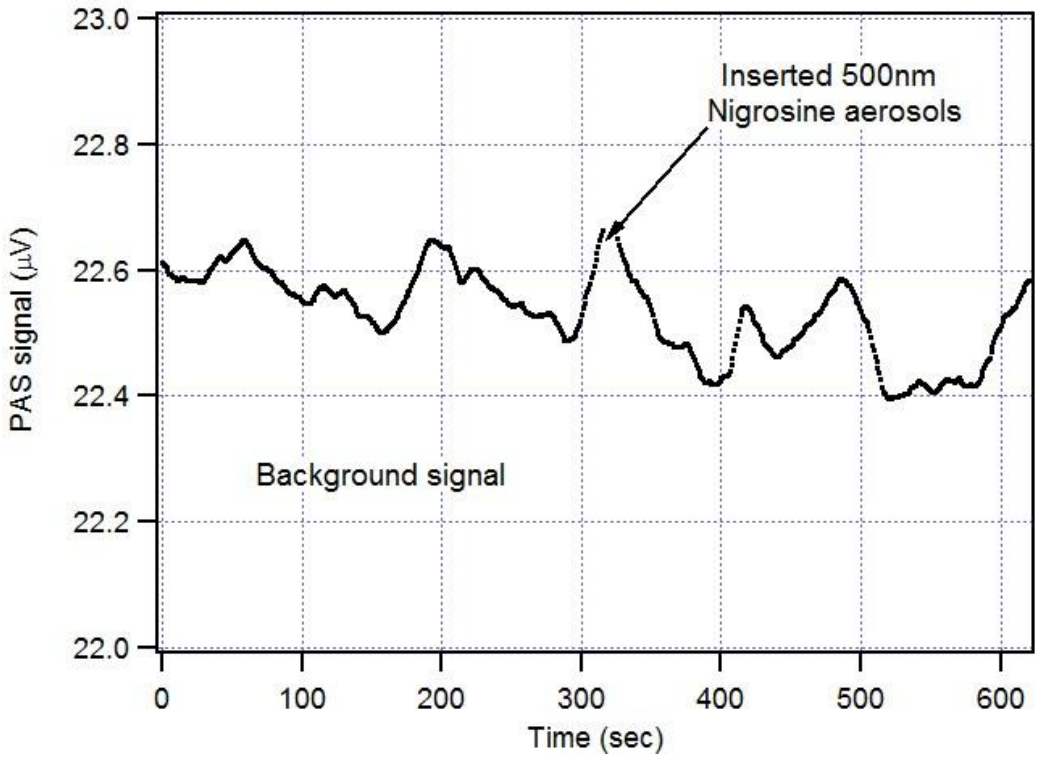

Figure 4.5. Signal from the PAS at 80% RH with no aerosol and after 500nm nigrosine aerosols were inserted.

4.5 Optical growth of humidified absorbing aerosols

The size dependence of $f\mathrm{RH}_{ext}$ at 80% and 90% RH was studied for substances with different degrees of absorption at 532 nm and 355 nm. The GF values were converted to theoretical $f\mathrm{RH}_{ext}$(%RH, Dry) as described for the 532 nm AS measurement at 80% RH. Figure 4.6 shows the size dependence of $f\mathrm{RH}_{ext}$(80%RH, Dry) and $f\mathrm{RH}_{ext}$(90%RH, Dry) for pure AS, IHSS Pahokee Peat, a mixture of AS and nigrosine at a 1:1 molar ratio, and pure nigrosine dye for 80% (left) and 90% (right) RH at 532 nm (green full markers and patterned shaded area) and 355 nm (blue open markers and full shaded area). The measured growth factors obtained with the SMPS for each substance are presented in the legend. The reported ranges for the converted values (shaded areas in Figure 4.6) are based on the values calculated from the lower and upper limits of the uncertainty of the measured GFs.

The measurements for all substances at both RHs and wavelengths are in excellent agreement with the calculations; while there are some values which are outside of the shaded area all substances follow the theoretical trends. The measurement for the Pahokee peat for 355 nm at 90% RH could not be completed due to shortage of the substance, the measurement presented was performed at an RH = 95% (±3%).

The ammonium sulfate measurements at both RHs show an exponential behavior of $f\mathrm{RH}_{ext}$(80%RH,Dry) and $f\mathrm{RH}_{ext}$(90%RH,Dry) with size. Garland *et al.* (2007)[140] parameterized the behavior of AS at 80% RH with an exponential function (see Figure 4.3 dashed line). This study shows that the exponential behavior is also maintained at 90% RH for 355 nm and 532 nm, as can be seen in Figure 4.6. Additionally, the $f\mathrm{RH}_{ext}$(80%RH,Dry) and $f\mathrm{RH}_{ext}$(90%RH,Dry) values at 532 nm are greater than at 355 nm. The spectral independence of AS on wavelength might incorrectly lead to expect the same $f\mathrm{RH}_{ext}$(%RH,Dry) curve for both wavelengths, however, the differences are attributed to the shape of the Mie curves and to the fact that the size parameters ($x = \pi D/\lambda$) for the diameters measured are larger at 355 nm than at 532 nm. Figure 4.7 shows the AS measurements of $f\mathrm{RH}_{ext}$(80%RH,Dry) as a function of size parameter to demonstrate this. For purely scattering substances, the extinction efficiency increases rapidly for size parameters smaller than 3, and the slope of this increase is steeper as the real part of the RI is larger. At 355 nm, the initial dry diameters measured have a greater extinction efficiency than at 532 nm, making $f\mathrm{RH}_{ext}$(%RH,Dry) smaller at 355 nm than at 532 nm.

Equation 4.6 for $f\mathrm{RH}_{ext}$(%RH,Dry) indicates that deviations from a constant value of $f\mathrm{RH}_{ext}$(%RH,Dry) arise from the $Q_{ext-\%RH} \,/\, Q_{ext-Dry}$ term. Beaver *et al.* (2008)[154] and Garland *et al.* (2007)[140] found a decreasing exponential behavior of $f\mathrm{RH}_{ext}$(80%RH,Dry) with size, with the maximum value of $f\mathrm{RH}_{ext}$(80%RH,Dry) at the smallest size measured in measurements of purely scattering organic substances. This exponential behavior clearly shows the behavior of the $Q_{ext-\%RH} \,/\, Q_{ext-Dry}$. However, the $Q_{ext-\%RH} \,/\, Q_{ext-Dry}$ term can also induce $f\mathrm{RH}_{ext}$(%RH,Dry) to be reduced in the smaller sizes. Form Figure 4.6, we

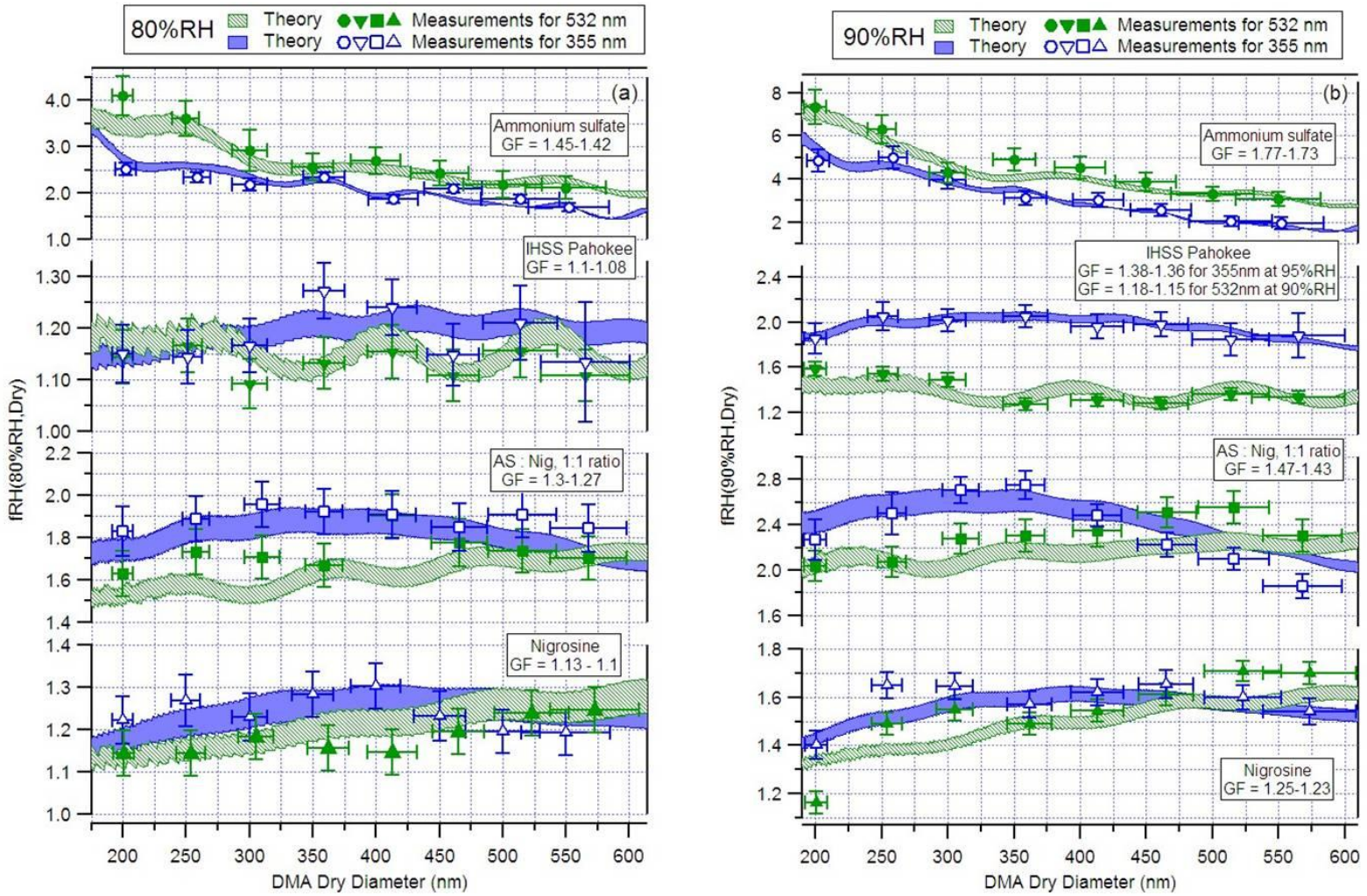

Figure 4.6 Size dependence of (a) $f\mathrm{RH}_{ext}$(80%RH,Dry) and (b) $f\mathrm{RH}_{ext}$(90%RH,Dry) for pure ammonium sulfate (circles), IHSS Pahokee peat (inverted triangles), the mixture of ammonium sulfate and nigrosine at 1 : 1 molar ratio (squares), and pure nigrosine (triangles) at 532 nm (full green markers) and 355 nm (open blue markers). The shaded areas represent the theoretical size dependence calculated from the measured growth factors from the SMPS; the growth factors measured are written in the legend with each substance.

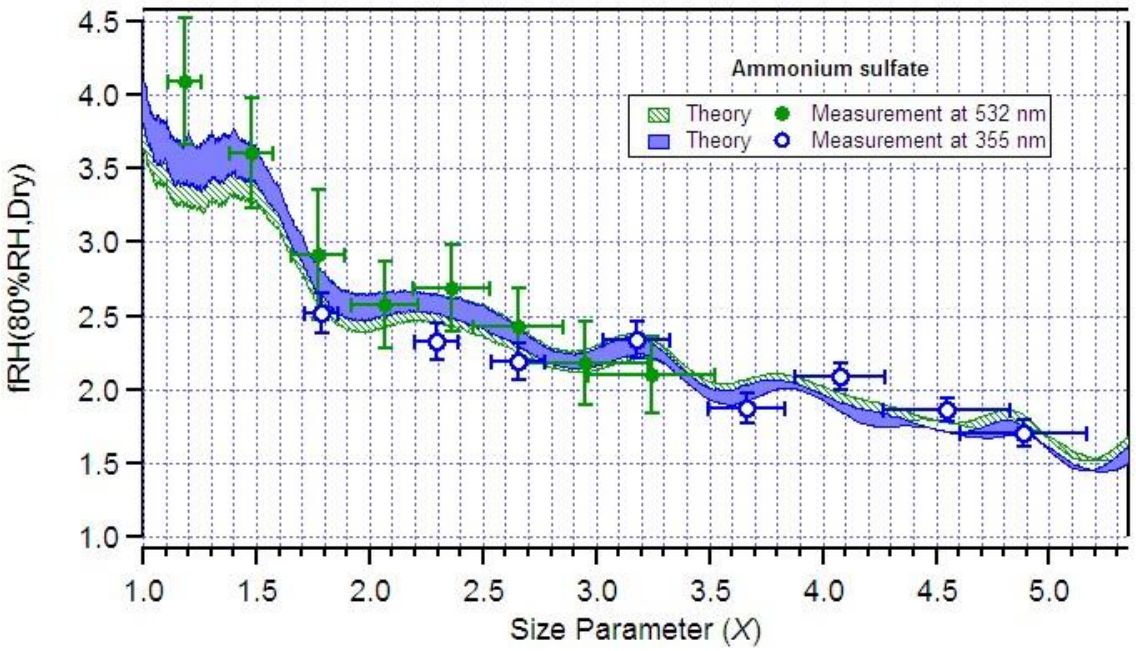

Figure 4.7. fRH$_{ext}$(80%RH,Dry) as a function of size parameter for ammonium sulfate at 532 nm (solid green circles) and 355 nm (open blue circles). The theoretical fRH$_{ext}$(80%RH,Dry) is shown as the shaded areas.

can see none of the substances with an imaginary part greater than zero showing this exponential dependence. However, it is difficult to quantify the role of the complex refractive index, and in particular the imaginary part in assessing the dependence of fRH$_{ext}$(%RH,Dry) with size. However, by comparing substances with similar GFs, the effect of the $Q_{ext-\%RH}$ / $Q_{ext-Dry}$ term and more specifically the imaginary part of the RI, on fRH$_{ext}$ can be explored. Figure 4.6 shows that fRH$_{ext}$(80%RH,Dry) for AS has a similar GF to fRH$_{ext}$(90%RH,Dry) for AS:Nig. To evaluate the effect of RI with a non-zero imaginary part on the dependence of fRH$_{ext}$ with size, both substances at 532 nm and 355 nm are plotted together in Figure 4.8a and Figure 4.8b, respectively. The ratio of fRH$_{ext}$(90%RH,Dry) of AS:Nig to fRH$_{ext}$(80%RH,Dry) of AS was calculated and plotted in Figure 4.8c for 532nm and in Figure 4.8d for 355 nm. The theoretical ratios for fRH$_{ext}$ at both wavelengths and RHs are presented. These two measurements show that absorbing substances change the exponential dependence of fRH$_{ext}$ with size seen in purely scattering substances. From the ratio at 532 nm of fRH(90%RH,Dry) of AS:Nig, the absorbing substance, to fRH$_{ext}$(80%RH,Dry) of AS, the purely scattering substance, there is a decrease in the optical growth of up 50% for particles smaller than 450 nm. At 355 nm there is an increase in the optical growth of up 33%. We can see that the effect of the absorption is enhanced in large particles, this is a result of the fact that the absorption scales with the volume while the scattering depends on the surface area.

For a better understanding of the effect of absorption on the magnitude and dependence of fRH$_{ext}$ on size, more substances with a wide variety of imaginary parts need to be studied. Using mixtures of purely scattering organic substances with nigrosine or other proxies for absorbing substances can shed some light on the issue. Nevertheless, the

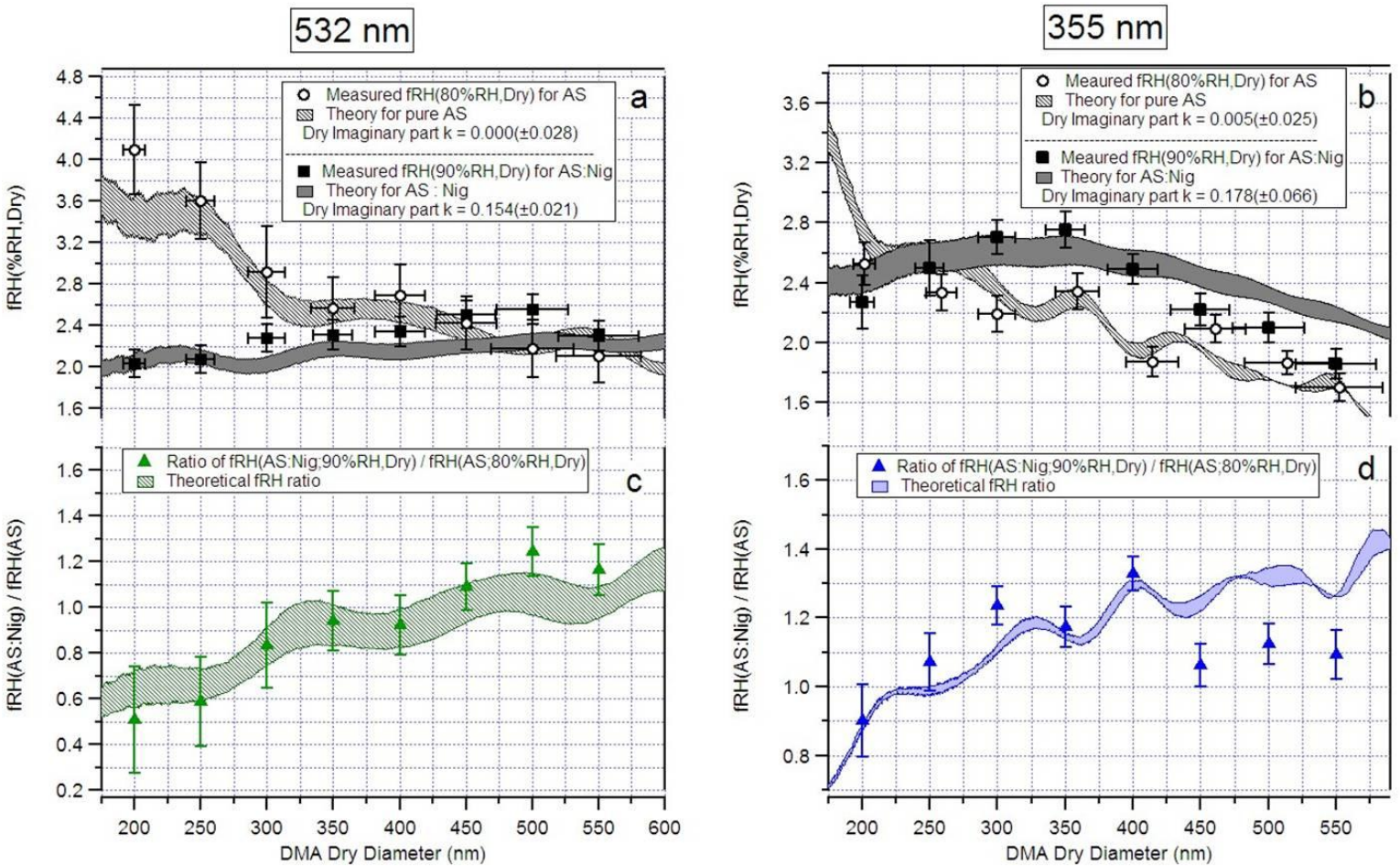

Figure 4.8 *f*RH(%RH,Dry) vs. DMA dry diameter for AS at 80%RH (open circles) and AS:Nig at 90%RH (filled squares) at 532nm(a) and 355nm(b). The theoretical calculations for both substances are also shown for comparison; light grey for AS, and dark grey for AS:Nig. The dry imaginary part of the complex refractive index for both substances is presented in the legend. The ratio of *f*RH(90%RH,Dry) of AS:Nig to *f*RH(80%RH,Dry) of AS is presented in the lower panels at 532nm (c) and 355nm (d). The theoretical ratio for both wavelengths is also presented; light patterned green for 532 nm and light solid blue for 355nm.

measurements presented here demonstrate that a non-zero imaginary part can have a significant influence on the dependence of $f\mathrm{RH}_{ext}$ on size.

4.6 Validation of the volume weighted optical mixing rule

Figure 4.6 shows a qualitative agreement between measurements and theoretical calculations assuming homogenous mixing and using the volume weighted mixing rule to calculate the corresponding complex refractive index. A quantitative analysis was done by comparing the RI values obtained from the measurements with various Mie models that assume different mixing states or structures. These calculations may serve as a further verification for the commonly used assumption of homogenously mixed particles at high %RH values. To retrieve the RI from the CRD measurements, the extinction efficiency of the humidified aerosols ($Q_{ext\text{-}\%RH}$) was calculated from the measured GF and the extinction coefficient at every diameter. By knowing the value of Q_{ext} at different diameters for internally mixed aerosols, a refractive index can be retrieved.[66, 72] Figure 4.9 shows an example of one result of the complex RI derivation and comparison performed. Three sets of data of Q_{ext} versus size at 532 nm and 80% RH for the IHSS Pahokee Peat aerosol are presented: 1) The measured $Q_{ext,80\%RH}$ values obtained by the CRD and the measured $D_{80\%RH}$, 2) the complex RI retrieved from the $Q_{ext,80\%RH}$ measurements, using the method described in Riziq *et al*. (2007)[71], and 3) the Q_{ext} curve for the complex RI calculated assuming homogeneous mixing and using a volume weighted mixing rule, where the RI for the Pahokee peat aerosol was retrieved from the dry measurements, and the RI value used for water at 532 nm was m = 1.335 + i0.0. [152]

The same analysis was performed for the other substances at both RHs and wavelengths. The RI used for water at 355 nm was m = 1.349 + i0.0.[152] The results are summarized in Table 1, literature growth factor values (when available), ZSR relation calculations, and the percent difference among the different measurements are also shown for comparison. The data in the table is presented in increasing degree of absorption of the proxy aerosols, from AS (no absorption) to Pahokee Peat to AS:Ng 1:1 and to pure nigrosine (highly absorbing).

The retrieved complex refractive indices for all substances at both RHs are in very good agreement with the calculated complex RI from the volume weighted averages; the real part of the RIs are within up to 5.3% of each other. There are greater differences in the imaginary parts, but the values are within measurement errors.

For the IHSS Pahokee peat and nigrosine aerosols, there is an overestimation of the imaginary part at both wavelengths and RHs. Both substances have a small GF, which raises the question of their internal structures after humidification; is there a complete mixture within these particles or a small shell of water formed around the particles forming a core-shell structure which is consequently being measured by the CRD? To explore whether there could be an optical distinction for Pahokee peat and nigrosine if we assume a core-shell

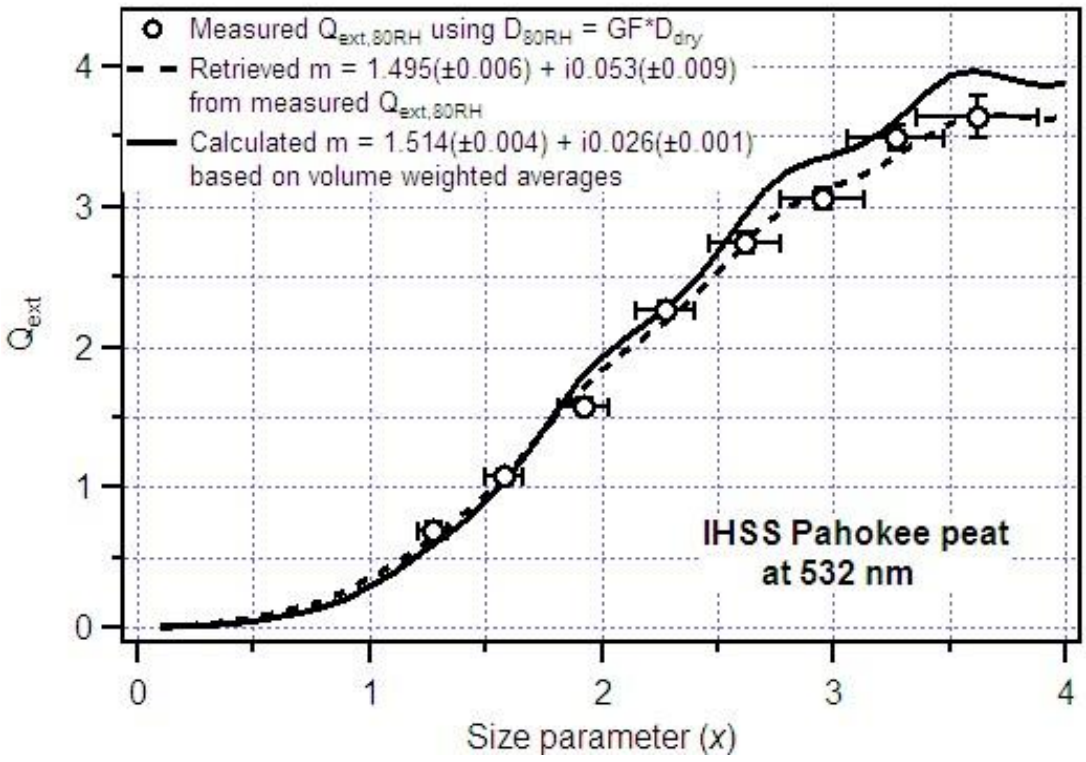

Figure 4.9 Extinction efficiency vs. size at 80% RH for Pahokee peat aerosol. The open circles represent the measured $Q_{ext,80\%RH}$ using the measured hygroscopic growth. The dotted line is the Q_{ext} curve for the retrieved RI from the $Q_{ext,\%RH}$ measurements. The solid line shows the expected Q_{ext} curve from the calculated RI using a volume weighted mixing rule which assumes homogeneous mixing to calculate the complex refractive index.

structure or complete mixing, the extinction efficiency as a function of size parameter was calculated separately for each case. For the homogenously mixed case, $Q_{ext\text{-}homogeneous}$ was calculated using the RI obtained from the volume weighted mixing rule. For the core-shell structure, $Q_{ext\text{-}core\text{-}shell}$ was calculated using the diameter measured after humidification as the total diameter, and the diameter selected from the first DMA as the core diameter. The RI of the core was taken from the dry measurements, and the RI of water was used for the RI of the shell. The code by Liu *et al*. (2007)[38] was used to calculate $Q_{ext\text{-}core\text{-}shell}$, and the code from Bohren & Hoffmann (1983)[37] was used to calculate $Q_{ext\text{-}homogeneous}$. The ratio of $Q_{ext\text{-}core\text{-}shell}$ to $Q_{ext\text{-}homogeneous}$ was calculated and plotted as a function of size parameter for both wavelengths in Figure 4.10. At 80% RH, where Pahokee and nigrosine only grew 9% and 12%, respectively, there is less than a 5% difference between the values obtained with a core-shell structure and those obtained by assuming homogenous mixture for size parameters less than 2.5.

Table 4.1 Measured growth factors, average volume weighted refractive indices, and retrieved refractive indices for all substances at 532 nm and 355nm, at 80% and 90 % RH. The retrieved dry refractive indices are also shown.

			532 nm		355 nm	
	Dry refractive index		m=1.504(±0.015) + *i*0.0(±0.028)		m=1.507(±0.024) + *i*0.005(±0.025)	
			80% RH	**90% RH**	**80% RH**	**90% RH**
Ammonium sulfate	Growth Factor	Measured	1.44(±0.02)	1.77(±0.25)	1.44(±0.02)	1.77(±0.25)
		Literature	1.46 (±0.01)[148, 151, 155]	1.69(±0.01)[151, 155]	1.46 (±0.01)[148, 151, 155]	1.69(±0.01)[151, 155]
		% Difference	1.4	4.6	1.4	4.6
	Ref. Index	Volume Weighted	m=1.39(±0.02) + *i*0.0	m=1.370(±0.02) + *i*0.0	1.40(±0.02) + i0.00(±0.03)	1.39(±0.02) + i0.00(±0.03)
		Retrieved	m=1.437(±0.03) + *i*0.02(±0.04)	m=1.328(±0.01) + *i*0.0(±0.03)	1.42(±0.03) + i0.0(±0.04)	1.41(±0.06) + i0.0 (±0.04)
		% Diff (n)+i(k)	3 + *i*200	3.1 + *i*0	1.5 + i0	2.6 + i0
IHSS Pahokee peat	Dry refractive index		m=1.558(±0.005) + *i*0.033(±0.007)		m=1.541(±0.034) + i0.18(±0.066)	
	Growth Factor	Measured	1.09(±0.01)	1.17(±0.02)	1.09(±0.01)	1.37(±0.02)[c]
		Literature	1.07(±0.01)[156]	1.12(±0.01)[156]	1.07(±0.01)[156]	1.23(±0.01)[156]
		% Diff	1.85	4.4	1.85	10.8
	Ref. Index	Volume Weighted	m=1.514(±0.004) + *i*0.026(±0.007)	m=1.503(±0.009) + *i*0.025(±0.007)	1.497(±0.034) + i0.139(±0.066)	1.424(±0.034) + i0.07(±0.066)
		Retrieved	m=1.495(±0.006) + *i*0.053(±0.009)	m=1.517(±0.008) + *i*0.025(±0.014)	1.578(±0.047) + i0.171(±0.072)	1.415(±0.045) + i0.064(±0.053)
		% Diff (n)+i(k)	1.3 + *i*68	0.9 + *i*0	5.3 + i20	0.6 + i8.9
AS : Nig[b]	Dry refractive index		m=1.595(±0.031) + *i*0.154(±0.021)		m=1.431(±0.034) + i0.178(±0.066)	
	Growth Factor	Measured	1.28(±0.02)	1.45(±0.02)	1.28(±0.02)	1.45(±0.02)
		Literature	1.29(±0.02)[a]	1.45(±0.1)[a]	1.29(±0.02)[a]	1.45(±0.1)[a]
		% Diff	0.8	0	0.8	0
	Ref. Index	Volume Weighted	m=1.431(±0.031) + *i*0.084(±0.021)	m=1.396(±0.031) + *i*0.046(±0.021)	1.388(±0.034) + i0.084(±0.066)	1.378(±0.034) + i0.058(±0.066)
		Retrieved	m=1.40(±0.01) + *i*0.086(±0.013)	m=1.329(±0.008) + *i*0.04(±0.017)	1.402(±0.037) + i0.079(±0.058)	1.377(±0.05) + i0.087(±0.064)
		% Diff (n)+i(k)	2.2 + *i*2.3	4.9 + *i*14	1.0 + i6	0.01 + i40
Nigrosine	Dry refractive index		m=1.626(±0.021) + *i*0.243(±0.023)		m=1.568(±0.056) + i0.305(±0.171)	
	Growth Factor	Measured	1.12(±0.02)	1.24(±0.1)	1.12(±0.02)	1.24(±0.1)
		Literature	1.15[d]	1.34[d]	1.15[d]	1.34[d]
		% Diff	2.6	7.8	2.6	7.8
	Ref. Index	Volume Weighted	m=1.544(±0.021) + *i*0.174(±0.023)	m=1.493(±0.021) + *i*0.132(±0.023)	1.508(±0.056) + i0.217(±0.171)	1.465(±0.056) + i0.160(±0.171)
		Retrieved	m=1.464(±0.004) + *i*0.216(±0.014)	m=1.504(±0.012) + *i*0.168(±0.024)	1.542(±0.066) + i0.249(±0.14)	1.477(±0.058) + i0.145(±0.087)
		% Diff (n)+i(k)	5.3 + *i*21.5	0.7 + *i*24	2.2 + i14	0.8 + i9.8

[a] Derived using the ZSR relation. [b] 1:1 molar ratio. [c] Measurement performed at 95% RH.
[d] Taken from https://sciencepolicy.colorado.edu/events/rendezvous/2007/posters/II21K.pdf

For 90% RH, the differences between the core-shell structure and a homogeneously mixed particle are more noticeable, with up to a 7% difference for the Pahokee peat. A clear distinction between the two mixing states can be observed at size parameters greater than 3. Mie curves of homogenously mixed particles with similar real part of the RI will have the maximum Q_{ext} value around the same size parameters —for real parts between 1.65 and 1.55 (the real parts of the RIs of Pahokee peat and nigrosine are between these values) the Q_{ext} peaks start around a size parameter of 2.5— for purely scattering substances it will be a series of resonance peaks. As the imaginary part of the complex RI increases the Q_{ext} peaks will accordingly decrease. Hence, if a substance is assumed to be homogenously mixed, when its internal structure is in reality a core-shell, the measured Q_{ext} will be lower and it will result in an underestimation of the imaginary part of the complex refractive index when it is calculated with the volume weighted mixing rule. This can be seen in Figure 4.9, where the difference between the measurements (open circles) and the homogeneous assumption (solid line) is greater at size parameters ≥ 3, and by having assumed a homogenous mixture the imaginary part of the RI was slightly underestimated.

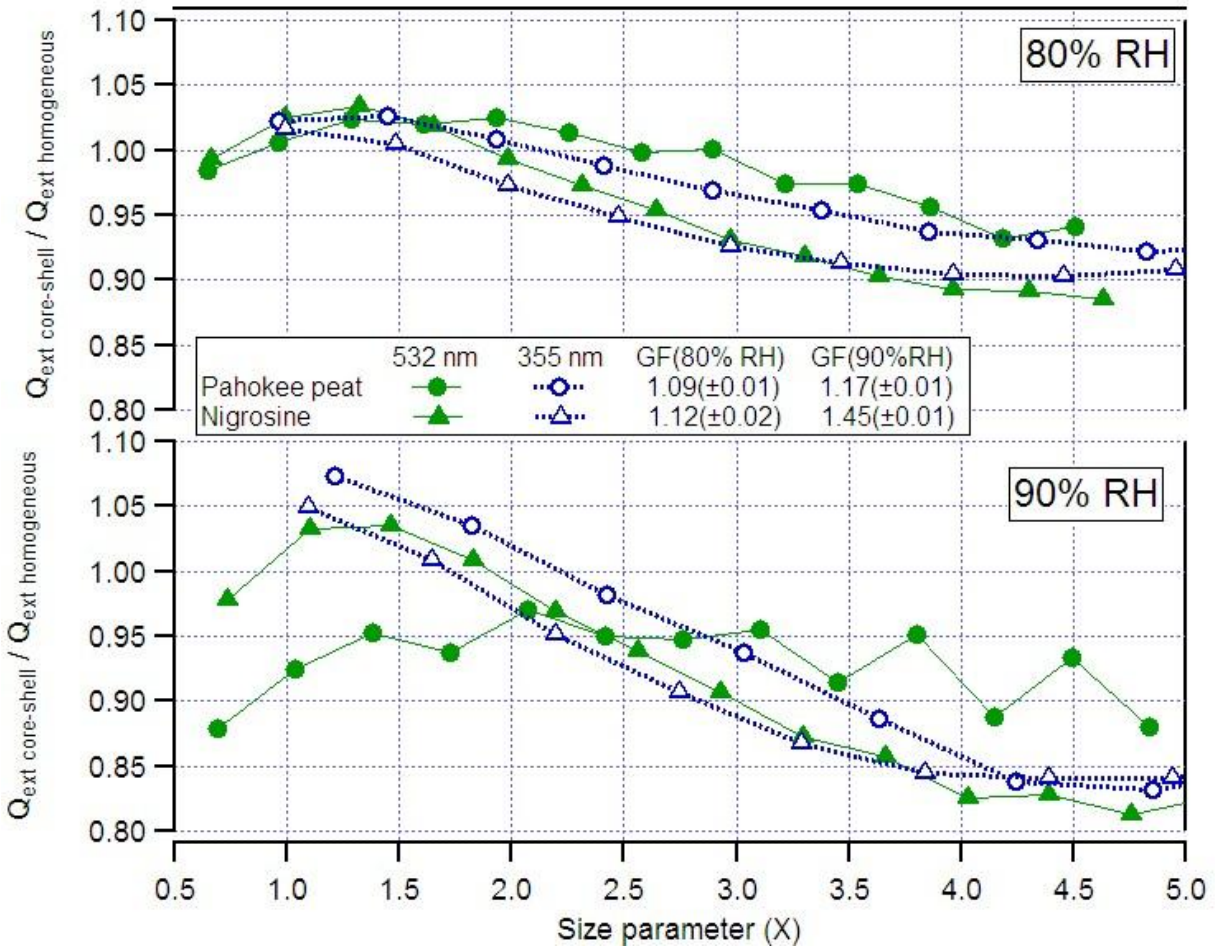

Figure 4.10 Ratio of Qext-core-shell to Qext-homogeneous as a function of size parameter for Pahokee peat (circles) and nigrosine(triangles) at 532 nm(green) and 355 nm(blue) at 80% and 90% RH. The growth factor for both substances at 80% and 90% RH are written in the legend for comparison.

These small discrepancies between the retrieved complex RI from direct measurements and the complex RI calculated from the volume weighted mixing rule suggest the volume weighted mixing rule is a good approximation for water soluble aerosols at high RH conditions; especially for substances with GF > 1.25. The homogenous mixture assumption for particles with small GF (less than 1.25) needs to be taken with caution for size parameter greater than three; for size parameters less than three there is no optical difference between the two assumptions of the internal structure of the particles.

4.7 Summary and Conclusions

The dependence of light extinction on RH for water soluble substances with different degrees of absorption was explored at two wavelengths, λ= 355 nm and 532 nm. The $f\mathrm{RH}_{ext}$(%RH,Dry) dependence on size changes from having an exponential dependence for purely scattering substances to demonstrating practically no dependence for absorbing substances with an imaginary part greater than zero. There is no clear evidence for the effect of $Q_{ext-\%RH} \,/\, Q_{ext-Dry}$ on the behavior of $f\mathrm{RH}_{ext}$(%RH,Dry), however, by analyzing two substances with the same GF, information on the influence of the imaginary part on $f\mathrm{RH}_{ext}$(%RH,Dry) was obtained. At 532 nm absorption decreased the magnitude of $f\mathrm{RH}_{ext}$(%RH,Dry) for diameters less than 450 nm and increased the magnitude for greater sizes. At 355 nm, with the exception of 200 nm particles, the magnitude of $f\mathrm{RH}_{ext}$(%RH,Dry) increased with size. It is premature to parameterize the dependence of $f\mathrm{RH}_{ext}$(%RH,Dry) on absorption, as more measurements are needed to quantify the influence of the $Q_{ext-\%RH} \,/\, Q_{ext-Dry}$ factor on the behavior of $f\mathrm{RH}_{ext}$(%RH,Dry) with size. For future work, I propose to conduct a series of measurements using purely scattering organic substances with similar growth factors mixed at different ratios with nigrosine or any other absorbing soluble material. For non soluble materials the experiments are more complicated as the lack of sphericiy can greatly influence the results (e.g. soot, mineral dust).

The validity of the volume weighted mixing rule at 355nm and 532nm was also investigated. I compared the complex refractive index of the humidified substances derived using the GF and the extinction coefficients measured by the SMPS and CRD, respectively, to the complex refractive index calculated with the volume weighted mixing rule using the dry complex refractive index of each substance, and the complex RI of water. It was found that the difference between the derived and calculated real parts of the complex RIs were less than 5.3% for all substances, wavelengths, and RHs. The obtained imaginary parts for the retrieved and calculated RIs were in good agreement with each other, and well within the measurement errors of retrieval from pulsed CRD spectroscopy measurements. There were some cases with high percent differences, but those were attributed to a non homogeneous mixing for substances with low growth factors such as IHSS Pahokee peat and nigrosine.

Finally, whether the difference between assuming a core-shell structure or a homogenously mixed particle could have a significant effect on the calculated RI value of substances with low growth factors, i.e., nigrosine and Pahokee, was explored. It was found that at 80% RH and for size parameters less than 2.5, there is less than a 5 % difference between the extinction efficiencies calculated with a core-shell model and a homogenous mixture model. This difference is within measurement errors; hence, there is no significant difference between the models in this case. However, for greater size parameters the difference can be up to 10%. For 90% RH the differences below a size parameter of 2.5 were up to 7%.

The measurements presented here demonstrate that the volume weighted mixing rule is a good approximation for water soluble absorbing substances under 80% and 90% relative humidity conditions, and will be used as a basis to investigate how the twilight zone of warm clouds would change if aerosols with different degrees of absorption, from purely scattering to highly absorbing, are present.

5 Optical properties of combustion soot, secondary organic aerosol, and their internal mixture

5.1 Introduction

Soot carbon ("soot"), an impure form of near-elemental carbon with graphite-like structure, which is formed in flaming combustion and in internal combustion engines,[157, 158] is one of the most efficient absorbers of light in the atmosphere. Soot particles consist primarily of 10 – 50 nm spherules of soot, which cluster together immediately after their formation to form aggregates [26, 35, 159] (see Figure 5.1). It is estimated that annually, about 8 Tg of soot are emitted globally into the atmosphere,[21] and it has an estimated lifetime of one (±1) week.[160] In terms of radiative forcing, soot is the second or third largest individual warming agent, following carbon dioxide and possibly methane. [161, 162] The high absorption of light by soot can play an important role in the direct and semi-direct effects of particles on the Earth's climate.[15, 96] The absorption of light heats the absorbing particles and their surroundings, thereby influencing local relative humidity profiles, cloud formation and lifetimes, and atmospheric circulation.[5, 101, 107] Moreover, the radiative balance of the earth-atmosphere system can be affected through a complex web of processes: [163] 1) by the reduction of the incident solar radiation below the aerosol layer;[7, 8] 2) by the absorption of the solar radiation reflected by the surface–atmosphere–cloud system, soot reduces the albedo of the planet;[164] 3) soot deposited over snow and sea ice can decrease the surface albedo;[12, 165, 166] and 4) soot inside cloud drops and ice crystals can decrease the albedo of clouds by enhancing absorption by droplets and ice crystals.[127, 145, 167]

Studies have shown that a large fraction of atmospheric soot exists as an internal mixture with water soluble compounds (mostly sulfate), and that internally mixed soot represents a globally significant fraction of the tropospheric aerosol,[168-170] but no quantitative mixing ratios are inferred from these results. Moreover, it is well known that if the internal mixture has a core-shell structure, a purely scattering shell surrounding the absorbing core, it can enhance the absorption of the core.[171] This effect arises from the fact that the purely scattering shell acts as a lens focusing more photons into the core than would have reached it otherwise. Bond *et al.* (2006)[172] showed theoretically that for core and shell sizes typical of the atmosphere, there can be an absorption increase of 50 – 100% by an individual soot particle. This absorption enhancement is thought to have and important influence on the radiative forcing of soot.[106] A few recent experiments have observe the absorption enhancement due to the lensing effect. Lack *et al.* (2009)[173] coated absorbing polystyrene latex spheres with organic material, Shiraiwa *et al.* (2009)[174] coated graphite with oleic acid or glycerol, and Lack *et al.* (2009)[175] observed the enhancement for absorbing mineral dust coated in aqueous inorganic material. Schnaiter *et al.* (2005)[35] and

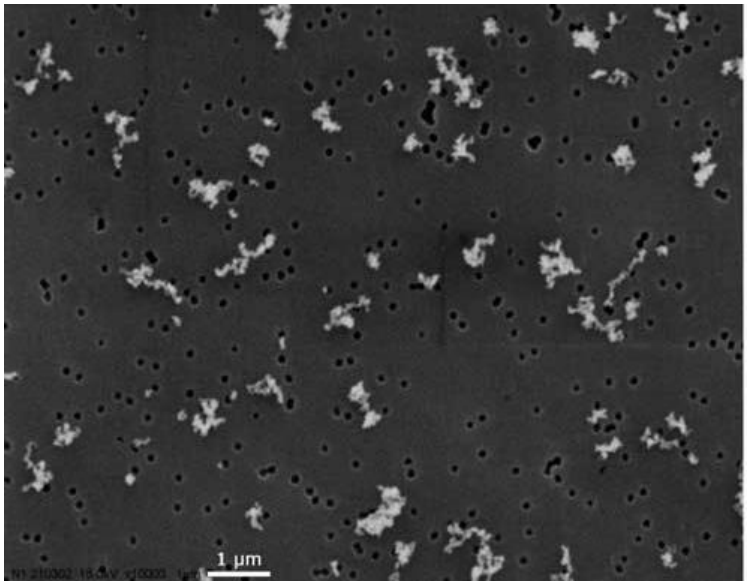

Figure 5.1. SEM micrographs of Diesel soot aggregates. Taken from Schnaiter *et al.* (2005)[35]

Zhang *et al.* (2008)[176] coated soot particle with secondary organic aerosol (SOA) and sulfuric acid, respectively. More recently, Khalizov *et al.* (2009)[177] measured the enhancement of light absorption and scattering of soot coated with sulfuric acid. However, the three latter studies derived the absorption enhancement from the difference method (extinction minus scattering), and not from a direct measurement of absorption.

Another source of uncertainty in the optical properties of soot it its complex refractive index. From an inter-comparison of experimentally determined RIs for different types of soot, Fuller *et al.* (1999)[171] reported a range between 1.50 + i0.50 to 2.67 + i1.3 at λ=550nm as typical values for the different solid state structures of soot material. On the other hand, Bond and Bergstrom (2006)[22] suggested that in the visible spectrum the RI of light absorbing carbon (LAC) to be constant, and depending on the amount of voids in the particle the derived RIs will fall in a void-fraction line (see Figure 5.7 or Figure 7 of their paper). From this void-fraction line Bond and Bergstrom (2006)[22] 'best guess' for the refractive index of light absorbing carbon (LAC) falls in the higher values, with a range of m = 1.85(±0.1) + i0.71(±0.08) at 550 nm. Adler *et al.* (2009)[60] used this value of the RI to calculate mass absorption cross section (MAC) at 532 nm and 355 nm for diesel soot and found their values to be in good agreement with the Bond *et at.* (2006)[172] suggested value of 7.5 m^2 g^{-1} at 550nm. Schnaiter *et al.* (2005)[35] deduced an RI of m = 1.9 + i1.0 for diesel soot using the aerosol model COSIMA[178] and the Rayleigh-Debye-Gans theory, and recently Moteki *et al.* (2010)[179] measured an RI of soot in Tokyo's urban area of m = 2.26 (±0.13) + i1.26(±0.13). The variability in the complex refractive indices of soot is still too large and therefore more measurements are needed.

In this study, results of two simulation experiments conducted at the large aerosol chamber facility AIDA (see Möhler *et al.* (2003),[180] for a detailed description) of the Karlsruhe Institute of Technology, Karlsruhe, Germany, are presented. Soot aerosol particles from a Combustion Aerosol Standard were coated with secondary organic aerosols (SOA)

generated by the ozonolysis of α-pinene. The non absorbing SOA particles with strongly absorbing soot inclusions were investigated as the geometry resembles the internally mixed soot particles in the atmosphere, and are good proxies for soot/sulfate mixtures which may be more frequent in the atmosphere. The optical properties of the particles were monitored using a cavity ring down spectrometer (CRD) and a photoacoustic sensor (PAS) at 532nm. By using a Mie model for homogenous[37] and coated spheres[38] the refractive indices of the SOA and the internally mixed soot particles with SOA were derived, respectively. This study also aims to further investigate the magnitude of the absorption enhancement of soot when coated with a purely scattering substance.

5.2 Experiments

The AIDA chamber is an aluminum vessel with an 84 m^3 volume, the temperature of the chamber can be controlled to be between -90°C to +60°C, and the pressure can be decreased down to 0.01 mbar. The chamber allows for simulations of atmospheric aerosol processes on the time scale of days.[35]A schematic of the instrumentation setup is depicted in Figure 5.2. A Combustion Aerosol Standard (CAST; Jing-CAST Technologies) was used to generate carbonaceous aerosols with a specific organic carbon (OC) to elemental carbon (EC) mass ratio. This was done by varying the propane-to-air ratio (C/O atomic ratio). For these experiments the CAST was set to a C/O=0.29, which corresponds to about 90% EC and 10% OC.[181] The particle concentration inside the chamber was monitored with a Condensation Particle Counter (CPC; TSI model 3022A). The aerosols number size distribution was measured with a Scanning Mobility Particle Sizer (SMPS) composed of a Differential Mobility Analyzer (DMA; TSI model 3071) and a CPC (TSI model 3010). The mass of refractory black carbon was measured with a Single Particle Soot Photometer (SP2; Droplet Measurement Technologies). The extinction and absorption coefficients at 532 nm were measured with a Cavity Ring Down Spectrometer (CRD) and a Photoacoustic Sensor (PAS) placed in series. A CPC (TSI model 3022A) was located at the exit of the PAS to directly count the particle concentration inside the CRD and the PAS. To measure the extinction efficiency (Q_{ext}) of particles of specific sizes, a DMA (TSI model 3081) was placed before the CRD-PAS-CPC system (marked with the dashed square in Figure 5.2) for generation of a monodisperse aerosol population. The PAS was calibrated before each experiment using the validated method described in Chapter 2.5.

A mixing fan, located near the bottom of the chamber, helped maintain homogeneous conditions within the chamber. Before the beginning of the experiments the chamber was evacuated and filled to ambient pressure with humidified particle free synthetic air (low hydrocarbon grade, Linde). The experiments were conducted with initial relative humidities between 18% and 22% and background particle concentrations of <0.1 cm^{-3}.

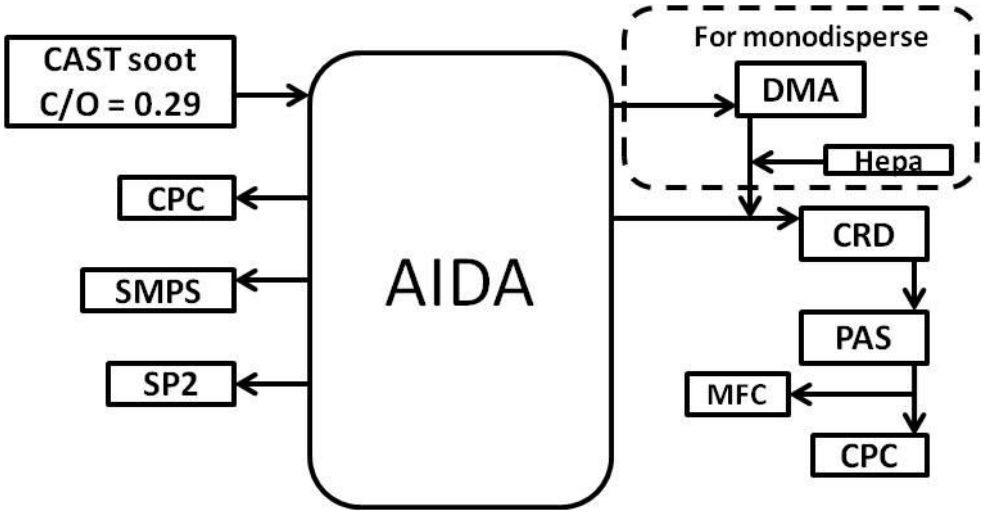

Figure 5.2. Schematic of the instrumentation setup in the AIDA chamber. For monodisperse measurements a DMA was placed before the CRD-PAS-CPC system, marked with the dotted square. DMA, differential mobility analyzer; CRD, cavity ring down spectrometer; PAS, photoacoustic sensor; CPC, condensation particle counter; SP2, single particle soot photometer; SMPS, scanning mobility particle sizer; CAST, combustion aerosol standard.

Two different experiments were performed: the first experiment began with homogeneous nucleation of secondary organic aerosol in particle-free air by the ozonolysis of α-pinene (SOA-αO_3), and soot aerosols were added after the nucleation mode stabilized (referred to as 'SOA-soot' from this point forward), yielding a population of externally mixed soot with SOA-αO_3 particles. The second began with the injection of CAST soot aerosols at a C/O=0.29 which were allowed to coagulate for approximately 28 hours before coating them with SOA-αO_3 (referred to as 'Coat-0.29'). The temperature during the experiments was 26.1 (±0.2) ° C and 24.5 (±1) ° C for the SOA-soot, and Coat-0.29, respectively.

The SOA-soot nucleation experiment was performed to derive the complex refractive index (RI) of the organic material which was used to coat the coagulated soot particles of the Coat-0.29 experiment, as well as to compare the differences in the single scattering albedos between coagulated soot with SOA-αO_3 (resembling and external mixture) and coated soot with SOA-αO_3. The SOA-soot experiment began with the addition of around 300 ppb of ozone to the particle-free chamber. Subsequently, 10 ppb of α-pinene were added by evaporating ca. 4.1 hPa α-pinene (99%, Aldrich) into a 1-liter glass bulb, and flushing air for 7 minutes (Schnaiter, personal communication; see Saathoff *et al*. (2003b)[182]for the details of the SOA yield determination). The nucleation mode served as seed aerosol before the subsequent addition of 250 ppb of ozone and 49 ppb of α-pinene. The particle concentration reached a maximum of 6 x 10^4 cm^{-3}, and the SOA-αO_3 grew to a maximum median diameter of ~160 nm. After the SOA-αO_3 growth stabilized, 25 μg m^{-3} of soot (C/O=0.29) were added, the soot and SOA-αO_3 were allowed to stabilize before a second injection of 25 μg m^{-3} of soot (C/O=0.29). After the last injection of soot, the SOA-αO_3 and soot were left to coagulate for another 22 hours.

For the Coat-0.29 experiment, approximately 100 μg m^{-3} of soot (C/O=0.29) were introduced to the chamber and allowed to coagulate for a period of about 28 hours before performing two *in-situ* coating steps with SOA-αO_3. For the first coating step, 260 ppb of ozone were added followed by 49 ppb of α-pinene. For the second coating step 270 ppb of ozone and 49 ppb of α-pinene were injected. New particle formation by SOA-αO_3 nucleation was observed with concentrations below 100 p/cm^{-3}, which can be considered negligible compared with the soot particle concentration. Monodisperse measurements were performed at the end of the last coating step.

For the two experiments the optical and microphysical properties were continuously measured.

5.3 Results

5.3.1 Optical properties of SOA coagulated with soot

Figure 5.3 shows the temporal evolution of the extinction and absorption coefficients, the single scattering albedo (SSA), the median mobility diameter ($\overline{D}_m$), and the total particle concentration of the SOA-soot experiment. The homogeneous nucleation of the SOA-αO_3 was performed in the first 300 minutes of the experiment. The gap centered at around the 200^{th} minute of the experiment is the period where monodisperse measurements were performed. The two occasions where soot (C/O=0.29) was injected to coagulate with the SOA-αO_3 are marked with the vertical grey lines. These points are also marked by a decrease in $\overline{D}_m$ and a sharp increase in the extinction and absorption coefficients, and the particle number concentration. For the homogenously nucleated SOA-αO_3, there is a clear increase in the extinction coefficient with particle growth, while the absorption coefficient remains at zero, in accordance with the non-absorbing nature of SOA-αO_3. SSA values of less than one are due to the injection of ozone for the second nucleation step; however, the absorption coefficient and the SSA remain constant at values close to zero and one, respectively. After every injection of CAST soot into the chamber there is a marked decrease in the SSA, the first one from 1 to an average constant value of 0.69(±0.02), and the second to an also constant value of 0.50(±0.02). This implies there is a rapid (within minutes) stabilization of the mixture of SOA-αO_3 and soot, and that the growth by coagulation, indicated by the increase of the median mobility diameter ($\overline{D}_m$) of soot and homogenously nucleated SOA-αO_3 does not change the optical properties.

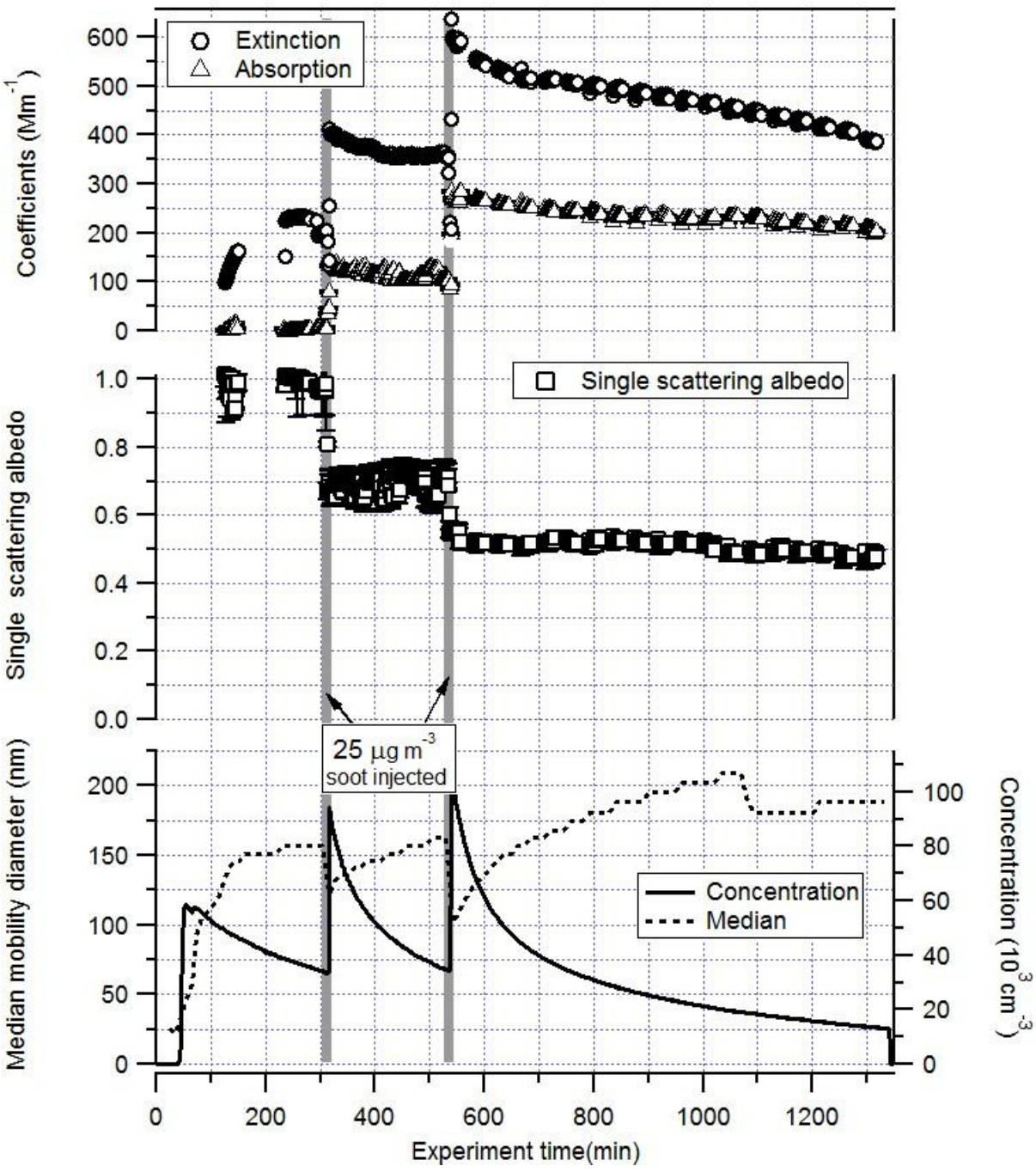

Figure 5.3 Time series of the extinction (circles) and absorption (triangles) coefficients, the single scattering albedo (squares), the mobility median diameter (dotted line), and the particle number concentration (solid line) for the SOA-soot experiment. The times in which 25 µg m^{-3} of CAST soot (C/O=0.29) were injected to the chamber are marked with the vertical grey lines.

5.3.2 Complex refractive index of SOA by ozonolysis of α-pinene

To obtain the complex RI of homogenously nucleated SOA-αO_3, measurements were conducted for monodisperse aerosol populations with sizes ranging from 130 nm to 220 nm in 15 nm steps. By calculating the extinction efficiency (Q_{ext}) for every diameter and using Mie theory and equation 2.20 in Chapter 2, a refractive index was derived. Figure 5.4 shows the measured Q_{ext} vs. size parameter, and the best fit RI curve obtained. A refractive index at 532 nm of m = 1.471 (±0.008) + i0.0 (±0.002) was derived from these measurements. There have been several laboratory studies where the refractive index of SOA has been reported. They are summarized in Table 5.1.

The values from this study are in good agreement with literature values for SOA generated by the ozonolysis of α-pinene. Specifically, Schnaiter *et al.* (2003)[183] and Schnaiter *et al.* (2005)[35] determined a wavelength-independent RI at λ > 350 nm of m = 1.44 and m = 1.5, respectively, by measuring the wavelength dependence of aerosol extinction and scattering (the SOA-αO_3 was generated using the same procedure as for this study). Wex *et al*. (2009)[184] found the value of the real part of the RI to be m = 1.45 by measuring the particle size dependence of scattering at visible wavelengths. Nakayama *et al.* (2010)[185] retrieved a complex RI at 532 nm of m = 1.41(±0.02) + i0.00(±0.02) by minimizing the Q_{ext} measured using a CRD of a polydisperse distribution with a theoretical Q_{ext} calculated with the size distributions from a Scanning mobility particle sizer. Kim *et al.* (2010)[186] used polar nephelometer measurements at 670 nm and measured particle size distributions together with a genetic algorithm method with Mie-Lorenz scattering theory to derive real RI values between 1.4 and 1.5. There is less than a 5% difference in the real part of the complex refractive index retrieved in this study and previous ones. Larger differences are observed for SOA generated by other methods.

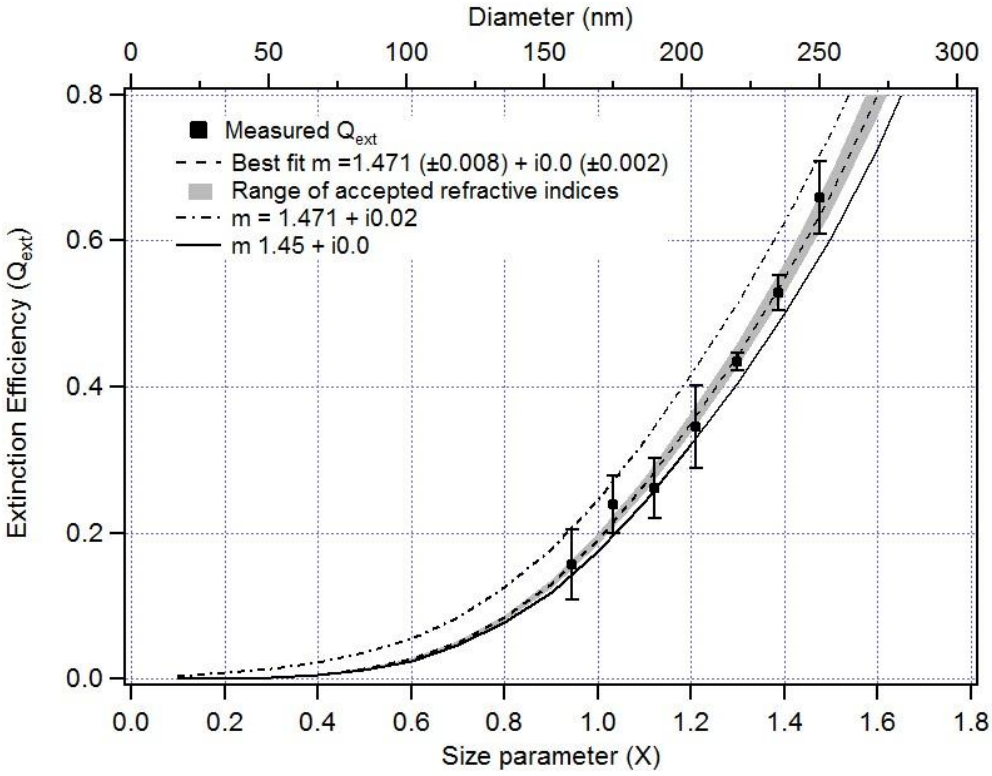

Figure 5.4 Extinction efficiency (Q_{ext}) vs. size parameter for the monodisperse measurements of SOA formed by ozonolysis of α-pinene. The dotted line is the theoretical curve for the derived complex refractive index, the shaded area are the range of accepted theoretical curves, the dot-line curve shows the extent of the deviation if the imaginary part is increased by *k*=0.02, and the solid line shows the extent of the deviation if the real part is varied by *n*=0.02.

Table 5.1. Complex refractive indices of Secondary Organic Aerosols

Reactions	Complex refractive index m = *n* + i*k*	Wavelength (nm)	Reference
	1.44 + i0.0	>350	Schnaiter *et al.* (2003)[183]
	1.5 + i0.0	>350	Schnaiter *et al.* (2005)[35]
	1.45	visible	Wex *et al.* (2009)[184]
Ozonolysis of α-pinene	1.46(±0.02) + i0.00(+0.02)	355	Nakayama *et al.* (2010)[185]
	1.41(±0.02) +i0.00(+0.03)	532	Nakayama *et al.* (2010)[185]
	1.4 – 1.5	670	Kim *et al.* (2010)[186]
	1.42 (±0.02)	670	Barkey *et al.* (2007)[187]
Photooxidation of α-pinene	1.56 (±0.04)	450	Yu *et al.* (2008)[188]
in the presence of NO_x	1.51 (±0.03)	550	Yu *et al.* (2008)[188]
	1.46 (±0.03)	700	Yu *et al.* (2008)[188]
Photooxidation of toluene	1.63(±0.04) + i0.05(±0.04)	355	Nakayama *et al.* (2010)[185]
in the presence of NOx	1.48(±0.03) +i0.01(+0.03)	532	Nakayama *et al.* (2010)[185]
Photooxidation of VOCs	1.53 (±0.08) +i0.00(±0.05)[a]	532	Lang-Yona *et al.* (2010)[67]
emitted from Holm Oak	1.53 (±0.06) + i0.00 (±0.04)[b]	532	Lang-Yona *et al.* (2010)[67]
Ozonolysis of α-pinene	1.47 (±0.01) + i0.0(±0.01)	532	This study

[a]Oxidation induced formation.
[b]Volatile organic compound induced formation.

5.3.3 Optical properties of coagulated soot coated by SOA

The time line for the Coat-0.29 experiment is presented in Figure 5.5 with the same variables as in Figure 5.3. Initially around 100 μg m^{-3} of CAST soot were injected into the AIDA chamber and allowed to coagulate for approximately 28 hours before performing coating steps with SOA-αO_3. The dark grey area indicates when the two coating steps were performed. Figure 5.3 shows that the soot grew from a $\overline{D}_m$= 70 nm to about $\overline{D}_m$= 340 nm before the coating steps, which is due to the coagulation of the fractal like aggregates. The $\overline{D}_m$ slightly decreased after the coating steps, due to a change in the shape of the coagulated coated soot. After long coagulation times the addition of a coating layer will cause the soot particles to collapse into more compact particles.[182, 183] The fresh soot SSA had an average value of 0.2(±0.03) before the first coating with SOA-αO_3. After the injection of 260 ppb of O_3 and 49 ppb of α-pinene, there was a clear increase in the SSA to 0.5(±0.01). After the second coating step the SSA increased further to an average value of 0.71(±0.03). Some experiments have been performed where the optical properties of fresh soot have been measured. Khalizov *et al.* (2009)[177] measured a SSA of 0.09 for soot generated by incomplete combustion of propane in a laminar diffusion burner, Schnaiter *et al.* (2003)[183] and Schnaiter *et al.* (2005)[35] measured a SSA for fresh diesel soot of 0.2 and 0.18, respectively. The SSA value of the CAST soot with the C/O ratio of 0.29 agrees very well with the SSA measured by Schnaiter and co-workers, while it is higher than the one measured by Khalizov *et al.* (2009).[177] The difference from Khalizov *et al.* (2009)[177] might be due to the different burning conditions, as the calculated fractal dimension from the three studies did not vary considerably; 2.1, 2.0, and 2.2 for Khalizov *et al.* (2009),[177] Schnaiter *et al.* (2003),[183] and Schnaiter *et al.* (2005)[35] respectively. A preliminary fractal dimension of 2.05 was derived using the COSIMA model for the soot measured in this study (Schnaiter personal communication), which is in good agreement with the previous measurements.

Together with the increase in the SSA there was an increase in the absorption coefficient from an average value of 206.3 (±1) Mm^{-1} to around 356.7(±1) Mm^{-1}, an absorption enhancement of about 1.72 (±0.01) times. The absorption enhancement by coated soot with a purely scattering substance was also explored by Schnaiter *et al.* (2005);[35] they found an absorption enhancement of 1.8 to 2.1. Zhang *et al.* (2008)[176] coated soot particle with SOA and sulfuric acid and exposed them to 80% relative humidity, they found an increase in absorption of nearly 2. More recently Shiraiwa *et al.* (2010)[174] measured absorption enhancements of 1.2 up to 2 for graphite particles coated with different thicknesses of oleic acid and glycerol. The lower absorption enhancement was measured for a total diameter (D_p) to core diameter (D_c) ratio of 1.2, and the larger enhancement was found for D_p/D_c = 2. The absorption enhancement measured by the PAS for the Coat-0.29 experiment lies below the measured absorption enhancement from Schaiter *et al.* (2005),[35]

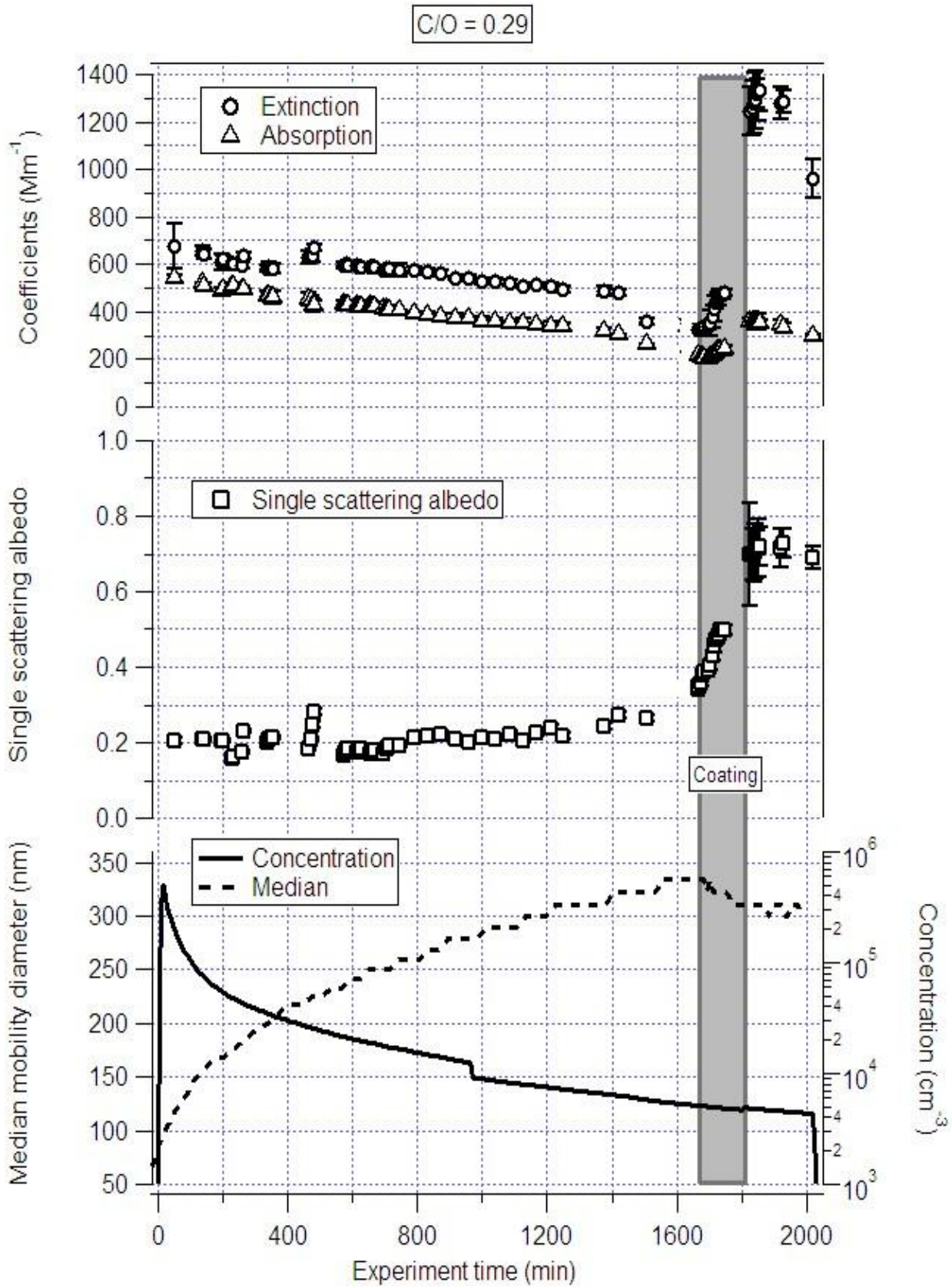

Figure 5.5 Time series of the extinction (circles) and absorption (triangles) coefficients, the single scattering albedo (squares), the mobility median diameter (dotted line), and the particle number concentration (solid line) for the Coat-0.29 experiment. The experiment began with approximately 100µg m^{-3} of CAST soot. The dark grey area indicates where coating steps were performed by the condensation of SOA by the ozonolysis of α-pinene.

but they performed up to five coating steps, compared to only two coating steps performed in this study.

5.3.4 Refractive index retrieval of the soot core

After the last coating step of the Coat-0.29 experiment, monodisperse measurements of the coated soot were performed for particles ranging from 250 nm to 600nm in 25nm steps. By using a concentric core shell model[38] the Q_{ext} of specific diameters can be calculated for different shell thicknesses and RIs of the core and the shell. By using monodisperse measurements of the coated soot with SOA-αO_3, the total diameter (core plus shell) is obtained from the chosen mobility diameter in the DMA, the Q_{ext} for every diameter is calculated from the CRD measurements, and the RI of shell is derived from the SOA-soot experiment; only the shell thickness and the core's RI remain unknown. Using the measured variables and varying the unknown ones in the concentric core shell model[38] the RI of the soot core can be derived together with an estimation of the coating thickness.

The derivation of the RI for the soot core was performed by varying both the thickness of the shell and the core refractive index. The retrieval algorithm compares the measured extinction efficiency as a function of size parameter with the extinction efficiency calculated using the core shell model code by Liu *et al.* (2007),[38] while simultaneously varying the real and imaginary parts of the core refractive indices for different coating thicknesses of the particles. It finds the complex refractive index that minimizes χ^2/ N^2 for every coating thickness, where χ^2 is defined as:

$$\chi^2(n,k,T) = \sum_{i=1}^{N} \frac{(Q_{ext\ measured} - Q_{ext\ calculated})_{i,k}^2}{\varepsilon_i^2} \qquad (5.1)$$

N is the number of diameters measured, n and k are the real and imaginary parts of the RI, respectively, T is the thickness of the shell which for this experiment was varied from 1 nm to 20 nm in 1 nm steps, and ε is the estimated error in the measurement. The minimum χ^2 for every coating thickness are compared, and the values of RI and coating thickness which yield the minimum χ^2 among these are taken as the best RI and coating thickness. The refractive index of the shell was kept at m = 1.471 + i0, the real part of the RI for the core was allowed to vary between 1.3 and 2.3, and the imaginary part from 0 to 1. Coating thicknesses with complex RIs which provided χ^2 values within 5% of the minimum χ^2 were also taken as valid.

It must be noted that this derivation assumes the same coating for all the sizes, i.e. assuming a 10 nm coating will mean a 300 nm total diameter measured will have a core of 290 nm and a 600 nm total diameter will have a core diameter of 590 nm. This may not be the case as it is possible to have a distribution of core and shell diameters; however, this data

is not available yet and the Kelvin effect[§§][189-191] for particles greater than ~70 nm diameter is negligible.[192, 193] Furthermore, it is not well understood whether the soot collapses into a sphere or another shape, whether the coating is homogenous around the particle, or whether there are some inclusions of SOA in the soot core. These unknowns will increase the error in the derivation of the complex refractive index. Some of the questions might be resolved in the ongoing analysis of the measurements performed with the Single particle soot photometer (SP2) which gives a direct measurement of the soot's mass and the SP2 – AMS (Aerosol Mass Spectrometer), which can provide a chemical analysis of the components present in the collapsed soot cores. There is ongoing research on this topic; hence the results given here must be taken as preliminary rather than final.

The measured Q_{ext} as a function of size parameter are depicted in Figure 5.6, and three different fitting curves are shown in addition to the measured data. The solid red curve was obtained by the Mie core shell fit using all particle sizes, a coating thickness of 1 nm was obtained and a core complex refractive index of m = 2.18 + i0.36. However, this coating thickness seems too thin and the measured points between 250 nm and 300nm could have been affected by doubly charged particles, and therefore overestimating their Q_{ext} values. The dotted blue line is the best Mie fit obtained for a subset of the sizes beginning at 325 nm (the first three points, marked with the circle, were excluded from the calculation), yielding a core RI of m = 2.04 + i0.34 and a coating thickness of 10 nm. Coating thicknesses from 4 nm to 14 nm also yielded χ^2 within 5 % of the minimum χ^2; the best Mie fits for the accepted coating thickness are represented by the grey lines.

Figure 5.7 shows the different refractive indices compiled by Bond and Bergstrom (2006)[22] and the RI derived in this study (marked with a black inverted triangle). The RI derived for the soot core falls slightly below the graphitization curve and considerably lower than the void-fraction curve.

The void-fraction curve assumes that light absorbing carbon has a single complex refractive index and that variation can be expressed by the Bruggeman effective-medium theory.[22] From Figure 5.7 we can observe that the assumptions made in the derivation of the complex refractive index of the soot core are not well founded and that more information is needed for an accurate derivation. Another method for obtaining a better derivation will be to use a thermodenuder before doing the monodisperse measurements to extract the SOA-αO_3 from the coated particle and only measure the collapsed soot core. This will only leave the uncertainty of the shape of the particle.

[§§] The vapor pressure of water in equilibrium with an aqueous solution drop at a given temperature depends only on the solute and its concentration and on the size of the drop. [188,189] This size dependence, which is due to the surface tension of the solution–air interface, is known as the Kelvin effect. [190] In other words, greater partial pressure is required to maintain mass equilibrium for curved surfaces than for flat surfaces.

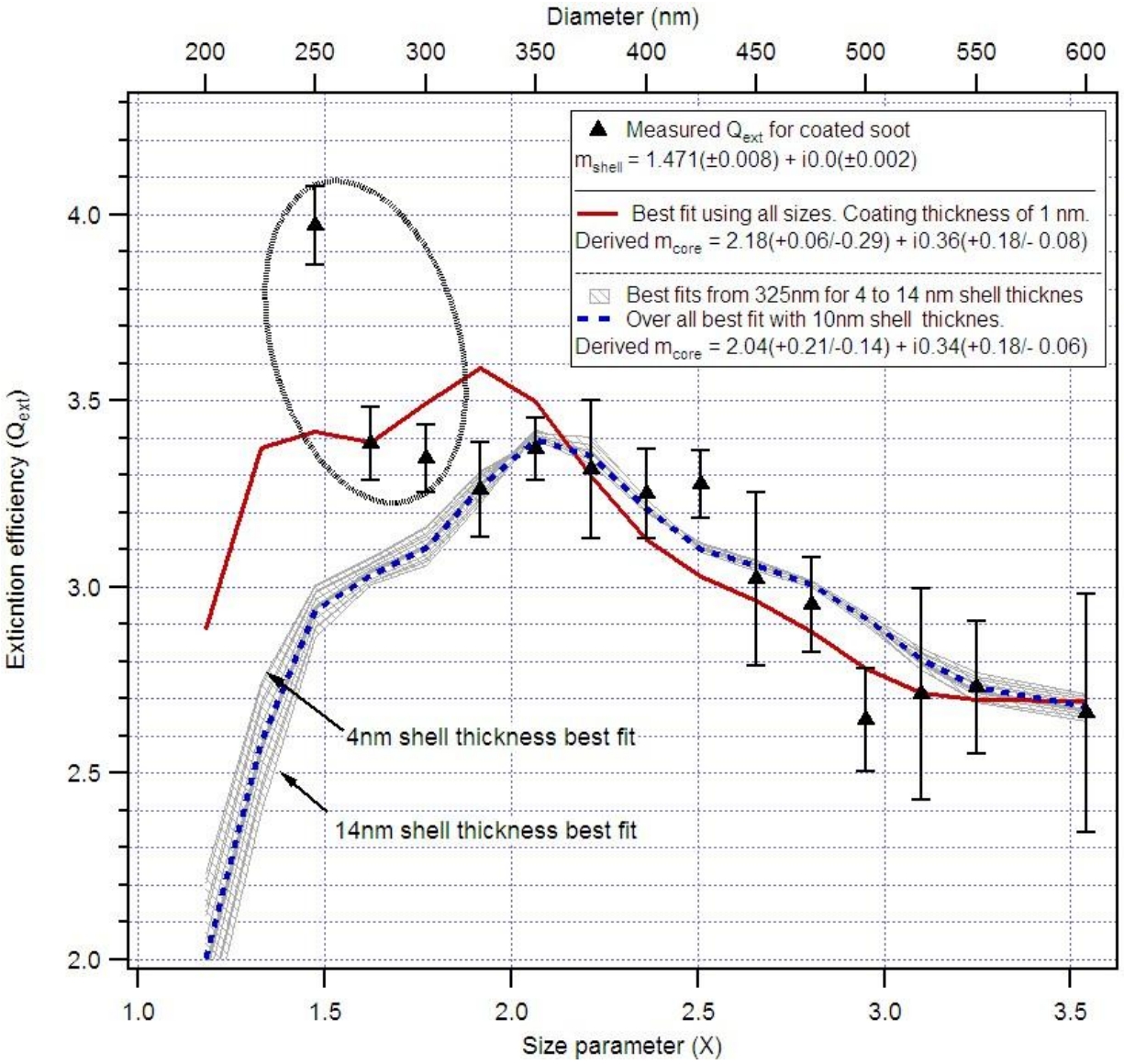

Figure 5.6 Extinction efficiency (Q_{ext}; triangles) as a function of size parameter (x) of soot coated with SOA-αO_3. The red solid curves represent the Mie best fits obtained by fitting all the experimental data points, with 1-3 nm as the best coatings thicknesses and m=2.18+i0.36 as the best RI. An RI of m=2.04+i0.34 with a 10nm coating (dotted blue line) was obtained by fitting only a subset of sizes starting from 325 nm (the excluded sizes are enclosed by the circle). The shaded area represents the best fits for all accepted coating thicknesses. The error bars represent the error from the average of extinction measurements sampled every 10 seconds for 2 minutes.

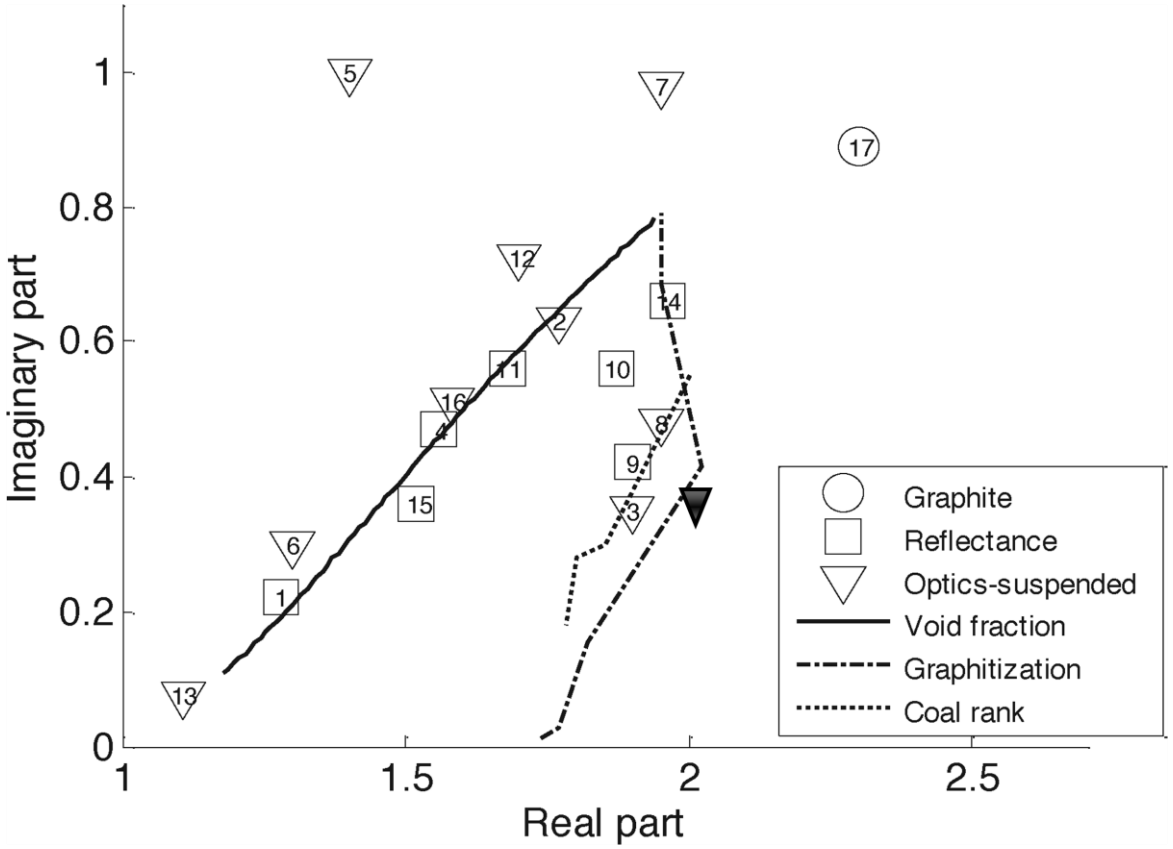

Figure 5.7 Refractive indices for light absorbing carbon (LAC). The black inverted triangle shows the RI derived in this study. The curve marked "void fraction" assumes that LAC has a single refractive index and that variation can be expressed by the Bruggeman effective-medium theory. The curve marked "graphitization" shows variations in the refractive index of carbon containing different sp2-bond content. Taken from Bond and Bergstrom (2006)[22]. See their publication for further explanation.

5.4 Summary and conclusions

Soot aerosol particles from a Combustion Aerosol Standard were injected into the large aerosol chamber facility AIDA and coated with secondary organic aerosols generated by the ozonolysis of α-pinene. The optical properties of non absorbing SOA particles with strongly absorbing soot inclusions were measured with a cavity ring down spectrometer (CRD) and a photoacoustic sensor (PAS) at 532nm. Using a Mie model for homogenous and coated spheres, the refractive indices of the SOA and internally mixed soot particles with SOA were derived.

The single scattering albedo (SSA) for the homogenously nucleated secondary organic aerosol, formed by the ozonolysis of α-pinene (SOA-αO_3), was measured to be one; which is in accordance with the non-absorbing nature of SOA-αO_3. After injecting 25μg m^{-3} of soot, at a C/O = 0.29, the SSA for the externally mixed aerosols decreased to 0.69 (±0.02); a second injection of 25μg m^{-3} decrease the SSA further to a value of 0.50(±0.02).

The SSA for fresh fractal-like soot was measured to be 0.2 (±0.03), and after allowing the soot to coagulate for 28 hours and coating it with SOA-αO_3 it increased to 0.71(±0.01). Furthermore, an absorption enhancement of the coated soot of up to 1.71 (±0.03) times from the non-coated coagulated soot was directly measured with the PAS.

Monodisperse measurements of SOA-αO_3 and soot coated with SOA-αO_3 were performed to derive the complex refractive index of both aerosols. A complex refractive index of m = 1.471(±0.008) + i0.0(±0.002) for the SOA-αO_3 was retrieved. For the compact coagulated soot a preliminary complex refractive index of m = 2.04(+0.21/-0.14) + i0.34(+0.18/-0.06) with 10nm(+4/-6) coating thickness was retrieved. Many uncertainties still need to be resolved to provide a certain value of the RI of soot and to explore different modeling approaches of the optical properties measured. However, the values found in this study serve as a firm basis for a comprehensive parameterization of the optical properties.

6 Overall summary and conclusions

Four different laboratory studies related to the optical properties of absorbing aerosols were presented in this dissertation.

In the first study (Chapter 2), a photoacoustic sensor (PAS) was fully characterized for measuring absorption by aerosols. It has an average sensitivity of $1.15 Mm^{-1}$, and $0.18 Mm^{-1}$ for a 1 second and 30 second integration time, respectively. The instrument was initially calibrated using ozone and a cavity ring down spectrometer (CRD). This calibration method was independently validated by measuring different sizes of nigrosine dye, calculating their optical absorption cross-section, and comparing them to the predicted cross-sections using Mie theory.

Furthermore, the photoacoustic sensor was used to characterize absorbing polystyrene latex spheres (APSL). The measured optical absorption cross-sections were compared to the results from Lack *et al*. (2006)[87] for the same batch of APSLs, and very good agreement was found between both measurements. This suggests APSLs can be a potential calibration standard for aerosol absorption instruments.

Finally, a simple algorithm was developed to calculate the PAS cell constant using a mixture of nigrosine and ammonium sulfate solutions. It was shown that if the complex refractive index of a highly or lightly absorbing substance is known, the PAS can be independently calibrated without the use of a CRD, or an absorbing gas.

The second study (Chapter 3), a simple approach to retrieve the effective broadband refractive index ($m_{broad,eff}$) in the visible range by matching the optical diameters measured by a white light optical particle counter (OPC) with the mobility diameters of a differential mobility analyzer was developed. This is the first time, to my knowledge, that such a method was applied to obtain refractive indices (RIs) of lightly absorbing (SRFA and the AS:nigrosine 10:1 mixture) and highly absorbing substances (nigrosine and its various mixtures with AS and GA).

Generally, the real part of the $m_{broad,eff}$ for all substances was retrieved successfully with a difference less than 8% from literature values. For absorbing substances, with the exception of AS:N 2:1 ratio, the obtained imaginary part is in good agreement with the expected values, and well within the measurement of other instruments, such as continuous wave and pulsed CRD spectroscopy.

With this new approach, the OPC can be used (with the caveat of the counting efficiency) to measure and analyze data and retrieve the complex $m_{broad,eff}$ for substances with a wide range of optical properties; from pure scatterers, for which the retrieval method is most accurate, up to highly absorbing ones, such as nigrosine. I expect that for substances with greater imaginary parts than nigrosine, such as soot, the RI retrieval will be less accurate. Using this approach, it is easy to obtain accurate calibration curves for data analysis and correct the measured sizes of white light OPCs to agree with the mobility diameters, i.e.

applying the retrieved calibration curve provides a corrected size distribution. This approach can substantially improve aerosol size distributions measured by OPCs in field measurements.

Finally, the calibration curves generated by this method were used to modify measured optical size distributions and align them with those of an SMPS to measure biomass burning aerosols, and by doing so, the effective broadband refractive index was derived. The average $m_{broad,eff}$ for a mixed population of aerosols dominated by open fires was $m_{broad,eff}=1.53(\pm0.03)+0.07i(\pm0.03)$, during the smoldering phase of the fires the effective broadband refractive index was found to be $m_{broad,eff}=1.54(\pm0.01)+0.04i(\pm0.01)$, compared to $m_{broad,eff}=1.49(\pm0.01)+0.02i(\pm0.01)$ of the aged aerosols measured the day following of the burning event.

The third study (Chapter 4), the validity of the volume weighted mixing rule at 355 nm and 532 nm was investigated. It was found that the difference between the derived and calculated real parts of the complex RIs were less than 5.3% for all substances, wavelengths, and RHs. The obtained imaginary parts for the retrieved and calculated RIs were in good agreement with each other, and well within the measurement errors of retrieval from pulsed CRD spectroscopy measurements. There were some cases with high percent differences, but those were attributed to a non homogeneous mixing for substances with low hygroscopic growth factors (GF) such as IHSS Pahokee peat and nigrosine.

For the low GF substances, the difference between assuming a core-shell structure or a homogenously mixed particle could have a significant effect on the calculated RI value was explored. It was found that at 80% RH and for size parameters less than 2.5, there is less than a 5 % difference between the extinction efficiencies calculated with a core-shell model and a homogenous mixture model. This difference is within measurement errors; hence, there is no significant difference between the models in this case. However, for greater size parameters the difference can be up to 10%. For 90% RH the differences below a size parameter of 2.5 were up to 7%.

Finally, the dependence of light extinction on RH for water soluble substances with different degrees of absorption was explored at two wavelengths, λ= 355 nm and 532 nm. It was found that the optical growth, $f\mathrm{RH}_{ext}$(%RH,Dry), dependence on size changes from having an exponential dependence for purely scattering substances to demonstrating practically no dependence for absorbing substances with an imaginary part greater than zero. There is no clear evidence for the effect of the ratio of the humidified extinction efficiency to the dry extinction efficiency on the behavior of $f\mathrm{RH}_{ext}$(%RH,Dry). However, by analyzing two substances with the same GF, information on the influence of the imaginary part on $f\mathrm{RH}_{ext}$(%RH,Dry) was obtained. At 532 nm absorption decreased the magnitude of $f\mathrm{RH}_{ext}$(%RH,Dry) for diameters less than 450 nm and increased the magnitude for greater sizes. At 355 nm, with the exception of 200 nm particles, the magnitude of $f\mathrm{RH}_{ext}$(%RH,Dry) increased with size. It is premature to parameterize the dependence of $f\mathrm{RH}_{ext}$(%RH,Dry) on

absorption, as more measurements are needed to quantify the influence of the $Q_{ext-\%RH}$ / $Q_{ext-Dry}$ factor on the behavior of $f\mathrm{RH}_{\mathrm{ext}}$(%RH,Dry) with size.

The measurements performed demonstrated that the volume weighted mixing rule is a good approximation for water soluble absorbing substances under 80% and 90% relative humidity conditions, and will be used as a basis to investigate how the twilight zone of warm clouds would change if aerosols with different degrees of absorption, from purely scattering to highly absorbing, are present.

In the last study presented in this dissertation, results of two soot aerosols simulation experiments conducted at the large aerosol chamber facility AIDA of the Karlsruhe Institute of Technology, Karlsruhe, Germany, were presented. Soot aerosol particles from a Combustion Aerosol Standard were injected into the large aerosol chamber facility AIDA and coated with secondary organic aerosols generated by the ozonolysis of α-pinene. The optical properties of non absorbing SOA particles with strongly absorbing soot inclusions were measured with a cavity ring down spectrometer and a photoacoustic sensor at 532nm. Using a Mie model for homogenous and coated spheres, the refractive indices of the SOA and internally mixed soot particles with SOA were derived.

The single scattering albedo (SSA) for the homogenously nucleated secondary organic aerosol, formed by the ozonolysis of α-pinene (SOA-αO_3), was measured to be one, after injecting 25μg m^{-3} of soot, at a C/O = 0.29, the SSA for the externally mixed aerosols decreased to 0.69 (±0.02); a second injection of 25μg m^{-3} decrease the SSA further to a value of 0.50(±0.02).

The SSA for fresh fractal-like soot was measured to be 0.2 (±0.03), and after allowing the soot to coagulate for 28 hours and coating it with SOA-αO_3 it increased to 0.71(±0.01). Furthermore, an absorption enhancement of the coated soot of up to 1.71 (±0.03) times from the non-coated coagulated soot was directly measured with the PAS.

Monodisperse measurements of SOA-αO_3 and soot coated with SOA-αO_3 were performed to derive the complex refractive index of both aerosols. A complex refractive index of m = 1.471(±0.008) + i0.0(±0.002) for the SOA-αO_3 was retrieved. For the compact coagulated soot a preliminary complex refractive index of m = 2.04(+0.21/-0.14) + i0.34(+0.18/-0.06) with 10nm(+4/-6) coating thickness was retrieved. Many uncertainties still need to be resolved to provide a certain value of the RI of soot and to explore different modeling approaches of the optical properties measured. However, the values found in this study serve as a firm basis for a comprehensive parameterization of the optical properties.

7 Recommendations for future work

There are still many open questions on the optical properties of absorbing aerosols. Here I would like to propose a few experiments that can help close the gaps in our knowledge. First, I propose a simple experiment to use the fully characterized photoacoustic spectrometer (PAS) in conjunction with a cavity ring down spectrometer (with the tandem setup used in chapter 2, 3, and 5) to derive the complex refractive index of aerosols with the measurement of only one diameter. This can help assess the chemical changes occurring in the aerosol and can give modelers changes in the RI over time to improve climate models.

Figure 7.1a shows the extinction coefficient (Q_{ext}) vs. size parameter for five different groups of complex refractive indices where the real part of the RI is kept constant, and the imaginary part is varied from k=0 to k=0.2 in k=0.05 steps for every real part. The dotted squares marks the diameter range where every real part of the complex RI can be distinguished regardless of the imaginary part, there is only a slight overlap between the real part n=1.4 and n=1.3. By choosing a size parameter of x=2.25, using the particle generation system described in Appendix I, and measuring the extinction coefficient with the cavity ring down spectrometer, the real part of the RI can be unequivocally measured. Furthermore, the imaginary part of the RI can be similarly measured with the photoacoustic spectrometer. Figure 7.1b shows the absorption coefficient vs. size parameter for four different groups of complex refractive indices where the imaginary part of the RI is kept constant, and the real part is varied from n=1.3 to n=1.7 in n=0.1 steps for every imaginary part. As in Figure 7.1a the dotted square marks the region where imaginary part will have to be distinguished from the real part measured from the CRD. In this region there is a clear distinction among the imaginary parts, with a slight overlap in the region between k=0.15 and k=0.2. However, the real part measured with the CRD will help distinguish the imaginary part. The error of the derivation is expected to be the same as the error in the CRD and PAS instruments; less than 5%. With only the need to measure one diameter to derive the complex refractive index, the instrument setup DMA-CRD-PAS can be taken to the field and time series of the RI can be measured.

Next, aerosol particles as they are transported through the atmosphere interact with existing gases which leads to products with new chemical and physical properties (normally referred to as aging). Aging of aerosols can change their molecular weight (MW), the new products can have higher oxidation states, which will therefore modify the hygroscopicity, and change the optical properties. Hence, to better model aerosols' processes in the atmosphere, investigating the effect of atmospheric condensed-phase reactions is of great importance. Some of the research questions where the CRD and the PAS can be used in the laboratory to better assess the optical properties of aerosols in these reactions are:

- How does the condensation of volatile organic compounds reacted with NO_x on non-reactive aerosols will change the optical properties of the seed aerosol?

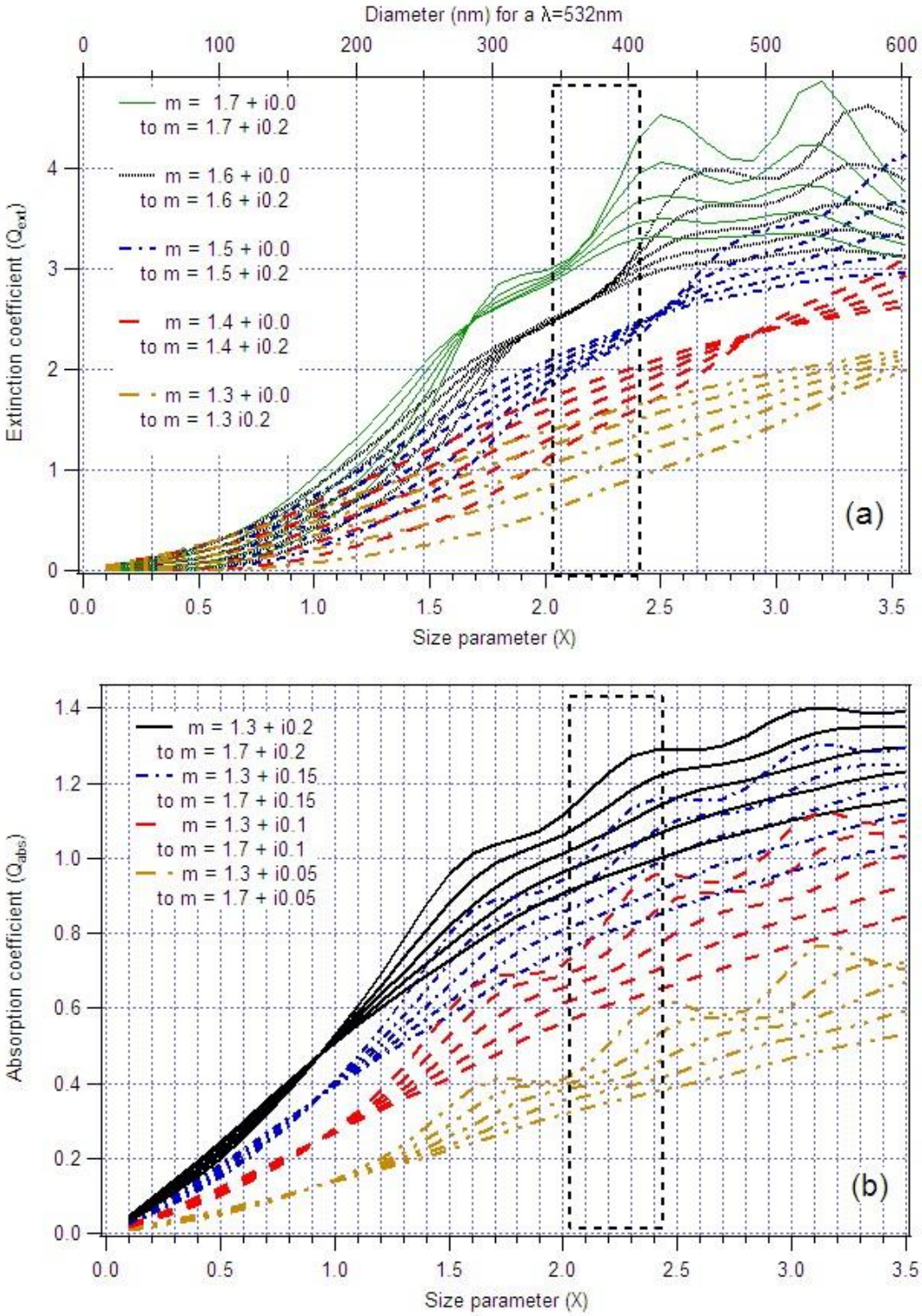

Figure 7.1 (a) Extinction coefficient vs size parameter for five different groups of complex refractive indices keeping the real part of the RI constant at n=1.7 (solid green line), n=1.6 (dotted black line), n=1.5 (blue dash-dot line), n=1.4 (red dash line), and n=1.3 (orange dash-dot-dot line), and varying the imaginary part from k=i0.0 to k=i0.2 for each real part. (b) Absorption coefficient vs size parameter for four different groups of RIs keeping the imaginary part constant at k=i0.2 (solid balck line), k=i0.15 (blue dash-dot line), k=i0.1 (red dash line), and k=0.05 (orange dash-dot-dot line), and varying the real part from n=1.3 to n=1.7. The dotted squares are the proposed areas to perform a single size measurement to derive the complex refractive index.

- How does the condensation of volatile organic compounds reacted with O_3 on non-reactive aerosols will change the optical properties of the seed aerosol?

Lastly, I would like to propose the development of a new instrument using a white light source. Using the design of the WELAS, instead of having a photomultiplier to measure the total intensity of the scattered light, a CCD camera can be placed instead to measure the scattering spectrum of single particles. This can give information on what wavelengths are being absorbed and what is the change in the scattering pattern for different carbonaceous particles.

8 Appendix I

8.1 Particle generation system

A schematic of the particle generation system is shown in Figure 8.1. Aqueous solutions (20–1000 mg L^{-1}) of the pure compounds or mixtures of interest are nebulized using a TSI constant output atomizer (TSI-3076, 35 psi, 2.5 standard liters per minute (SLM) flow), with dry particle-free pure nitrogen, generating a polydisperse distribution of droplets. An external pump is used to control the polydisperse aerosol flow which will be size selected. The aerosol flow enters silica gel column dryers to produce a dry flow (relative humidity (RH) of ~3%). Next, the dry polydisperse aerosol passes through a neutralizer (TSI 3012A) to obtain an equilibrium charge distribution on the particles. The charged particles then enter an electrostatic classifier (differential mobility analyzer (DMA TSI model 308100)), and a size selected, nearly monodisperse aerosol is selected at a fix applied voltage. The DMA operates with 5–3 SLM dry, clean nitrogen sheath flow. The maximum diameters that can be selected are 500 nm and 800 nm for 5 SLM and 3 SLM sheath flows, respectively. The aerosol concentration is controlled by the solution concentration with no upper limit for atmospherically relevant concentrations.

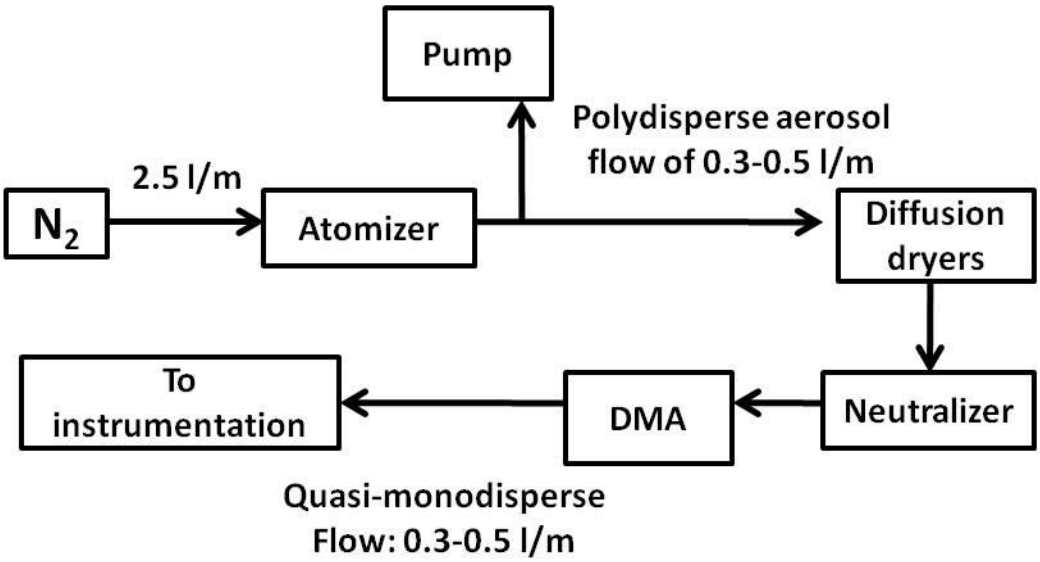

Figure 8.1Schematic of the quasi-monodisperse particle generation system

8.2 Derivation of the complex refractive index using cavity ring down spectroscopy

To retrieve the complex refractive index of a substance in the aerosol phase, the extinction efficiency (Q_{ext}) is measured at different diameters. The measured Q_{ext} values are fitted to Mie curves of different complex refractive indices, and the curve that best fits the measured data is determined to be the complex refractive index of the substance measured. To perform this calculation, equation 8.1 is used:

$$\chi^2(n,k) = \sum_{i=1}^{N} \frac{\left(Q_{ext\ measured} - Q_{ext_{(n,k)}}\right)_i^2}{\varepsilon_i^2} \qquad (8.1)$$

where N is number of diameters measured, ε is the estimated error in the measurement (taken as the standard deviation of repeated measurements of the same particle size with different concentrations), and *n* and *k* are the real and imaginary parts of the complex refractive index, respectively.

For example, to derive the complex refractive index for nigrosine, measurements of Q_{ext} at different diameters were performed (shown as the black squares in Figure 8.2).

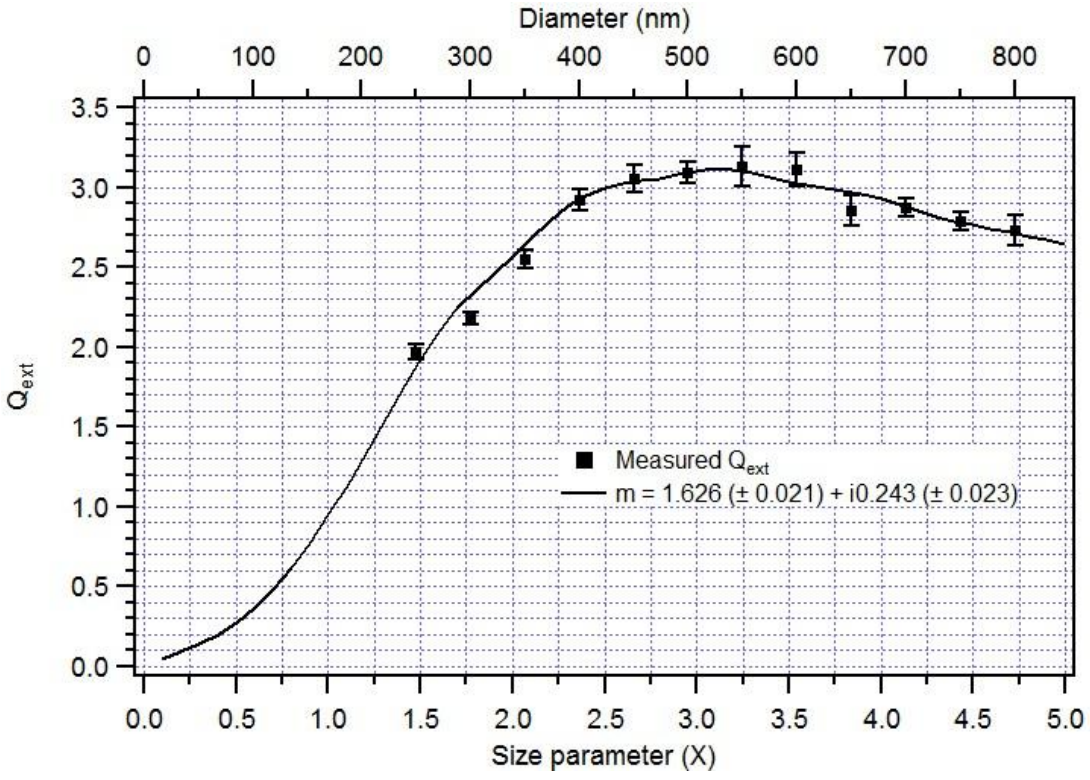

Figure 8.2. Measured Qext vs diameter for nigrosine dye at 532nm (solid squares). The solid line is the best Mie curve for the measured data, and it represents a complex refractive index of m = 1.626 (±0.021) + i0.243 (±0.023).

The obtained Q_{ext} values were used in equation 8.1 to calculate χ^2 while varying n and k values. The set of *n* and *k* values that minimize equation 8.1 represent the real and imaginary part of the complex refractive index of nigrosine. Figure 8.3 shows an example of the search for the minimum χ^2 value for the measured points shown in Figure A.1. The real part of the refractive index was allowed to vary from $n = 1.3$ to $n = 1.8$, and the imaginary part from $k = 0$ to $k = 0.8$, in steps of 0.001.

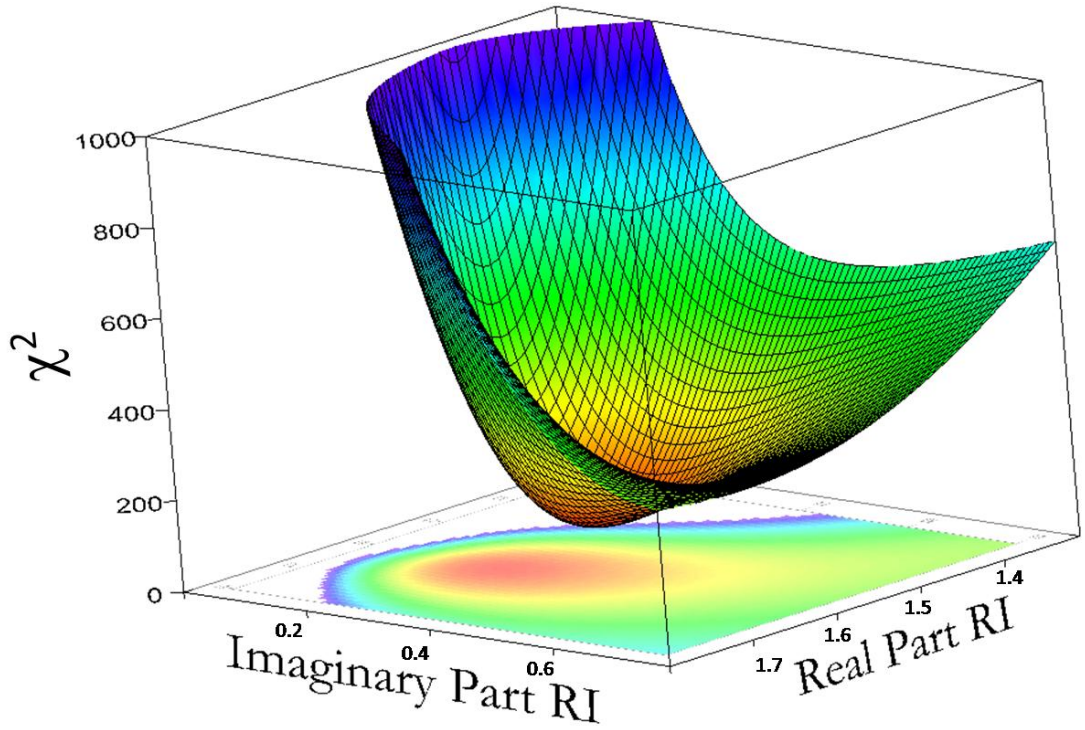

Figure 8.3. Calculation of χ^2 for different values of the complex refractive index. The real part was allowed to vary from *n*=1.3 to *n*=1.8, and the imaginary part from *k*=0 to *k*=0.8. The red area shows where the minimum value of exists.

The minimum χ^2 found for this experiment was $\chi^2_{min} = 18.86$. Assuming the errors of the measurement ε_i^2 to be normally distributed in the *n*-*k* space, the values of χ^2 for different calculations of equation A.1 follow a χ^2 distribution. The quintile for the 68.3% (1σ) confidence level for two degrees of freedom is 2.298. Any *n* and *k* values which yield a χ^2 that falls within the 1σ error bound of the best measurement is considered acceptable if $\chi^2 < \chi^2_{min} + 2.298$ (marked as the red area in Figure A.2).

9 Curriculum vitae

9.1 Education

Max Planck Institute for Chemistry & Institute for Atmospheric Physics, Johannes-Gutenberg-University, Mainz, Germany — Jul 07 – present
- PhD Atmospheric Physics
  Thesis project: Laboratory study of the optical properties of absorbing atmospheric aerosols and field applications.
  Estimated graduation date: September 2011

Weizmann Institute of Science, Department of Environmental Sciences and Energy Research, Rehovot, Israel. — Jul 09 – Oct 10
- Research collaboration with Prof. Yinon Rudich

Universidad Nacional Autónoma de México, México — Jan 05 – Jun 07
- M.S., Atmospheric Physics
  Thesis title: Microphysical characterization and radiative implications of sub-visual cirrus and contrails in the tropical tropopause.

The Pennsylvania State University, PA, U. S. A. — Aug 99 – May 04
- B.S. in Physics
- B.S. in Mathematics
- Minor in French.

Université Louis Pasteur, Strasbourg, France — Sept 02 – Jul 03
- Exchange program for physics students

9.2 Field Project Experience

SOOT-11 Project, AIDA chamber, Karlsruhe, Germany — Nov 10
- Participated in the project to measure the optical evolution of soot at different C/O ratios and when coated with SOA with a cavity ring down spectrometer and a photoacoustic sensor.

Amazonian Aerosol Characterization Experiment (AMAZE-08) Manaus, Brazil — Jan 08
- Took part in the research of the optical, chemical and physical properties of the ambient biogenic aerosol of the Amazonian forest in Brazil, and was responsible for the measurements with a White Light Aerosol Spectrometer.

Aircraft Towed Sensor Shuttle, University Mainz, Hohn, Germany — Sept 07
- Assisted the quality assurance of measurements, calibration and proper functionality of the Cloud Imaging Probe, the FSSP 300, and FSSP 100 during the first measurements with the AIRcraft TOwed Sensor Shuttle (AIRTOSS)

Costa Rica Aura Validation Experiment, NASA, San José, Costa Rica Jan 06
- Participated in a project investigating the microphysical properties of high altitude " sub-visible" cirrus cloud with a cloud, aerosol and precipitation spectrometer (CAPS).

Pre – AVE Water Isotope project, NASA Ellington field, U.S.A. Jul 05
- Preparation project for CR-AVE, where I Analyzed data from several research flights to check the performance of the CAPS.
- Participated in the setup and calibration of the CAPS in the WB-57F aircraft.

9.3 Publications

Flores, J.M., Bluvshtein, N., Abo-Riziq, A., Borrmann, S., Rudich, Y., Relative humidity dependence of light extinction of absorbing aerosols, 2011. In Preparation

Trainic, M., Riziq, A. A., Lavi, A., **Flores, J. M.**, and Rudich, Y.: The optical, physical and chemical properties of the products of glyoxal uptake on ammonium sulfate seed aerosols, Atmos. Chem. Phys. Discuss., 11, 19223-19252, doi:10.5194/acpd-11-19223-2011, 2011.

Lu, J.W., **Flores, J.M.**, Lavi, A., Abo-Riziq, A., Rudich, Y., Changes in the optical properties of Benzo[a]pyrene-coated aerosols with heterogeneous reactions with NO_2 and NO_3, Physical Chemistry Chemical Physics, 2011.

Adler, G., **Flores, J.M.**, Abo-Riziq, A., Borrmann, S., Rudich, Y., Chemical, physical, and optical evolution of biomass burning aerosols: a case study. Atmos. Chem. Phys., 2010.

Flores, J.M., Trainic, M., Borrmann, S., Rudich, Y., Effective broadband refractive index retrieval by a white light optical particle counter. Physical Chemistry Chemical Physics, **11**, 7943-7950, 2009.

9.4 Conference Proceedings

Flores, J. M., Bluvshtein, N., Abo-Riziq, A., Borrmann, S., Rudich, Y., Interaction of absorbing aerosols with high relative humidity, is the volume weighted mixing rule valid? Gordon research conference-Atmospheric chemistry. Poster presentation

Flores, J.M., Schnaiter, M., Laborde, M., Taylor, J., Linke, C., Saathoff, H., Gysel, M., Abo-Riziq, A., Rudich, Y., Optical evolution of pure black carbon and internally mixed with secondary organic aerosol, 2011. 10th International Conference on Carbonaceous Particles in the Atmosphere. Poster presentation.

Flores, J.M., Trainic, M., Borrmann, S., Rudich, Y., Effective broadband refractive index retrieval by a white light optical particle counter, INTROP Final Conference – Tropospheric Chemistry, 2009. Poster presentation.

Flores, J.M., AMAZE-08 White light aerosol spectrometer preliminary data, International Workshop: Aerosols in the Amazon - Changes and their Consequences from Past and Future Human Activities, February 18 - 22, 2008

Flores, J. M., Baumgardner,D., Kok, G., Raga, G., Hermann R., Tropical sub – visual cirrus and contrails at -85°C , 12th Conference on Cloud Physics *American Meteorological Society,* 2006.

Flores, J. M., D. Baumgardner, G. Raga, Cirrus invisibles en regiones tropicales y estelas de avión a -85°C, XV Congreso mexicano de meteorología, 2006.

9.5 Awards

Accepted to the Atmospheric Chemistry Colloquium for Emerging Senior Scientist (ACCESS-XI) organized by the Gordon Research conference-Atmospheric chemistry. July 2011.

Alfonso Caso Medal nomination. Given to the best Master's thesis in the year. 2007

Button – Waller Scholarship, Penn State University, 2000, 2001, 2002, 2003.

John and Elizabeth Teas Scholarship, Penn State University, 2000, 2001, 2003.

10 References

1. Murphy, D.M., D.S. Thomson, and M.J. Mahoney, *In Situ Measurements of Organics, Meteoritic Material, Mercury, and Other Elements in Aerosols at 5 to 19 Kilometers.* Science, 1998. 282(5394): p. 1664-1669.
2. Albrecht, B.A., *Aerosols, Cloud Microphysics, and Fractional Cloudiness.* Science, 1989. 245(4923): p. 1227-30.
3. Twomey, S.A., *The influence of pollution on the shortwave albedo of clouds.* J. Atmos. Sci., 1977. 34: p. 1149-1152.
4. Rosenfeld, D., *Suppression of Rain and Snow by Urban and Industrial Air Pollution.* Science, 2000. 287(5459): p. 1793-1796.
5. Ackerman AS, T.O., Stevens DE, Heymsfield AJ, Ramanathan V, Welton EJ. , *Reduction of tropical cloudiness by soot.* Science, 2000. 288: p. 1042-1047.
6. IPCC, *Climate Change 2007: The Physical Science Basis. Contribution of Working Group I to the Fourth Assessment Report of the Intergovernmental Panel on Climate Change* ed. S. Solomon, D. Qin, M. Manning, Z. Chen, M. Marquis, K.B. Averyt, M.Tignor and H.L. Miller 2007, Cambridge, United Kingdom and New York, NY, USA.
   : Cambridge University Press.
7. Schwartz, S.E. and P.R. Buseck, *Absorbing Phenomena.* Science, 2000. 288(5468): p. 989-990.
8. Streets, D.G., Y. Wu, and M. Chin, *Two-decadal aerosol trends as a likely explanation of the global dimming/brightening transition.* Geophys. Res. Lett., 2006. 33(15): p. L15806.
9. Tripathi, S.N., et al., *Aerosol black carbon radiative forcing at an industrial city in northern India.* Geophys. Res. Lett., 2005. 32(8): p. L08802.
10. Moosmuller, H., R.K. Chakrabarty, and W.P. Arnott, *Aerosol light absorption and its measurement: A review.* Journal of Quantitative Spectroscopy & Radiative Transfer, 2009. 110(11): p. 844-878.
11. Warren, S.G., *Optical properties of snow.* Rev. Geophys., 1982. 20(1): p. 67-89.
12. Warren, S.G. and W.J. Wiscombe, *Dirty snow after nuclear war.* Nature, 1985. 313(6002): p. 467-470.
13. Brandt, R.E., S.G. Warren, and A.D. Clarke, *A controlled snowmaking experiment testing the relation between black carbon content and reduction of snow albedo.* Journal of Geophysical Research-Atmospheres. 116: p. 6.
14. Chylek, P. and J. Wong, *Effect of absorbing aerosols on global radiation budget.* Geophys. Res. Lett., 1995. 22(8): p. 929-931.
15. Stier P., S.J.H., Kinne S., Boucher O. , *Aerosol absorption and radiative forcing.* Atmospheric Chemistry and Physics, 2007. 7: p. 5237-5261.
16. Hegg, D.A., et al., *Chemical apportionment of aerosol column optical depth off the mid-Atlantic coast of the United States.* J. Geophys. Res., 1997. 102(D21): p. 25293-25303.
17. Novakov, T., D.A. Hegg, and P.V. Hobbs, *Airborne measurements of carbonaceous aerosols on the East Coast of the United States.* J. Geophys. Res., 1997. 102(D25): p. 30023-30030.
18. Park, R.J., et al., *Export efficiency of black carbon aerosol in continental outflow: Global implications.* J. Geophys. Res., 2005. 110(D11): p. D11205.

19. Petzold, A., et al., *Perturbation of the European free troposphere aerosol by North American forest fire plumes during the ICARTT-ITOP experiment in summer 2004.* Atmos. Chem. Phys., 2007. 7(19): p. 5105-5127.
20. Reddy, M.S., et al., *Aerosol optical depths and direct radiative perturbations by species and source type.* Geophys. Res. Lett., 2005. 32(12): p. L12803.
21. Bond, T.C., et al., *A technology-based global inventory of black and organic carbon emissions from combustion.* J. Geophys. Res., 2004. 109(D14): p. D14203.
22. Bond, T.C. and R.W. Bergstrom, *Light Absorption by Carbonaceous Particles: An Investigative Review.* Aerosol Science and Technology, 2006. 40(1): p. 27 - 67.
23. Chakrabarty, R.K., et al., *Light scattering and absorption by fractal-like carbonaceous chain aggregates: comparison of theories and experiment.* Appl. Opt., 2007. 46(28): p. 6990-7006.
24. Liu, L., M.I. Mishchenko, and W. Patrick Arnott, *A study of radiative properties of fractal soot aggregates using the superposition T-matrix method.* Journal of Quantitative Spectroscopy and Radiative Transfer, 2008. 109(15): p. 2656-2663.
25. Sorensen, C.M., *Light scattering by fractal aggregates: A review.* Aerosol Science and Technology, 2001. 35(2): p. 648-687.
26. Andreae, M.O. and A. Gelencser, *Black carbon or brown carbon? The nature of light-absorbing carbonaceous aerosols.* Atmospheric Chemistry and Physics, 2006. 6: p. 3131-3148.
27. Sun, H.L., L. Biedermann, and T.C. Bond, *Color of brown carbon: A model for ultraviolet and visible light absorption by organic carbon aerosol.* Geophysical Research Letters, 2007. 34.
28. Hallquist, M., et al., *The formation, properties and impact of secondary organic aerosol: current and emerging issues.* Atmos. Chem. Phys., 2009. 9(14): p. 5155-5236.
29. Robinson, A.L., et al., *Rethinking Organic Aerosols: Semivolatile Emissions and Photochemical Aging.* Science, 2007. 315(5816): p. 1259-1262.
30. Turpin, B.J. and J.J. Huntzicker, *Identification of secondary organic aerosol episodes and quantitation of primary and secondary organic aerosol concentrations during SCAQS.* Atmospheric Environment, 1995. 29(23): p. 3527-3544.
31. Chughtai, A.R., et al., *Carbonaceous particle hydration.* Atmospheric Environment, 1999. 33(17): p. 2679-2687.
32. Petters, M.D., et al., *Chemical aging and the hydrophobic-to-hydrophilic conversion of carbonaceous aerosol.* Geophys. Res. Lett., 2006. 33(24): p. L24806.
33. Weingartner, E., H. Burtscher, and U. Baltensperger, *Hygroscopic properties of carbon and diesel soot particles.* Atmospheric Environment, 1997. 31(15): p. 2311-2327.
34. Huang, P.-F., et al., *Effects of water condensation and evaporation on diesel chain-agglomerate morphology.* Journal of Aerosol Science, 1994. 25(3): p. 447-459.
35. Schnaiter, M., et al., *Absorption amplification of black carbon internally mixed with secondary organic aerosol.* J. Geophys. Res., 2005. 110(D19): p. D19204.
36. Koren, I., et al., *On the twilight zone between clouds and aerosols.* Geophys. Res. Lett., 2007. 34(8): p. L08805.
37. Bohren C. F. and Huffman D. R., *Absorption and scattering of light by small particles*. 1983, New York: Wiley.
38. Liu, L., Wang, H., Yu, B., Xu, Y., Shem, J., *Improved algorithm of light scattering by a coated sphere.* China Particuology, 2007. 5(3): p. 230-236.
39. Satheesh SK, M.K., *Radiative effects of natural aerosols: a review.* Atmos Environ, 2005. 39: p. 2089-2110.

40. Koren, I.J., Martins, V., Remer, L. A., and Afargan, H., *Smoke invigoration versus inhibition of clouds over the amazon.* Science, 2008. 321: p. 946-949.
41. Mie G., *Beiträge zur Optiktrüber Medien,speziell kolloidaler Metallösungen.* Ann Phys, 1908. 330: p. 377-445.
42. Baumgardner, D., et al., *Refractive, indices of aerosols in the upper troposphere and lower stratosphere.* Geophysical Research Letters, 1996. 23(7): p. 749-752.
43. Bemer, D., J.F. Fabries, and A. Renoux, *Calculation Of The Theoretical Response Of An Optical-Particle Counter And Its Practical Usefulness.* Journal Of Aerosol Science, 1990. 21(5): p. 689-700.
44. Binnig, J., J. Meyer, and G. Kasper, *Calibration of an optical particle counter to provide PM2.5 mass for well-defined particle materials.* Journal Of Aerosol Science, 2007. 38(3): p. 325-332.
45. Chen, B.T., Y.S. Cheng, and H.C. Yeh, *Experimental Responses Of 2 Optical-Particle Counters.* Journal Of Aerosol Science, 1984. 15(4): p. 457-464.
46. Garvey, D.M. and R.G. Pinnick, *Response Characteristics Of The Particle Measuring Systems Active Scattering Aerosol Spectrometer Probe (Asasp-X).* Aerosol Science And Technology, 1983. 2(4): p. 477-488.
47. Gebhart, J., et al., *Intercomparison Of Optical-Particle Counters.* Staub Reinhaltung Der Luft, 1983. 43(11): p. 439-447.
48. Guyon, P., et al., *Refractive index of aerosol particles over the Amazon tropical forest during LBA-EUSTACH 1999.* Journal Of Aerosol Science, 2003. 34(7): p. 883-907.
49. Hand, J.L. and S.M. Kreidenweis, *A new method for retrieving particle refractive index and effective density from aerosol size distribution data.* Aerosol Science And Technology, 2002. 36(10): p. 1012-1026.
50. Heim, M., et al., *Performance evaluation of three optical particle counters with an efficient "multimodal" calibration method.* Journal Of Aerosol Science, 2008. 39(12): p. 1019-1031.
51. Kim, Y.J., *Response Of The Active Scattering Aerosol Spectrometer Probe (Asasp-100x) To Particles Of Different Chemical-Composition.* Aerosol Science And Technology, 1995. 22(1): p. 33-42.
52. Sachweh, B., et al., *In situ optical particle counter with improved coincidence error correction for number concentrations up to 10(7) particles cm(-3).* Journal Of Aerosol Science, 1998. 29(9): p. 1075-1086.
53. Snider, J.R. and M.D. Petters, *Optical particle counter measurement of marine aerosol hygroscopic growth.* Atmospheric Chemistry And Physics, 2008. 8(7): p. 1949-1962.
54. Stolzenburg, M., N. Kreisberg, and S. Hering, *Atmospheric size distributions measured by differential mobility optical particle size spectrometry.* Aerosol Science And Technology, 1998. 29(5): p. 402-418.
55. Umhauer, H., *Particle-Size Distribution Analysis By Scattered-Light Measurements Using An Optically Defined Measuring Volume.* Journal Of Aerosol Science, 1983. 14(6): p. 765-770.
56. Umhauer, H., S. Berbner, and G. Hemmer, *Optical in situ size and concentration measurement of particles dispersed in gases at temperatures up to 1000 degrees C.* Particle & Particle Systems Characterization, 2000. 17(1): p. 3-15.
57. Wen, H.Y. and G. Kasper, *Counting Efficiencies Of 6 Commercial Particle Counters.* Journal Of Aerosol Science, 1986. 17(6): p. 947-&.
58. Okeefe, A. and D.A.G. Deacon, *CAVITY RING-DOWN OPTICAL SPECTROMETER FOR ABSORPTION-MEASUREMENTS USING PULSED LASER SOURCES.* Review of Scientific Instruments, 1988. 59(12): p. 2544-2551.

59. Sappey, A.D., et al., *Fixed-frequency cavity ringdown diagnostic for atmospheric particulate matter.* Optics Letters, 1998. 23(12): p. 954-956.
60. Adler, G., et al., *Effect of intrinsic organic carbon on the optical properties of fresh diesel soot.* Proceedings of the National Academy of Sciences of the United States of America, 2009. 107(15): p. 6699-6704.
61. Brown, S.S., H. Stark, and A.R. Ravishankara, *Applicability of the steady state approximation to the interpretation of atmospheric observations of NO3 and N2O5.* Journal of Geophysical Research-Atmospheres, 2003. 108(D17).
62. Dinar, E., et al., *The complex refractive index of atmospheric and model humic-like substances (HULIS) retrieved by a cavity ring down aerosol spectrometer (CRD-AS).* Faraday Discussions, 2008. 137: p. 279-295.
63. Dube, W.P., et al., *Aircraft instrument for simultaneous, in situ measurement of NO3 and N2O5 via pulsed cavity ring-down spectroscopy.* Review of Scientific Instruments, 2006. 77(3).
64. Garland, R.M., et al., *Parameterization for the relative humidity dependence of light extinction: Organic-ammonium sulfate aerosol.* Journal of Geophysical Research-Atmospheres, 2007. 112(D19).
65. Lang-Yona, M., et al., *Complex Refractive Indices of Aerosols Retrieved by Continuous Wave-Cavity Ring Down Aerosol Spectrometer.* Analytical Chemistry, 2009. 81(5): p. 1762-1769.
66. Lang-Yona, N., et al., *Interaction of internally mixed aerosols with light.* Physical Chemistry Chemical Physics, 2009. 12(1): p. 21-31.
67. Lang-Yona, N., et al., *The chemical and microphysical properties of secondary organic aerosols from Holm Oak emissions.* Atmospheric Chemistry and Physics, 2010. 10(15): p. 7253-7265.
68. Moosmuller, H., R. Varma, and W.P. Arnott, *Cavity ring-down and cavity-enhanced detection techniques for the measurement of aerosol extinction.* Aerosol Science and Technology, 2005. 39(1): p. 30-39.
69. Osthoff, H.D., et al., *Measurement of atmospheric NO2 by pulsed cavity ring-down spectroscopy.* Journal of Geophysical Research-Atmospheres, 2006. 111(D12).
70. Pettersson, A., et al., *Measurement of aerosol optical extinction at 532nm with pulsed cavity ring down spectroscopy.* Journal Of Aerosol Science, 2004. 35(8): p. 995-1011.
71. Riziq, A.A., et al., *Optical properties of absorbing and non-absorbing aerosols retrieved by cavity ring down (CRD) spectroscopy.* Atmospheric Chemistry And Physics, 2007. 7(6): p. 1523-1536.
72. Riziq, A.A., et al., *Extinction efficiencies of coated absorbing aerosols measured by cavity ring down aerosol spectrometry.* Atmospheric Chemistry and Physics, 2008. 8(6): p. 1823-1833.
73. Spindler, C., A.A. Riziq, and Y. Rudich, *Retrieval of aerosol complex refractive index by combining cavity ring down aerosol spectrometer measurements with full size distribution information.* Aerosol Science and Technology, 2007. 41(11): p. 1011-1017.
74. Scherer, J.J.P., J.B.; O`Keefe, A.; Saykally, R.J.,, *Cavity Ringdown Laser Absorption Spectroscopy: History, Development, and Application to Pulsed Molecular Beams. Chem.Rev.*, 1997. 97: p. 25-51.
75. Wheeler, M.D.N., S.M.; Orr-Ewing, A.J.; Ashfold, M.N.R.,, *Cavity ring-down spectroscopy. J. Chem. Soc., Faraday Trans.*, 1998. 94(3): p. 337-351.
76. Busch, K.W., Busch, M.A.,, *Cavity-Ringdown Spectroscopy: An Ultratrace-Absorption Measurement Technique*. *ACS Symposium Series 720*. 1999, *Washington American Chemical Society*.

77. Berden, G.P., R.; Meijer, G.,, *Cavity ring-down spectroscopy: Experimental schemes and applications. Int. Reviews Phys. Chem.*, 2000. 19(4): p. 565-607.
78. Brown, S.S., *Absorption Spectroscopy in High-Finesse Cavities for Atmospheric Studies. Chem. Rev.*, 2003. 103: p. 5219-5238.
79. Brown, S.S., Stark, H., Ciciora, S. J., McLaughlin, R. J., and Ravishankara, A. R.,, *Simultaneous in situ detection of atmospheric no3 and n2o5 via cavity ring-down spectroscopy.* Rev. Sci. Inst., 2002. 73: p. 3291-3301.
80. Bruce CW, P.R., *In situ measurement of light absorption with a resonant CW laser spectrophone.* . Appl Opt, 1977. 16: p. 1762-1765.
81. Terhune RW, A.J., *Spectrophone measurements of the absorption of visible light by aerosols in the atmosphere.* . Opt Lett 1977. 1: p. 70-72.
82. Arnott, W.P., Moosmuller, H., Rogers, C.F., Jin, T., Bruch, R.,, *Photoacoustic spectrometer for measuring light absorption by aerosol: instrument description.* Atmos. Environ., 1999. 33: p. 2845-2852.
83. Chan CH., *Effective absorption for thermal blooming due to aerosols.* Appl Phys Lett, 1975. 26: p. 628-630.
84. Miklos, A., P. Hess, and Z. Bozoki, *Application of acoustic resonators in photoacoustic trace gas analysis and metrology.* Review of Scientific Instruments, 2001. 72(4): p. 1937-1955.
85. Meyer, P.L.S., M. W., *Atmospheric pollution monitoring using CO2-laser photoacoustic spectroscopy and other techniques.* Review of Scientific Instruments, 1990. 61(7): p. 1779-1807.
86. Schäfer S., M.A., and Hess P, , *Quantitative signal analysis in pulsed resonant photoacoustics.* Appl. Opt, 1997. 36: p. 3202-3211.
87. Lack, D.A., et al., *Aerosol Absorption Measurement using Photoacoustic Spectroscopy: Sensitivity, Calibration, and Uncertainty Developments.* Aerosol Science and Technology, 2006. 40(9): p. 697 - 708.
88. Arnott, W.P., Walker, J. W., Moosmuller, H., Elleman, R. A., Jonsson, H. H., Buzorious, G., Conant, W. C., Flagan, R. C., and Seinfeld, J. H.,, *Photacoustic Insight for Aerosol Light Absorption Aloft from Meterological Aircraft and Comparison with Particle Soot Absorption Photometer Measurements: DOE Southern Great Plains Climate Research Facility and the Coastal Stratocumulus Imposed Perturbation Experiments,*. J. Geophys. Res., 2006. 111: p. D05S02.
89. Bond, T.C., Anderson, T. L., and Campbell, D.,, *Calibration and Intercomparison of Filter-Based Measurements of Visible Light Absorption by Aerosols. Aerosol Sci. Technol*, 1999. 30(6): p. 582.
90. Flores, J.M., et al., *Effective broadband refractive index retrieval by a white light optical particle counter*. Physical Chemistry Chemical Physics, 2009. 11(36): p. 7943-7950.
91. Press, W.H., et al., *Numerical recipes in c, the art of scientific computer, 2nd edition*. 1992, New York: Cambridge University Press.
92. Erlick, C., *Effective refractive indices of water and sulfate drops containing absorbing inclusions.* Journal of the Atmospheric Sciences, 2006. 63(2): p. 754-763.
93. G. A. d'Almeida, P.K.a.E.P.S., *Atmospheric Aerosols: Global Climatology and Radiative Characteristics (Studies in Geophysical Optics and Remote Sensing)*. 1991, Hampton: A Deepak Pub.
94. Pettersson, A., Lovejoy, E. R., Brock, C. A., Brown, S. S., and Ravishankara, A. R., *Measurement of Aerosol Optical Extinction at 532 nm with Pulsed Cavity Ring Down Spectroscopy. J. Aerosol Sci.*, 2004. 35(8): p. 995.

95. Ramanathan, V., et al., *Atmospheric brown clouds: Impacts on South Asian climate and hydrological cycle.* Proceedings Of The National Academy Of Sciences Of The United States Of America, 2005. 102(15): p. 5326-5333.
96. Solomon, S., et al., *The Physical Science Basis. Contribution of Working Group I to the Fourth Assessment*
Report of the Intergovernmental Panel on Climate Change. 2007, Cambridge University Press: Cambridge, New York.
97. Koren, I., et al., *Measurement of the effect of Amazon smoke on inhibition of cloud formation.* Science, 2004. 303(5662): p. 1342-1345.
98. Bates, T.S., et al., *Aerosol direct radiative effects over the northwest Atlantic, northwest Pacific, and North Indian Oceans: estimates based on in-situ chemical and optical measurements and chemical transport modeling.* Atmospheric Chemistry And Physics, 2006. 6: p. 1657-1732.
99. Bellouin, N., et al., *Global estimate of aerosol direct radiative forcing from satellite measurements.* Nature, 2005. 438(7071): p. 1138-1141.
100. Kaufman, Y.J., et al., *The effect of smoke, dust, and pollution aerosol on shallow cloud development over the Atlantic Ocean.* Proceedings Of The National Academy Of Sciences Of The United States Of America, 2005. 102(32): p. 11207-11212.
101. Koren, I., et al., *Smoke invigoration versus inhibition of clouds over the Amazon.* Science, 2008. 321(5891): p. 946-949.
102. Rosenfeld, D., et al., *Flood or drought: How do aerosols affect precipitation?* Science, 2008. 321(5894): p. 1309-1313.
103. Kanakidou, M., *Aerosols in global models - Focus on Europe*, in *Regional Climate Variability And Its Impacts In The Mediterranean Area*. 2007. p. 143-154.
104. Kanakidou, M., S. Myriokefalitakis, and K. Tsigaridis, *Global Modelling Of Secondary Organic Aerosol (Soa) Formation: Knowledge And Challenges*, in *Simulation And Assessment Of Chemical Processes In A Multiphase Environment*. 2008. p. 149-165.
105. Hansen, J., et al., *Efficacy of climate forcings.* Journal Of Geophysical Research-Atmospheres, 2005. 110(D18).
106. Jacobson, M.Z., *Global direct radiative forcing due to multicomponent anthropogenic and natural aerosols.* Journal Of Geophysical Research-Atmospheres, 2001. 106(D2): p. 1551-1568.
107. Menon, S., et al., *Climate effects of black carbon aerosols in China and India.* Science, 2002. 297(5590): p. 2250-2253.
108. Ramanathan, V. and Y. Feng, *Air pollution, greenhouse gases and climate change: Global and regional perspectives.* Atmospheric Environment, 2009. 43(1): p. 37-50.
109. Koren, I., et al., *Aerosol invigoration and restructuring of Atlantic convective clouds.* Geophysical Research Letters, 2005. 32(14).
110. Anderson, T.L., et al., *Performance characteristics of a high-sensitivity, three-wavelength, total scatter/backscatter nephelometer.* Journal of Atmospheric and Oceanic Technology, 1996. 13(5): p. 967-986.
111. Anderson, T.L. and J.A. Ogren, *Determining aerosol radiative properties using the TSI 3563 integrating nephelometer.* Aerosol Science and Technology, 1998. 29(1): p. 57-69.
112. Arnott, W.P., et al., *Photoacoustic spectrometer for measuring light absorption by aerosol: instrument description.* Atmospheric Environment, 1999. 33(17): p. 2845-2852.
113. Arnott, W.P., et al., *Evaluation of 1047-nm photoacoustic instruments and photoelectric aerosol sensors in source-sampling of black carbon aerosol and*

particle-bound PAHs from gasoline and diesel powered vehicles. Environmental Science & Technology, 2005. 39(14): p. 5398-5406.
114. Lack, D.A., et al., *Aerosol absorption measurement using photoacoustic spectroscopy: Sensitivity, calibration, and uncertainty developments.* Aerosol Science And Technology, 2006. 40(9): p. 697-708.
115. Lang-Yona, N., et al., *Complex Refractive Indices of Aerosols Retrieved by Continuous Wave-Cavity Ring Down Aerosol Spectrometer.* Analytical Chemistry, 2009. 81(5): p. 1762-1769.
116. Liu, Y.G. and P.H. Daum, *The effect of refractive index on size distributions and light scattering coefficients derived from optical particle counters.* Journal Of Aerosol Science, 2000. 31(8): p. 945-957.
117. Pueschel, R.F., et al., *Calibration Correction Of An Active Scattering Spectrometer Probe To Account For Refractive-Index Of Stratospheric Aerosols - Comparison Of Results With Inertial Impaction.* Aerosol Science And Technology, 1990. 12(4): p. 992-1002.
118. Friehmelt, R. and S. Heidenreich, *Calibration of a white-light/90 degrees optical particle counter for "aerodynamic" size measurements-experiments and calculations for spherical particles and quartz dust.* Journal Of Aerosol Science, 1999. 30(10): p. 1271-1279.
119. Quinten, M., R. Friehmelt, and K.F. Ebert, *Sizing of aggregates of spheres by a white-light optical particle counter with 90 degrees scattering angle.* Journal Of Aerosol Science, 2001. 32(1): p. 63-72.
120. Baron, P., *Personal Aerosol Sampler Design: A Review.* Appl. Occup. Environ. Hyg., 1998. 13: p. 313-320.
121. Jacobson, M.Z., *Analysis of aerosol interactions with numerical techniques for solving coagulation, nucleation, condensation, dissolution, and reversible chemistry among multiple size distributions.* Journal Of Geophysical Research-Atmospheres, 2002. 107(D19).
122. Stelson, A.W., *Urban Aerosol Refractive-Index Prediction By Partial Molar Refraction Approach.* Environmental Science & Technology, 1990. 24(11): p. 1676-1679.
123. Tang, I.N., *Thermodynamic and optical properties of mixed-salt aerosols of atmospheric importance.* Journal Of Geophysical Research-Atmospheres, 1997. 102(D2): p. 1883-1893.
124. Born, M. and E. Wolf, *Principles of Optics*. 7th ed. 1999: Cambridge University Press.
125. d'Almeida, G.A., P. Koepke, and E.P. Shettle, *Atmospheric aerosols, global climatology and radiative characteristics*. 1991, Hampton: A. Deepak Publishing. 561.
126. Bohren, C.F. and D.R. Huffman, *Absorption and scattering of light by small particles* 1983: Wiley. 530.
127. Chylek, P., V. Ramaswamy, and R.J. Cheng, *Effect Of Graphitic Carbon On The Albedo Of Clouds.* Journal Of The Atmospheric Sciences, 1984. 41(21): p. 3076-3084.
128. Covert, D.S., J. Heintzenberg, and H.C. Hansson, *Electrooptical Detection Of External Mixtures In Aerosols.* Aerosol Science And Technology, 1990. 12(2): p. 446-456.
129. Hering, S.V. and P.H. McMurry, *Optical Counter Response To Monodisperse Atmospheric Aerosols.* Atmospheric Environment Part A-General Topics, 1991. 25(2): p. 463-468.

130. von der Weiden, S.L., F. Drewnick, and S. Borrmann, *Particle Loss Calculator - a new software tool for the assessment of the performance of aerosol inlet systems.* Atmospheric Measurement Techniques, 2009. 2(2): p. 479-494.
131. Adler, G., Flores, J. M., Abo Riziq, A., Borrmann, S., and Rudich, Y., , *Chemical, physical, and optical evolution of biomass burning aerosols: a case study.* Atmos. Chem. Phys. , 2011.
132. Yamasoe, M.A., Kaufman, Y. J., Dubovik, O., Remer, L. A., Holben, B. N., and Artaxo, P. , *Retrieval of the real part of the refractive index of smoke particles from Sun/sky measurements during SCAR-B.* J. Geophys. Res.-Atmos., 1998. 103: p. 31893-31902.
133. Wandinger, U., Muller, D., Bockmann, C., Althausen, D., Matthias, V., Bosenberg, J., Weiss, V., Fiebig, M., Wendisch, M., Stohl, A., and Ansmann, A., *Optical and micro physical characterization of biomass-burning and industrial-pollution aerosols from multiwavelength lidar and aircraft measurements.* J. Geophys. Res.-Atmos., 2002. 107(D21): p. 8125.
134. Hand, J.L., Day, D. E., McMeeking, G. M., Levin, E. J. T., Carrico, C. M., Kreidenweis, S. M., Malm, W. C., Laskin, A., and Desyaterik, Y., *Measured and modeled humidification factors of fresh smoke particles from biomass burning: role of inorganic constituents.* Atmos. Chem. Phys., 2010. 10: p. 6179-6194.
135. Guyon, P., Boucher, O., Graham, B., Beck, J., Mayol-Bracero, O. L., Roberts, G. C., Maenhaut, W., Artaxo, P., and Andreae, M. O., *Refractive index of aerosol particles over the Amazon tropical forest during LBA-EUSTACH 1999.* J. Aerosol. Sci., 2003. 34: p. 883-907.
136. Haywood, J.M., Osborne, S. R., Francis, P. N., Keil, A., Formenti, P., Andreae, M. O., and Kaye, P. H., *The mean physical and optical properties of regional haze dominated by biomass burning aerosol measured from the C-130 aircraft during SAFARI 2000.* J. Geophys. Res.- Atmos., 2003. 108.
137. Abel, S.J., Haywood, J. M., Highwood, E. J., Li, J., and Buseck, P. R., *Evolution of biomass burning aerosol properties from an agricultural fire in Southern Africa.* Geophys. Res. Lett., 2003. 30: p. 1783.
138. Johnson, B.T., Osborne, S. R., Haywood, J. M., and Harrison, M. A. J., *Aircraft measurements of biomass burning aerosol over West Africa during DABEX.* J. Geophys. Res.-Atmos., 2008. 113.
139. Wild, M., *Solar radiation budgets in atmospheric model intercomparisons from a surface perspective.* Geophys. Res. Lett., 2005. 32(7): p. L07704.
140. Garland, R.M., A. R. Ravishankara, E. R. Lovejoy, M. A. Tolbert, and T. Baynard, *Parameterization for the relative humidity dependence of light extinction: Organic-ammonium sulfate aerosol.* J. Geophys. Res., 2007. 112(D19303).
141. Baynard, T., et al., *Key factors influencing the relative humidity dependence of aerosol light scattering.* Geophys. Res. Lett., 2006. 33(6): p. L06813.
142. Hasenkopf, C.A., et al., *Potential Climatic Impact of Organic Haze on Early Earth.* Astrobiology, 2011. 11(2): p. 135-149.
143. Kanakidou, M., et al., *Organic aerosol and global climate modelling: a review.* Atmos. Chem. Phys., 2005. 5(4): p. 1053-1123.
144. Yu, H., et al., *A review of measurement-based assessments of the aerosol direct radiative effect and forcing.* Atmospheric Chemistry and Physics, 2006. 6: p. 613-666.
145. Jacobson, M.Z., *Effects of Externally-Through-Internally-Mixed Soot Inclusions within Clouds and Precipitation on Global Climateâ€* The Journal of Physical Chemistry A, 2006. 110(21): p. 6860-6873.

146. Haywood, J.M., et al., *General Circulation Model Calculations of the Direct Radiative Forcing by Anthropogenic Sulfate and Fossil-Fuel Soot Aerosol.* Journal of Climate, 1997. 10(7): p. 1562-1577.
147. Liu, X., et al., *Uncertainties in global aerosol simulations: Assessment using three meteorological data sets.* J. Geophys. Res., 2007. 112(D11): p. D11212.
148. Sjogren, S., et al., *Hygroscopic growth and water uptake kinetics of two-phase aerosol particles consisting of ammonium sulfate, adipic and humic acid mixtures.* Journal of Aerosol Science, 2007. 38(2): p. 157-171.
149. Stokes, R.H., Robinson, R. A. , *Interactions in aqueous nonelectrolyte solutions. I. Solute-solvent equilibria.* Journal of Physical Chemistry, 1966. 70: p. 2126-2130.
150. Hoppel, W., *Determination of the aerosol size distribution from the mobility distribution of the charged fraction of aerosols.* J. Aerosol Sci., 1978. 9: p. 41 - 54.
151. Dinar, E., I. Taraniuk, E. R. Graber, T. Anttila, T. F. Mentel, and Y. Rudich, *Hygroscopic growth of atmospheric and model humic-like substances.* Journal of Geophysical Research, 2007. 112(D05211).
152. Daimon, M. and A. Masumura, *Measurement of the refractive index of distilled water from the near-infrared region to the ultraviolet region.* Appl. Opt., 2007. 46(18): p. 3811-3820.
153. Arnott, W.P., et al., *Photoacoustic and filter-based ambient aerosol light absorption measurements: Instrument comparisons and the role of relative humidity.* J. Geophys. Res., 2003. 108(D1): p. 4034.
154. Beaver, M.R., et al., *A laboratory investigation of the relative humidity dependence of light extinction by organic compounds from lignin combustion.* Environmental Research Letters, 2008. 3(4).
155. Gysel, M., Weingartner, E., Baltensperger, U., *Hygroscopicity of Aerosol Particles at Low Temperatures. 2. Theoretical and Experimental Hygroscopic Properties of Laboratory Generated Aerosols.* Environmental Science & Technology, 2002. 36(1): p. 63-68.
156. Brooks, S.D., P.J. DeMott, and S.M. Kreidenweis, *Water uptake by particles containing humic materials and mixtures of humic materials with ammonium sulfate.* Atmospheric Environment, 2004. 38(13): p. 1859-1868.
157. Bockhorn, H., *Soot formation in combustion : mechanisms and models*. 1994, Berlin; New York: Springer-Verlag.
158. Medalia, A.I. and D. Rivin, *Particulate carbon and other components of soot and carbon black.* Carbon, 1982. 20(6): p. 481-492.
159. Wentzel, M., et al., *Transmission electron microscopical and aerosol dynamical characterization of soot aerosols.* Journal of Aerosol Science, 2003. 34(10): p. 1347-1370.
160. Rodhe, H., C. Persson, and O. Åkesson, *An investigation into regional transport of soot and sulfate aerosols.* Atmospheric Environment (1967), 1972. 6(9): p. 675-693.
161. Jacobson, M.Z., *A physically-based treatment of elemental carbon optics: Implications for global direct forcing of aerosols.* Geophysical Research Letters, 2000. 27(2): p. 217-220.
162. Sato, M., et al., *Global atmospheric black carbon inferred from AERONET.* Proceedings of the National Academy of Sciences of the United States of America, 2003. 100(11): p. 6319-6324.
163. Ramanathan, V., et al., *Indian Ocean Experiment: An integrated analysis of the climate forcing and effects of the great Indo-Asian haze.* J. Geophys. Res., 2001. 106(D22): p. 28371-28398.

164. Ramanathan, V. and G. Carmichael, *Global and regional climate changes due to black carbon.* Nature Geosci, 2008. 1(4): p. 221-227.
165. Cess, R.D., *Arctic aerosols: Model estimates of interactive influences upon the surface-atmosphere clearsky radiation budget.* Atmospheric Environment (1967), 1983. 17(12): p. 2555-2564.
166. Clarke, A.D. and K.J. Noone, *Soot in the Arctic snowpack: a cause for perturbations in radiative transfer.* Atmospheric Environment (1967), 1985. 19(12): p. 2045-2053.
167. Mikhailov, E.F., et al., *Optical properties of soot-water drop agglomerates: An experimental study.* J. Geophys. Res., 2006. 111(D7): p. D07209.
168. Hasegawa, S. and S. Ohta, *Some measurements of the mixing state of soot-containing particles at urban and non-urban sites.* Atmospheric Environment, 2002. 36(24): p. 3899-3908.
169. Naoe, H. and K. Okada, *Mixing properties of submicrometer aerosol particles in the urban atmosphere--with regard to soot particles.* Atmospheric Environment, 2001. 35(33): p. 5765-5772.
170. Pósfai, M., et al., *Soot and sulfate aerosol particles in the remote marine troposphere.* J. Geophys. Res., 1999. 104(D17): p. 21685-21693.
171. Fuller, K.A., W.C. Malm, and S.M. Kreidenweis, *Effects of mixing on extinction by carbonaceous particles.* J. Geophys. Res., 1999. 104(D13): p. 15941-15954.
172. Bond, T.C., G. Habib, and R.W. Bergstrom, *Limitations in the enhancement of visible light absorption due to mixing state.* J. Geophys. Res., 2006. 111(D20): p. D20211.
173. Lack, D.A., et al., *Absorption Enhancement of Coated Absorbing Aerosols: Validation of the Photo-Acoustic Technique for Measuring the Enhancement.* Aerosol Science and Technology, 2009. 43(10): p. 1006-1012.
174. Shiraiwa, M., et al., *Amplification of Light Absorption of Black Carbon by Organic Coating.* Aerosol Science and Technology, 2009. 44(1): p. 46-54.
175. Lack, D.A., et al., *Relative humidity dependence of light absorption by mineral dust after long-range atmospheric transport from the Sahara.* Geophys. Res. Lett., 2009. 36(24): p. L24805.
176. Zhang, R., et al., *Variability in morphology, hygroscopicity, and optical properties of soot aerosols during atmospheric processing.* Proceedings of the National Academy of Sciences, 2008. 105(30): p. 10291-10296.
177. Khalizov, A.F., et al., *Enhanced Light Absorption and Scattering by Carbon Soot Aerosol Internally Mixed with Sulfuric Acid.* Journal of Physical Chemistry A, 2009. 113(6): p. 1066-1074.
178. Naumann, K.-H., *COSIMA--a computer program simulating the dynamics of fractal aerosols.* Journal of Aerosol Science, 2003. 34(10): p. 1371-1397.
179. Moteki, N., Y. Kondo, and S. Nakamura, *Method to measure refractive indices of small nonspherical particles: Application to black carbon particles.* Journal of Aerosol Science. 41(5): p. 513-521.
180. Möhler, O., et al., *Experimental investigation of homogeneous freezing of sulphuric acid particles in the aerosol chamber AIDA.* Atmos. Chem. Phys., 2003. 3(1): p. 211-223.
181. Schnaiter, M., et al., *Strong spectral dependence of light absorption by organic carbon particles formed by propane combustion.* Atmos. Chem. Phys., 2006. 6(10): p. 2981-2990.
182. Saathoff, H., et al., *Coating of soot and (NH4)2SO4 particles by ozonolysis products of [alpha]-pinene.* Journal of Aerosol Science, 2003. 34(10): p. 1297-1321.
183. Schnaiter, M., et al., *UV-VIS-NIR spectral optical properties of soot and soot-containing aerosols.* Journal of Aerosol Science, 2003. 34(10): p. 1421-1444.

184. Wex, H., et al., *Towards closing the gap between hygroscopic growth and activation for secondary organic aerosol: Part 1 â€“ Evidence from measurements.* Atmos. Chem. Phys., 2009. 9(12): p. 3987-3997.
185. Nakayama, T., et al., *Laboratory studies on optical properties of secondary organic aerosols generated during the photooxidation of toluene and the ozonolysis of alpha-pinene.* Journal of Geophysical Research-Atmospheres, 2010. 115: p. 11.
186. Kim, H., B. Barkey, and S.E. Paulson, *Real refractive indices of alpha- and beta-pinene and toluene secondary organic aerosols generated from ozonolysis and photo-oxidation.* Journal of Geophysical Research-Atmospheres, 2010. 115: p. 10.
187. Barkey, B., S.E. Paulson, and A. Chung, *Genetic Algorithm Inversion of Dual Polarization Polar Nephelometer Data to Determine Aerosol Refractive Index.* Aerosol Science and Technology, 2007. 41(8): p. 751-760.
188. Yu, Y., et al., *Photooxidation of [alpha]-pinene at high relative humidity in the presence of increasing concentrations of NOx.* Atmospheric Environment, 2008. 42(20): p. 5044-5060.
189. Thomson, S.W., *On the equilibrium of vapour at a curved surface of liquid. Philosophical Magazine*, 1871. 4: p. 448-452.
190. Kohler, H., *The nucleus in and the growth of hygroscopic droplets.* Transactions of the Faraday Society, 1936. 32: p. 1152-1161.
191. Wright, H.L., *The size of atmospheric nuclei: Some deductions from measurements of the number of charged and uncharged nuclei at kew observatory.* Proceedings of the Physical Society, 1936. 48(5): p. 675.
192. Lewis, E.R., *The effect of surface tension (Kelvin effect) on the equilibrium radius of a hygroscopic aqueous aerosol particle.* Journal of Aerosol Science, 2006. 37(11): p. 1605-1617.
193. Gao, Y., S.B. Chen, and L.E. Yu, *Efflorescence relative humidity of airborne sodium chloride particles: A theoretical investigation.* Atmospheric Environment, 2007. 41(9): p. 2019-2023.